UNIVERSITY OF CALGARY

Comparison of the Effects of a Conductive Host on Moving- and Fixed-Source Frequency Domain Electromagnetic Devices

by

Tricia Dianne Nichols

A THESIS

SUBMITTED TO THE FACULTY OF GRADUATE STUDIES

IN PARTIAL FULFILLMENT OF THE REQUIREMENTS FOR THE

DEGREE OF MASTER OF SCIENCE

DEPARTMENT OF GEOLOGY AND GEOPHYSICS

CALGARY, ALBERTA

JUNE, 1999

Abstract

A physical scale model of a vertical tabular conductor (6.3E4 S/m) placed in a conductive (9.93 S/m) and resistive (air) host was surveyed by a moving-source (1.5-cm diameter transmitter), and a fixed-source (1-m square transmitter) device. Nine transmitter frequencies and five target depths were used for both devices. Argand diagrams of conductive host data showed unexpected second dispersions for both devices. These dispersions began at 40 and 4 kHz for the moving- and fixed-source devices respectively. The ratio of the target's conductive host response to its free-space response was as great as 6.0 for the fixed-source, and 1.3 for the moving-source system. Contrary to published results, these ratios decreased with depth for the fixed-source transmitter. Differences in transmitter size and geometry and the conductivity contrast between the host and target are thought to be the cause of the unexpected and unpredicted behavior.

Acknowledgements

The author wishes to express her appreciation to the following people for the contribution of their time, energy, and resources: Dr. Ken Duckworth and Dr. Edward S. Krebes for their moral and financial support, Eric Gallant and John Juigalli for their technical expertise, and Malcolm Bertram, Lynne Maillet-Frotten and Henry Bland for their assistance with computer-related problems.

I would also like to thank Dr. Viola Birss for the loan of a conductivity cell, Dr. Melvin Best for providing us with a copy of his modeling program and documentation, and Dr. Ron Johnston for allowing me access to a trial of some electromagnetic modeling software.

Finally, I would like to thank the friends and family who cheered me on from the sidelines. I couldn't have done it without you!

To my parents,

Robert and Judith Nichols

Table of Contents

List of Tables

Table of Figures

Chapter 1

1 Introduction

Electromagnetic prospecting devices are classified by the type of source or by the type of data they record. Sources can be either moving or fixed, and the data can be collected in either the time- or frequency-domain. Comparison of surveys performed over the same target using different electromagnetic prospecting methods shows that geological interpretations and calculations of electromagnetic properties often depend on the device used (Macnae and Walker, 1981; Pitcher, 1985; Duckworth and O'Neill, 1992). Why different devices should result in different interpretations of the same target is a question that has received very little attention in the literature. To understand this apparent inconsistency, the responses of two commonly used frequency-domain devices to the same target were compared using physical scale modeling. The horizontal coplanar moving-source system and a Turam-type fixed-source device were compared. The rest of this discussion will be limited to frequency-domain systems.

Physical scale modeling provides a means of simulating large-scale electromagnetic systems exactly in a laboratory setting. The act of scaling the linear dimensions of a system requires that the frequencies and electromagnetic parameters be scaled as well. Sinclair (1948) and Spies (1976) have derived the relationships between model and full-scale electromagnetic parameters. The condition for equivalence in the present study, was that the dimensionless product of conductivity, σ, magnetic permeability, μ, angular frequency of the transmitter, ω, and a squared dimension of length, L^2 be the same for both systems. Algebraically, the equivalence condition for two systems (denoted by the subscripts 1 and 2) is expressed as

$$\sigma_1\mu_1\omega_1 L_1^2 = \sigma_2\mu_2\omega_2 L_2^2. \qquad \textit{Equation 1-1}$$

In this study, the moving-source system was the horizontal coplanar coil system where one coil was a source, the other a receiver. The fixed-source system was a large, square, horizontal loop that was coplanar with a small horizontal coil receiver. The target was a vertical tabular conductor immersed in either a free-space or conductive host. The conductive host was modeled by a brine solution that was several orders of magnitude less conductive than the target. The transmitter and receiver coils were placed in air at a height t above the surface of the host. The air layer between the coils and the host represents a resistive overburden. By varying the depth, D, of the target and the frequency of the source field, different full-scale conditions were modeled according to Equation 1-1. A diagram of the target system is shown in Figure 1-1.

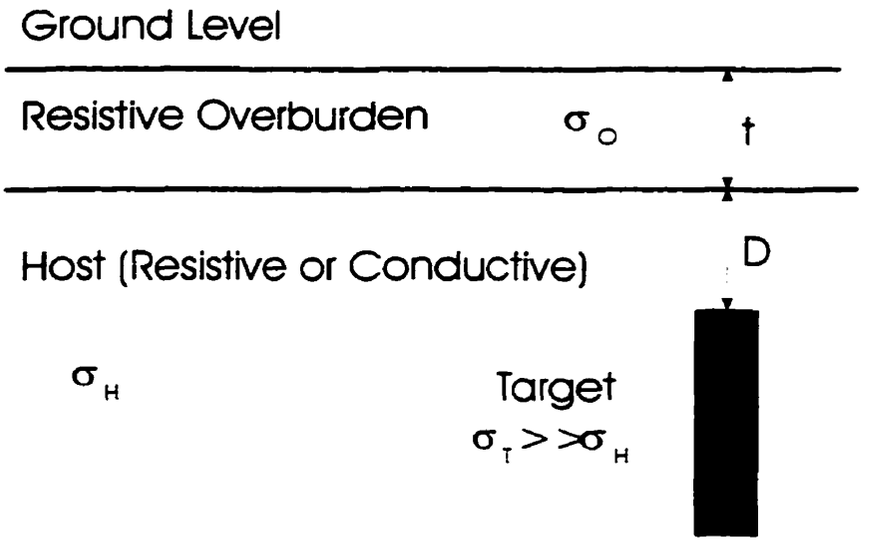

Figure 1-1: The host was either resistive or conductive with a resistive overburden of thickness t. The target was tabular buried to a depth D under the surface of the host. The conductivity of the target was several orders of magnitude larger than that of the conductive host.

Interpretations made from data from early inductive devices assumed that the effects due to a resistive host could be ignored. In reality, there are significant changes in the target's response when the effects of even slightly conductive hosts and overburdens are present. To improve the understanding of these situations, Lowrie and West (1965) used physical scale model studies to determine the effects of a conductive overburden on the response of a horizontal coplanar loop device. Their results showed that when the free-space assumption was used, targets beneath (but not in contact with) a conductive overburden appeared to be deeper, and better conductors than they really were.

Physical scale modeling of the effects of a conducting host on moving-source systems was also performed by Guptasarma and Maru (1971), Gaur et al. (1972), and Verma and Gaur, (1975). These authors demonstrated that a target in a conductive host responded more strongly, and possibly with a differently shaped profile, than the same target in free-space. It was found that the conductive host also caused a change in the phase of the anomaly. Attenuations due to the electromagnetic fields passing through the host were observed, but the effect was usually small relative to the anomaly enhancements. The anomaly enhancements were attributed to induced currents in the host taking the path of least resistance through the more conductive target. This tendency for host currents to 'channel' through the target was termed 'current gathering'.

Hanneson and West (1984) used numerical models of moving-source systems in conductive host environments to investigate the effect of increasing host conductivity. They found that both current gathering and attenuation effects were always present, but that the current gathering effects dominated over attenuation when the host conductivity was low. The initial result of an increase in host conductivity was a slight counter clockwise phase rotation of the anomaly accompanied by a slight enhancement of the anomaly amplitude. Further increases resulted in clockwise phase rotations and larger amplitude enhancements. Amplitude attenuation was noted at the highest conductivities considered, while the phase rotations continued in the clockwise direction.

Lajoie and West (1976) studied fixed-source devices in conductive host environments using numerical models. They predicted phase rotation and attenuation due to the host overlying the target, as well as current gathering related anomaly enhancements due to the conductive host surrounding the target. Physical scale modeling results indicate that the enhancement due to current gathering might be larger than predicted by the numerical models (Duckworth and O'Neill, 1989). However, the theoretical model assumed a thin conductor ('thin' means that only the *product* of conductivity and thickness is necessary to classify the conductor), and the targets used in the physical scale model study did not necessarily behave as thin conductors.

Each of the studies mentioned above has been dedicated to a single type of device. Lowrie and West (1965), Guptasarma and Maru (1971), and Hanneson and West (1984) focused on the horizontal coplanar moving-source device. Gaur et al. (1972), and Verma and Gaur (1975) compared different coil configurations of moving-source devices. Lajoie and West (1976), and Duckworth and O'Neill (1989) focused on the fixed-source device, and Duckworth and O'Neill (1992) compared two methods of operation for a fixed-source device. Very few direct comparisons of moving-source and fixed-source devices have been published. This purpose of this study was to investigate the relative effects that a conductive host environment has on the results of moving-source and fixed-source frequency-domain electromagnetic prospecting devices.

Chapter 7 was included to document an unsuccessful attempt to reproduce published results for a conductive sphere in free-space when surveyed by a vertical coaxial moving-source system.

Chapter 2

2 Relevant Electromagnetic Theory

In this section, the theory related to electromagnetic physical scale modeling is presented. The equivalence condition for electromagnetic physical scale modeling is derived from Maxwell's equations, the theoretical definition of 'skin depth' is provided, and brief discussion of electromagnetic induction as it applies to geophysical systems is also included.

2.1 Scaling Theory

There are two types of physical scale modeling, geometrical, and absolute. Geometric models simulate the spatial manifestations, but not the power levels, of the electromagnetic fields and may be used when the properties to be studied can be expressed in a dimensionless form. The amplitudes of the electric and magnetic fields do not need to be scaled for geometric models. Absolute models are used when the quantities to be measured are not dimensionless, so the amplitudes of the fields must be scaled as well as the dimensions, time, and electromagnetic properties of the model materials. The theory of absolute and geometric physical scale modeling was presented by Sinclair (1948), who derived the theory and discussed the limitations imposed on physical scale modeling due to the finite selection of modeling materials. Ward (1967), and Frischknecht (1988), generalized this theory for systems where displacement currents may be neglected, and showed that in such cases the condition for geometric modeling was satisfied if a quantity called the induction number was invariant with a change of scale between two systems. Ward and Frischknecht defined the induction number as the dimensionless product of $\sigma\mu\omega L^2$, where σ, μ, and L are the conductivity, magnetic permeability, and a significant, though arbitrary, linear dimension of the system under consideration, and ω is the angular frequency of the primary field. The theory of

electromagnetic physical scale modeling which follows is based on the work of Sinclair, Ward, and Frischknecht.

If System 1 is a full-scale system consisting of materials that are linear (i.e. constant in time) in conductivity, magnetic permeability, and electric permittivity, then Maxwell's equations (Equations 2-1 to 2-4) describe the behavior of the electromagnetic fields within the system. It is assumed that there are no isolated charges within the system.

Maxwell's Equations for System 1:

$$\nabla_1 \times \mathbf{E}_1 = -\mu_1 \frac{\partial \mathbf{H}_1}{\partial t_1} \qquad \textit{Equation 2-1}$$

$$\nabla_1 \times \mathbf{H}_1 = \sigma_1 E_1 + \varepsilon_1 \frac{\partial \mathbf{E}_1}{\partial t_1} \qquad \textit{Equation 2-2}$$

$$\nabla_1 \cdot \mathbf{H}_1 = 0 \qquad \textit{Equation 2-3}$$

$$\nabla_1 \cdot \mathbf{E}_1 = 0 \qquad \textit{Equation 2-4}$$

In the above equations, $\mathbf{E}_1$ and $\mathbf{H}_1$ are the electric and magnetic field vectors, and σ_1, μ_1, and ε_1 are the conductivity, magnetic permeability, and electric permittivity of a given material, and ∇_1 is the gradient operator in terms of the Cartesian coordinates of System 1. The aim of physical scale modeling is to model the full-scale system (System 1) with a smaller version (System 2) in such a way that the two systems are electromagnetically identical. If the linear dimensions, times, and electromagnetic vectors of Systems 1 and 2 are scaled by way of the following equations, then it is possible to calculate scaling factors, p, q, a, and b for System 2 that will make the two systems electromagnetically identical (Sinclair, 1948).

$$x_1 = px_2 \qquad \textit{Equation 2-5}$$

$$y_1 = py_2 \qquad \textit{Equation 2-6}$$

$$z_1 = pz_2 \qquad \textit{Equation 2-7}$$

$$t_1 = qt_2 \qquad \textit{Equation 2-8}$$

$$\mathrm{E}_1 = a\mathbf{E}_2 \qquad \textit{Equation 2-9}$$

$$\mathbf{H}_1 = b\mathbf{H}_2 \qquad \textit{Equation 2-10}$$

To determine the relationships between the electromagnetic parameters and frequencies of Systems 1 and 2, Equations 2-11 and 2-12 (Maxwell's equations for System 2) must be written in terms of $\mathbf{E}_1$, $\mathbf{H}_1$, t_1, and the Cartesian coordinates of System 1.

Maxwell's Equations for System 2:

$$\nabla_2 \times \mathbf{E}_2 = -\mu_2 \frac{\partial \mathbf{H}_2}{\partial t_2} \qquad \textit{Equation 2-11}$$

$$\nabla_2 \times \mathbf{H}_2 = \sigma_2 \mathbf{E}_2 + \varepsilon_2 \frac{\partial \mathbf{E}_2}{\partial t_2} \qquad \textit{Equation 2-12}$$

$$\nabla_2 \cdot \mathbf{H}_2 = 0 \qquad \textit{Equation 2-13}$$

$$\nabla_2 \cdot \mathbf{E}_2 = 0 \qquad \textit{Equation 2-14}$$

It is shown in Appendix A that $\nabla_2 \times \mathbf{V} = p\nabla_1 \times \mathbf{V}$, and that $\partial \mathbf{V}/\partial t_2 = q\,\partial \mathbf{V}/\partial t_1$, so that substitution of Equations 2-5 to 2-10 into Equations 2-11 and 2-12 will produce the following equations for System 2 in terms of $\mathbf{E}_1$ and $\mathbf{H}_1$:

$$\frac{p}{a}\nabla_1 \times \mathbf{E}_1 = -\mu_2 \frac{q}{b}\frac{\partial \mathbf{H}_1}{\partial t_1} \qquad \textit{Equation 2-15}$$

$$\frac{p}{b}\nabla_1 \times \mathbf{H}_1 = \sigma_2 \frac{1}{a}\mathbf{E}_1 + \varepsilon_2 \frac{q}{a}\frac{\partial \mathbf{E}_1}{\partial t_1} \qquad \textit{Equation 2-16}$$

Comparison of Equations 2-15 and 2-16 with Equations 2-1 and 2-2, provides the constraints that must be placed on the conductivity, magnetic permeability, and electric permittivity for electromagnetic equivalence of the two systems as follows:

$$\sigma_2 = \frac{ap}{b}\sigma_1 \qquad \textit{Equation 2-17}$$

$$\mu_2 = \frac{bp}{aq}\mu_1 \qquad \textit{Equation 2-18}$$

$$\varepsilon_2 = \frac{ap}{bq}\varepsilon_1 \qquad \textit{Equation 2-19}$$

It is important to note that Equations 2-17, 2-18, and 2-19 must hold for all materials in the system. Sinclair (1948) notes that air in the full-scale system, is most effectively modeled by air in the model, so that for these regions, $\mu_1=\mu_2$, and $\varepsilon_1=\varepsilon_2$. Since Equations 2-18 and 2-19 must hold for all regions in the model, the constants of proportionality which relate the full-scale and model magnetic permeabilities and electric permittivities to one another must be unity. These conditions are expressed in Equations 2-20 and 2-21.

$$\frac{bp}{aq} = 1 \qquad \textit{Equation 2-20}$$

$$\frac{ap}{bq} = 1 \qquad \textit{Equation 2-21}$$

Equations 2-20 and 2-21 require that

$$\frac{a}{b} = 1 \qquad \textit{Equation 2-22}$$

and

$$\frac{p}{q} = 1 \qquad \textit{Equation 2-23}$$

so that the conditions for electromagnetic equivalence become:

$$\sigma_2 = p\sigma_1 \qquad \textit{Equation 2-24}$$

$$\mu_2 = \mu_1 \qquad \textit{Equation 2-25}$$

$$\varepsilon_2 = \varepsilon_1 \qquad \textit{Equation 2-26}$$

The electrical parameters of the model materials are related to the full-scale parameters by Equations 2-17 through 2-19 for a general system, or Equations 2-24 through 2-26 for a system where air is modeled by air. For a geometric model, the amplitudes of the electric and magnetic fields do not need to be scaled, so a specific value for a does not need to be used, provided Equation 2-22 is satisfied. In this study, all the data are in the form of percentages, so a geometric model is sufficient.

Frischknecht (1988) further simplified these conditions by neglecting displacement currents, and therefore any conditions relating to electric permittivity. Under these conditions, the relationship between model and full-scale conductivity is given by

$$\sigma_2 = \frac{p^2}{q}\sigma_1 \qquad \textit{Equation 2-27}$$

By substituting relationships from Equations 2-5 to 2-10 in to Equation 2-27, and letting L_n represent a dimension of length in System n, Equation 2-27 may be written in induction number form as

$$\sigma_2 = \frac{(L_1/L_2)^2}{(t_1/t_2)}\sigma_1$$

$$\sigma_2 \frac{L_2^2}{t_2} = \sigma_1 \frac{L_1^2}{t_1} \qquad \textit{Equation 2-28}$$

$$(\mu_2)\sigma_2\omega_2 L_2^2 = (\mu_1)\sigma_1\omega_1 L_1^2$$

Where the magnetic permeability has been re-introduced as a formality, though for most modeling materials that are suitable for physical scale modeling, $\mu_1 \cong \mu_2 \cong \mu_o$, and the magnetic permeabilities will cancel.

The condition given by Equation 2-28 is all that is required for equivalence using geometric modeling provided that everywhere $\mu=\mu_o$, and ω_n is low enough that displacement currents may be neglected. If quantities that are not dimensionless (e.g. impedance) are to be studied, scaling relationships for voltages, currents, and current densities must also be considered (Frischknecht, 1988; Spies, 1976).

It is noteworthy that Equation 2-28 may also be derived by scaling the skin depths[1] of the materials in the same way that other model lengths are scaled (see Appendix B).

---

[1] The skin depth of a material is calculated from the following formula and has dimensions of length: $\delta = \sqrt{2/\sigma\mu\omega}$, where σ is conductivity, μ is magnetic permeability, and ω is the angular frequency of the impinging field. A derivation and discussion of the physical significance of the skin depth will be presented in Section 2.2.

Bosschart (1964) defined a thin conductor as one for which the conductance (conductivity-thickness product) was all that needed to be scaled for electromagnetic equivalence. Therefore, for thin conductors, the equivalence condition for geometric modeling becomes

$$(\sigma_2 T_2)\omega_2 L_2 = (\sigma_1 T_1)\omega_1 L_1 . \qquad \textit{Equation 2-29}$$

where T_1 and T_2 are the thicknesses of the conductors. This implies that only the product of conductivity and thickness can be determined from the response of a thin conductor. There are limits beyond which targets with identical conductances will not produce identical responses, and in these cases it may be possible to determine the conductivity and thickness independently (Hedström and Parasnis, 1958). In practice, Bosschart's thin conductor definition will be met if there is a linear variation of the in-phase to quadrature ratio with response parameter (see Section 2.3).

At the frequencies that were used in this study, the target could not always be considered 'thin', but the deviation from the thin conductor approximation does not affect the results since the purpose was to compare the responses of moving-source systems to fixed-source systems over the same target. The target may stop responding as a thin conductor at different frequencies for each device because the geometry of the transmitted fields is different. Deviations from a 'thin' target have to be considered if the final anomaly index diagrams (Figures 5-2, 5-4, 5-7 and 5-8) are to be used for interpreting field data. Tables 2-1 and 2-2 give the skin depths for the modeling materials, graphite and brine, used to simulate the target and host respectively. The frequencies shown are those used in the physical model studies. In general, the shorter the skin depth with respect to the dimensions of the body, the more effect an electromagnetic field will have on that body. The theoretical derivation of the skin depth is given in the next section.

Table 2-1: Skin depths for graphite at model frequencies (conductivity of the graphite: 6.3E+04 S/m, thickness of the target: 1.45 cm)

Frequency (kHz)	Skin Depth (m)
1	6.34E-02
2	4.48E-02
4	3.17E-02
10	2.01E-02
20	1.42E-02
40	1.00E-02
100	6.34E-03
200	4.48E-03
400	3.17E-03

Table 2-2: Skin Depths for brine at model frequencies (conductivity of the brine: 9.93 S/m)

Frequency (kHz)	Skin Depth (m)
1	5.05
2	3.57
4	2.53
10	1.60
20	1.13
40	0.80
100	0.51
200	0.36
400	0.25

2.2 Skin Depth

The skin depth of a material is defined as the depth at which the amplitude of a plane electromagnetic wave incident upon the planar surface of a conductive medium is attenuated by a factor of $1/e$. The following discussion of skin depth is based on the presentations by Lorrain, Corson, and Lorrain (1988), Grant and West (1965), and Keller (1988).

The amplitude of a harmonically oscillating plane wave is described in phasor notation by

$$F = F_{max} e^{i(\omega t - kz)} \qquad \textit{Equation 2-30}$$

where F_{max} is the maximum amplitude of the wave, ω is the angular frequency of the wave, t is time, k is the wave number, and z is the axis of propagation. The wave number is defined as $2\pi/\lambda$ where λ is the wavelength of the wave.

For a plane electromagnetic wave in a conducting medium, the wave number is complex

$$k = \beta - i\alpha \qquad \textit{Equation 2-31}$$

and Equation 2-30 becomes

$$\begin{aligned} F &= F_{max} e^{i(\omega t - (\beta - i\alpha)z)} \\ &= F_{max} e^{-\alpha z} e^{i(\omega t - \beta z)} \end{aligned} \qquad \textit{Equation 2-32}$$

The term $e^{-\alpha z}$ causes attenuation of the amplitude with distance z. By definition, the skin depth is the depth at which the amplitude has been attenuated by $1/e$, so $\delta = z$ when $\alpha z = 1$, or

$$\delta = 1/\alpha . \qquad \textit{Equation 2-33}$$

To represent α in terms of frequency, conductivity, magnetic permeability, and electric permittivity, it is necessary to derive the electromagnetic wave equation from Maxwell's equations.

Equation 2-1 relates the curl of the **E** vector to the time derivative of the **H** vector, and Equation 2-2 relates the curl of the **H** vector to the **E** vector and its time derivative. Using the vector relationship

$$\nabla\times(\nabla\times\mathbf{A})=\nabla(\nabla\cdot\mathbf{A})-\nabla\cdot\nabla\mathbf{A}$$
$$=\nabla(\nabla\cdot\mathbf{A})-\nabla^2\mathbf{A} \qquad \textit{Equation 2-34}$$

(for rectangular coordinates), where

$$\nabla^2\mathbf{A}=\bar{i}_x\nabla^2A_x+\bar{i}_y\nabla^2A_y+\bar{i}_z\nabla^2A_z \qquad \textit{Equation 2-35}$$

and $\bar{i}_n$ is the unit vector in the *n*th direction. Equations 2-1 to 2-4 yield the following equations:

$$\nabla\times(\nabla\times\mathbf{E})=\nabla(\nabla\cdot\mathbf{E})-\nabla^2\mathbf{E}=\nabla\times\left(-\mu\frac{\partial\mathbf{H}}{\partial t}\right)$$
$$\nabla(0)-\nabla^2\mathbf{E}=-\mu\frac{\partial}{\partial t}(\nabla\times\mathbf{H})=-\mu\frac{\partial}{\partial t}\left(\sigma\mathbf{E}+\varepsilon\frac{\partial\mathbf{E}}{\partial t}\right)$$
$$\nabla^2\mathbf{E}-\sigma\mu\frac{\partial\mathbf{E}}{\partial t}-\varepsilon\mu\frac{\partial^2\mathbf{E}}{\partial t^2}=0$$

and *Equation 2-36*

$$\nabla(\nabla\times\mathbf{H})=\nabla(\nabla\cdot\mathbf{H})-\nabla^2\mathbf{H}=\nabla\times\left(\sigma\mathbf{E}+\varepsilon\frac{\partial\mathbf{E}}{\partial t}\right)$$
$$\nabla(0)-\nabla^2\mathbf{H}=\sigma\nabla\times\mathbf{E}+\varepsilon\frac{\partial}{\partial t}(\nabla\times\mathbf{E})$$
$$-\nabla^2\mathbf{H}=\sigma\left(-\mu\frac{\partial\mathbf{H}}{\partial t}\right)+\varepsilon\left(\frac{\partial^2\mathbf{H}}{\partial t^2}\right)$$
$$\nabla^2\mathbf{H}-\sigma\mu\frac{\partial\mathbf{H}}{\partial t}-\varepsilon\mu\frac{\partial^2\mathbf{H}}{\partial t^2}=0 \qquad \textit{Equation 2-37}$$

If we consider only sinusoidally varying fields of the form

$$(\mathbf{E}\ or\ \mathbf{H})=(\mathbf{E}_o\ or\ \mathbf{H}_o)e^{i(\omega t-kz)} \qquad \textit{Equation 2-38}$$

where $\mathbf{E}_o$ and $\mathbf{H}_o$ are amplitudes of the fields at $t = 0$, then the time derivative becomes

$$\frac{\partial}{\partial t}(\mathbf{E} \text{ or } \mathbf{H}) = -i\omega(\mathbf{E} \text{ or } \mathbf{H}) \qquad \textit{Equation 2-39}$$

and Equations 2-36 and 2-37 may be written as

$$\nabla^2\mathbf{E} = (i\sigma\mu\omega - \varepsilon\mu\omega^2)\mathbf{E} \qquad \textit{Equation 2-40}$$

and

$$\nabla^2\mathbf{H} = (i\sigma\mu\omega - \varepsilon\mu\omega^2)\mathbf{H} \qquad \textit{Equation 2-41}$$

For Equation 2-30 to be a solution for **E** or **H** above, then the wave number k, is determined by calculating $\nabla^2\mathbf{F}$ and comparing the result to Equation 2-40 or 2-41. The Cartesian components of $\nabla^2\mathbf{F}$ are

$$(\nabla^2\mathbf{F})_x = \frac{\partial^2}{\partial x^2} F_{\max} e^{i(\omega t - kz)} = 0 \qquad \textit{Equation 2-42 a)}$$

$$(\nabla^2\mathbf{F})_y = \frac{\partial^2}{\partial y^2} F_{\max} e^{i(\omega t - kz)} = 0 \qquad \textit{b)}$$

and

$$(\nabla^2\mathbf{F})_z = \frac{\partial^2}{\partial z^2} F_{\max} e^{i(\omega t - kz)} = (-k^2)F \qquad \textit{c)}$$

where the x and y components become zero because the wave is traveling in the z direction only. By comparison, the square of the wave number is found to be

$$k^2 = \varepsilon\mu\omega^2 - i\sigma\mu\omega\,. \qquad \textit{Equation 2-43}$$

At this point it is convenient to make some assumptions about the relative magnitudes of the real and imaginary terms in Equation 2-43. In free-space, the conductivity is zero and the wave number is completely real ($\alpha = 0$) and given by

$$k = \sqrt{\varepsilon\mu\omega} \qquad \textit{Equation 2-44}$$

Substitution of a real wave number into Equation 2-32 eliminates the attenuation term, so electromagnetic waves traveling in free-space experience no attenuation. In a conductor at low frequencies (frequencies having periods much longer than the relaxation time (ε/σ) of the atoms) the imaginary term of Equation 2-43 dominates and the wave number is the complex function

$$k = \left(\frac{\sigma\mu\omega}{2}\right)^{1/2} - i\left(\frac{\sigma\mu\omega}{2}\right)^{1/2} \qquad \textit{Equation 2-45}$$
$$= \beta - i\alpha$$

In terms of the conductivity, magnetic permeability, and frequency, the skin depth (Equation 2-33) becomes

$$\delta = \frac{1}{\alpha} = \sqrt{\frac{2}{\sigma\mu\omega}}. \qquad \textit{Equation 2-46}$$

With attenuation comes phase rotation. Next it will be shown that the phase rotation at one skin depth is equal to ($1/2\pi$) radians.

The spatial wavelength of the uniform planar field is related to the β-term as follows:

Since $e^{i\theta}$ is a periodic function,

$$e^{-i\beta z_1} = e^{-i(\beta z_1 + 2\pi)} = e^{-i\beta z_2} \qquad \textit{Equation 2-47}$$

By definition, the wavelength, λ, equals the difference between z_2 and z_1, so

$$\beta z_1 + 2\pi = \beta z_2$$
$$\lambda = z_2 - z_1 = \frac{2\pi}{\beta} \qquad \textit{Equation 2-48}$$

Since λ is the distance over which the phase rotates by 2π, and, in this case, $\alpha = \beta$, then the phase rotation at one skin depth will be $\delta/\lambda = 1/(2\pi)$ radians.

2.3 A Simple Model of Electromagnetic Induction

A simple model that demonstrates the important characteristics of electromagnetic induction is shown in Figure 2-1. The model consists of two horizontal coplanar conductive loops that represent the transmitter and the receiver, and a third, vertical conducting loop that represents the target conductor. The following discussion is based on the presentation by Grant and West (1965). The transmitter, receiver, and target properties will be denoted by the subscripts *Tx*, *Rx*, and *Trg* respectively. The transmitter and target loops are closed circuits around which current can flow, and the receiver is an open circuit that does not permit current to flow. The transmitter generates a changing magnetic field (the primary field) that causes electric potentials (emfs) in the target and receiver circuits. The emf induced in the target causes current to flow in the target, which in turn generates a secondary magnetic field. The resultant emf due to the transmitter and the target is measured at the receiver circuit. *R* and *L* give the resistance and self-inductance of the target respectively. M_{ij} gives the mutual inductance between any two coils, where *i* and *j* are two of the three circuit labels. For any pair of circuits, M_{ij} is dependent only on the geometry of the two circuits, and $M_{ij} = M_{ji}$. In general, this is true for any pair of components of an inductively coupled system.

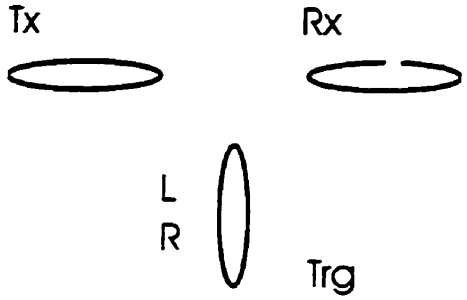

Figure 2-1: The three circuit model for electromagnetic induction. The transmitter, Tx, and target Trg, are closed single coils. The receiver, Rx, is an open single coil. The target has a self-inductance L, and a resistance R.

If the current in the transmitter is $I_{Tx}=I_{Txo}e^{i\omega t}$, then by Faraday's law, the emfs induced in the receiver and target circuits due to the current in the transmitter circuit are given by

$$\varepsilon_{Rx}^{(\text{Primary})} = -i\omega M_{\text{Tx Rx}} I_{\text{Tx o}} e^{i\omega t} \qquad \textit{Equation 2-49}$$

and

$$\varepsilon'_{Trg} = -i\omega M_{\text{Tx Trg}} I_{\text{Tx o}} e^{i\omega t} \qquad \textit{Equation 2-50}$$

The target circuit also experiences an emf due to its resistivity and self-inductance which is given by

$$\varepsilon''_{Trg} = -(R + i\omega L) I_{\text{Trg o}} e^{i\omega t}. \qquad \textit{Equation 2-51}$$

The total emf in the target circuit must be zero because it is a closed circuit, this gives Equation 2-52.

$$\begin{aligned} \varepsilon_{Trg} &= \varepsilon'_{Trg} + \varepsilon''_{Trg} \\ &= -i\omega M_{\text{Tx Trg}} I_{\text{Tx o}} e^{i\omega t} - (R + i\omega L) I_{\text{Trg o}} e^{i\omega t}. \\ &= 0 \end{aligned} \qquad \textit{Equation 2-52}$$

The above equation can be solved for the target current that is required in order to calculate the secondary fields at the receiver:

$$I_{\mathrm{Trg\,o}}e^{i\omega t} = -\frac{i\omega M_{\mathrm{Tx\,Trg}} I_{\mathrm{Tx\,o}} e^{i\omega t}}{(R+i\omega L)}\frac{(R-i\omega L)}{(R-i\omega L)} \qquad \textit{Equation 2-53}$$

$$= -\frac{M_{\mathrm{Tx\,Trg}}}{\mathbf{L}}\left[\frac{i\omega L(R-i\omega L)}{\left(R^2+\omega^2 L^2\right)}\right] I_{\mathrm{Tx\,o}} e^{i\omega t}$$

The secondary emf due to the target at the receiver is given by

$$\varepsilon_{Rx}^{(\mathrm{Secondary})} = -i\omega M_{\mathrm{Trg\,Rx}} I_{\mathrm{Trg\,o}} e^{i\omega t}. \qquad \textit{Equation 2-54}$$

Secondary fields are usually normalized to the primary field, so that the electromagnetic response has the form

$$\frac{\varepsilon_{Rx}^{(\mathrm{Secondary})}}{\varepsilon_{Rx}^{(\mathrm{Primary})}} = \frac{-i\omega M_{\mathrm{Trg\,Rx}} I_{\mathrm{Trg\,o}} e^{i\omega t}}{-i\omega M_{\mathrm{Tx\,Rx}} I_{\mathrm{Tx\,o}} e^{i\omega t}}. \qquad \textit{Equation 2-55}$$

Substitution of the expression for the target current (Equation 2-53) results in

$$\frac{\mathcal{E}_{Rx}^{(\text{Secondary})}}{\mathcal{E}_{Rx}^{(\text{Primary})}} = -\frac{M_{\text{Tx Trg}} M_{\text{Trg Rx}}}{M_{\text{Tx Rx}} L}\left[\frac{i\left(\omega L/R\right)\left(1 - i\left(\omega L/R\right)\right)}{1+\left(\omega L/R\right)^2}\right] \qquad \textit{Equation 2-56}$$

$$= -\frac{M_{\text{Tx Trg}} M_{\text{Trg Rx}}}{M_{\text{Tx Rx}} L}\left[\frac{\alpha^2 + i\alpha}{1+\alpha^2}\right]$$

where

$$\alpha = \omega L/R .$$

Equation 2-56 has two distinct parts, the first part, $\frac{M_{\text{Tx Trg}} M_{\text{Trg Rx}}}{M_{\text{Tx Rx}} L}$ is only dependent on the geometry and the size of the three loops (or components of an inductively coupled system). The second part, $\frac{\alpha^2 + i\alpha}{1+\alpha^2}$, is called the response function. The response function is dependent on the frequency of the transmitter and on the electromagnetic parameters of the target. The parameter α is called the response parameter. The behavior of the response function is of interest because it contains the information about the electromagnetic properties of the target. Figure 2-2 shows a plot of the response function. In the limit as α goes to zero (the resistive limit), the response function becomes $i\alpha$, so that $\frac{\mathcal{E}_{Rx}^{(\text{Secondary})}}{\mathcal{E}_{Rx}^{(\text{Primary})}}$ is completely imaginary. As α goes to infinity (the inductive limit), the response function asymptotes to 1, and $\frac{\mathcal{E}_{Rx}^{(\text{Secondary})}}{\mathcal{E}_{Rx}^{(\text{Primary})}}$ is purely real. The real to imaginary ratio for the three-circuit model is equal to α, which is a measure of the ratio of the self-inductance and resistance of the target. Because α is directly proportional to the frequency, there is a linear relationship between the real to imaginary ratio and frequency. Bosschart (1964) used this relationship as a practical definition of 'thin' conductor behavior.

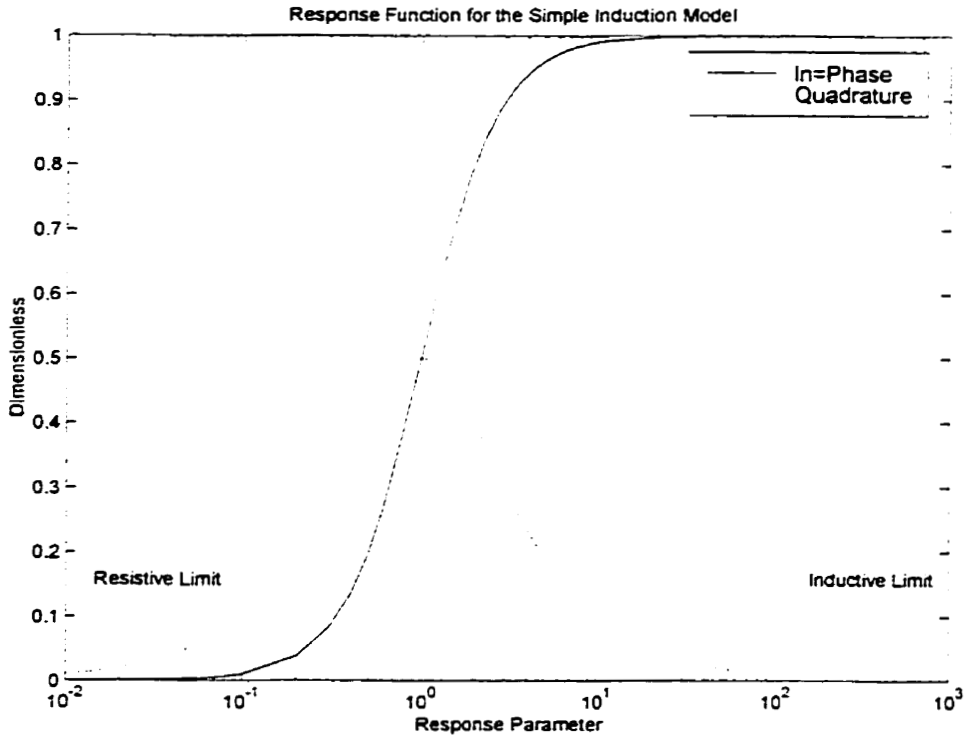

Figure 2-2: The in-phase and quadrature components of the response function of the simple induction model.

The real and imaginary components of a response are also referred to as the in-phase and quadrature components of the response. The latter terminology will be used throughout this thesis.

The phase of the target circuit's response is

$$\mathbf{phase} = \mathbf{arctan}\left(\frac{\mathbf{imaginary\ component}}{\mathbf{real\ component}}\right) = \mathbf{arctan}\left(\frac{1}{\alpha}\right) \qquad \textit{Equation 2-57}$$

As α goes to zero the phase goes to 90 degrees and as α goes to infinity, the phase goes to 180 degrees. It is important to note that the in-phase (real) and quadrature (imaginary)

currents in this example were confined to the same location in space since the target was modeled as a two dimensional loop. This is not necessarily true for three-dimensional conductors. There are two complications that arise from having in-phase and quadrature currents in different locations. The first is that for dipping targets, the in-phase and quadrature anomalies may be laterally displaced from one another so that the complex number that is assigned to such an anomaly may be due to an in-phase response at one location and a quadrature response at another location. The second complication is due to the different distances between the receiver and the source of the in-phase and quadrature currents. The fields from the nearer current will decay at a greater rate than those from the farther current so that only an apparent in-phase to quadrature ratio can be measured at the receiver. This also implies that measured phases are not the true phases of the target current. For this study, all amplitudes, phases, and complex components were derived using right-hand-triangle trigonometry as shown on Figure 2-3

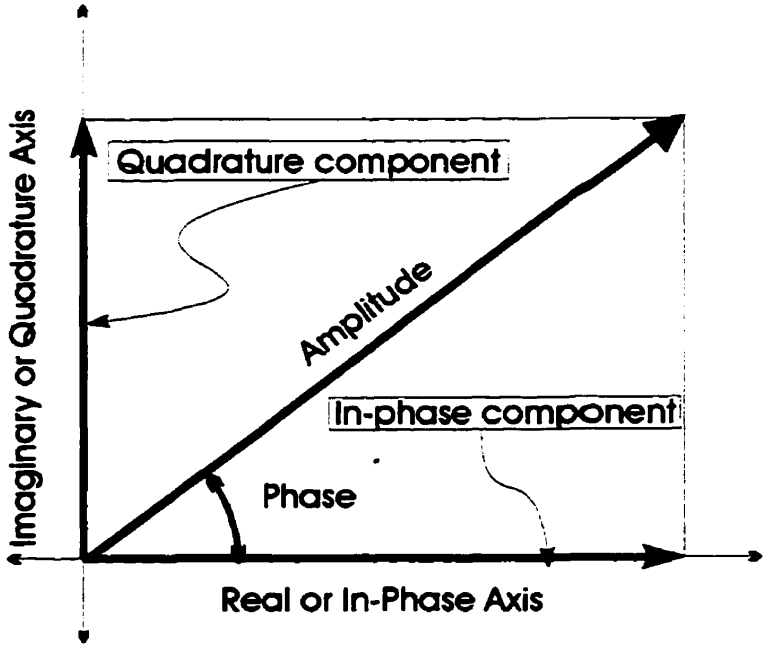

Figure 2-3: Definition of amplitude, phase, and complex components (in-phase and quadrature) as used in the present study.

Chapter 3

3 Physical Scale Modeling Facility and Procedures

The goal of this thesis was to compare the responses of the moving-source device to those of the fixed-source device over the same target. The target system consisted of a vertical tabular conductor (graphite, dimensions 1.5 × 20 × 98.5 cm, conductivity 6.3E10+4 S/m), in a host material. The host material was either free-space (air) or conductive (brine solution, dimensions 6 × 3 × 1.2 m, conductivity 9.93 S/m). For each system-host pair, sinusoidal signals of nine different frequencies (f = 1, 2, 4, 10, 20, 40, 100, 200, and 400 kHz), and five different target depths (D = 1, 2, 3, 4, and 5 cm) were used to obtain a suite of anomalies representing different electromagnetic systems.

3.1 Data Acquisition

A Hewlett Packard 3325A function generator controlled the transmitter signal and a 400 MHz Tektronix TDS 430A two channel digitizing oscilloscope was used to record the pre-amplified receiver signals. The horizontal and vertical location of the transmitter and receiver coils was controlled by a set of motorized beams and supports. A Quick BASIC program on a personal computer controlled the whole system. The program allowed the operator to select the survey type, operating frequency, and survey parameters. The program prompted the operator to select one of four survey types. For this study only two surveys were considered, a finite-separation moving-source system (the horizontal coplanar system), and the conventional fixed-source survey where the receiver traverse was perpendicular to the front edge of the transmitter. The other systems that could be modeled were a coincident coil moving-source device and a fixed-source device where the receiver traverse was parallel to the front edge of the transmitter. The operator controlled the transmitter frequency, the number of points for the oscilloscope to store (record length), and the number of readings for the oscilloscope to average together for

each stored point. The program provided a number of possible record lengths, and assigned (rather than calculated) a waveform sampling rate. The waveform-sampling rate was chosen so that there were an integral number of waveforms per record. After the data were transferred back to the computer, the oscilloscope record was broken into waveform-length sections that were summed together and divided by the number of waveforms in the sum. The result was one average waveform from which the in-phase and quadrature components of the anomaly could be obtained. For this study, nine frequencies in the range 1 kHz to 400 kHz were used and the sampling rates and number of waveforms per record are summarized in Table 3-1.

Table 3-1: Integral number of waveforms for a 15000-point oscilloscope record

Frequency (kHz)	Number of Points Per Waveform	Number of Waveforms Per Record
1	500	30
2	500	30
4	250	60
10	500	30
20	500	30
40	250	60
100	500	30
200	500	30
400	250	60

The resultant waveforms from the receiver that were acquired by the oscilloscope were transferred to the program where the in-phase and quadrature responses of the target-system were calculated by Fourier decomposition. This was accomplished by choosing a set of angles from 0° to 360° that were assigned to each point on the waveform. The in-phase component was then just the product of the cosine of the corresponding angle and the corresponding point on the waveform. The quadrature component was given by the product of the sine of the corresponding angle and corresponding point on the waveform.

This process separated the waveform into two components that were ninety degrees out of phase with one another, the in-phase and quadrature components.

For the moving-source system, the primary field is constant at the receiver because the transmitter-receiver separation was constant. This allowed for the primary field to be automatically subtracted from the measured resultant field leaving the secondary field. This was done after the data were collected, by subtracting the in-phase primary field reference signal from the resultant in-phase components. Moving-source data files included the in-phase and quadrature secondary field responses as well as the primary in-phase reference. The secondary field components were expressed as a percentage of the reference signal.

The fixed-source data files contained the raw amplitude and phase measurements of the resultant field. It was not possible to convert the fixed-source data from resultant to secondary fields as the survey progressed because, unlike the moving-source system, the primary field was not constant throughout the survey. For the fixed-source surveys, a reference signal was not required (instead a separate primary field file was recorded) and the amplitude and phase were calculated from the in-phase and quadrature values via

$$Amplitude = \sqrt{(In-Phase)^2 + (Quadrature)^2} \qquad \textit{Equation 3-1}$$

and

$$Phase = \mathbf{arctan}\left(\frac{Quadrature}{In-Phase}\right) \qquad \textit{Equation 3-2}$$

A description of the moving- and fixed-source data processing procedures can be found in Chapter 4.

More detailed information about this modeling facility may be found in the following Masters theses: Bays (1982), Cummins (1986), and O'Neill (1989).

3.2 System Stability Testing

To test the stability of the electronics system, the fixed-source system's receiver was set at 51.5 cm from the transmitter and five sets of 200 amplitude and phase reading were taken. Two sets of tests were performed, one at 400 kHz and one at 1 kHz. The time for 200 readings was about 20 minutes at 400 kHz, and about 30 minutes at 1 kHz. The 1 and 400 kHz tests were performed on different days, and were started as soon as possible after the system was turned on. The start and finish times of each 200-point data set were recorded to provide an estimate of the stabilization time required. The change in response with time was attributed to the warming up of the electronic equipment. Plots of the amplitude and phase as a function of time are provided in Figures 3-1 to 3-4 (note the different vertical scales). The system drift was defined as the difference between the first and last amplitude of a straight line fit through the 200-point data set, expressed as a percentage of the first amplitude on the line. Tables 3-2 to 3-5 summarize the results, but it is worth noting that even if no warm-up time was allowed, the system drift over the course of a 200 point survey could be confined to less than 2% of the recorded amplitude. Since all the data in this study were collected after the system had warmed-up for an hour, the effect of a system drift was less than 0.2% of the recorded amplitude. This error was further reduced because the anomaly occurred over approximately one third of the survey. Errors related to system drift were negligible when compared to the magnitudes of the anomalies for both moving- and fixed-source data sets.

The phase data for these tests is shown in Figures 3-2 and 3-4. The phase was observed to be sporadic for 400 kHz until 90 minutes after the system was turned on. At 1 kHz, the phase was more consistent with time. Neither frequency showed the theoretically expected zero-phase, though the phases for both frequencies were less than one degree. In a true free-space, all that the receiver should measure is the primary field and since the primary field is the phase reference, all measured phases should, theoretically, be zero.

These phases were measured in the lab rather than a true free-space, so non-zero phase readings may be due to materials in the floor, or other laboratory equipment.

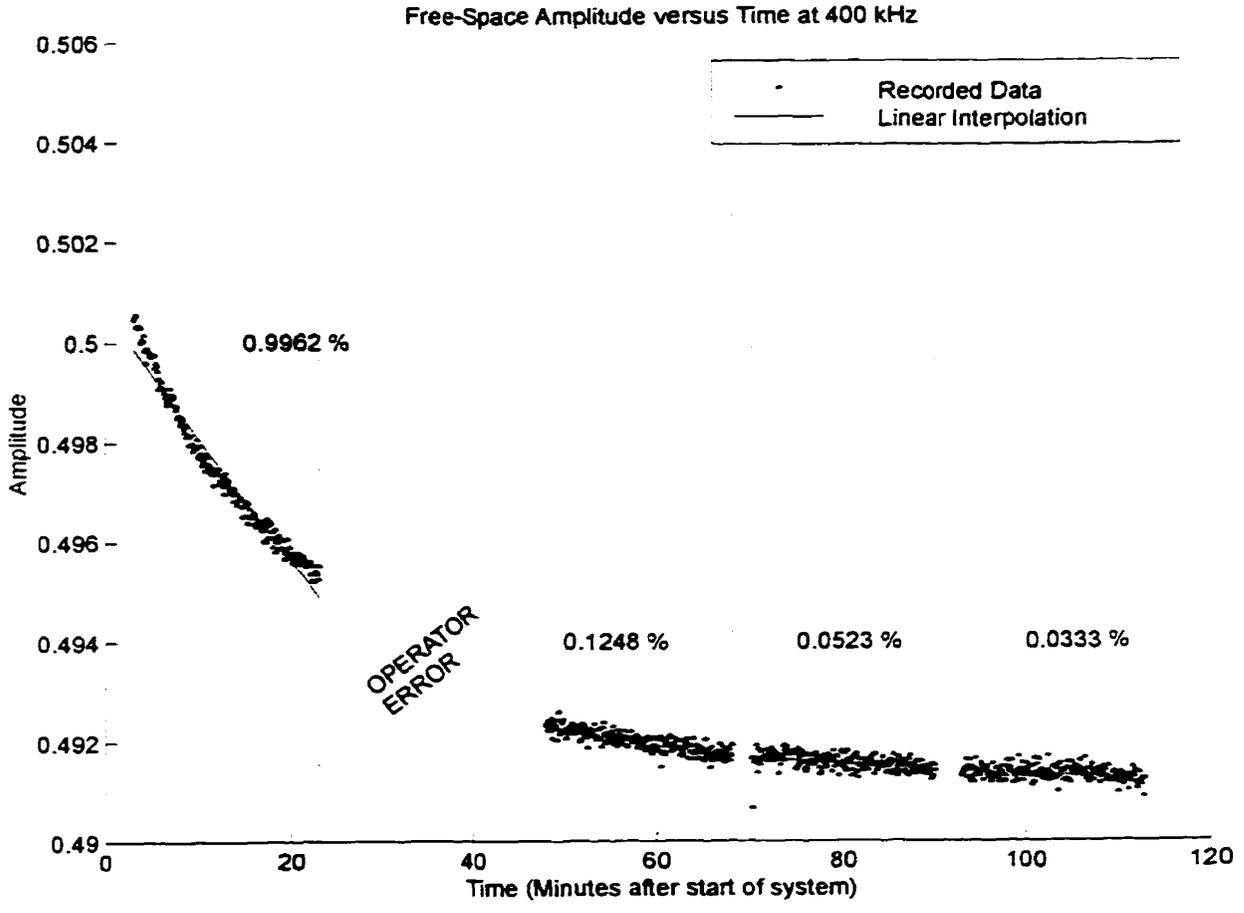

Figure 3-1 : Free-space amplitude versus time at 400 kHz. The decrease in the linear interpolated line from the start to finish is expressed as a percentage of the first point in the window.

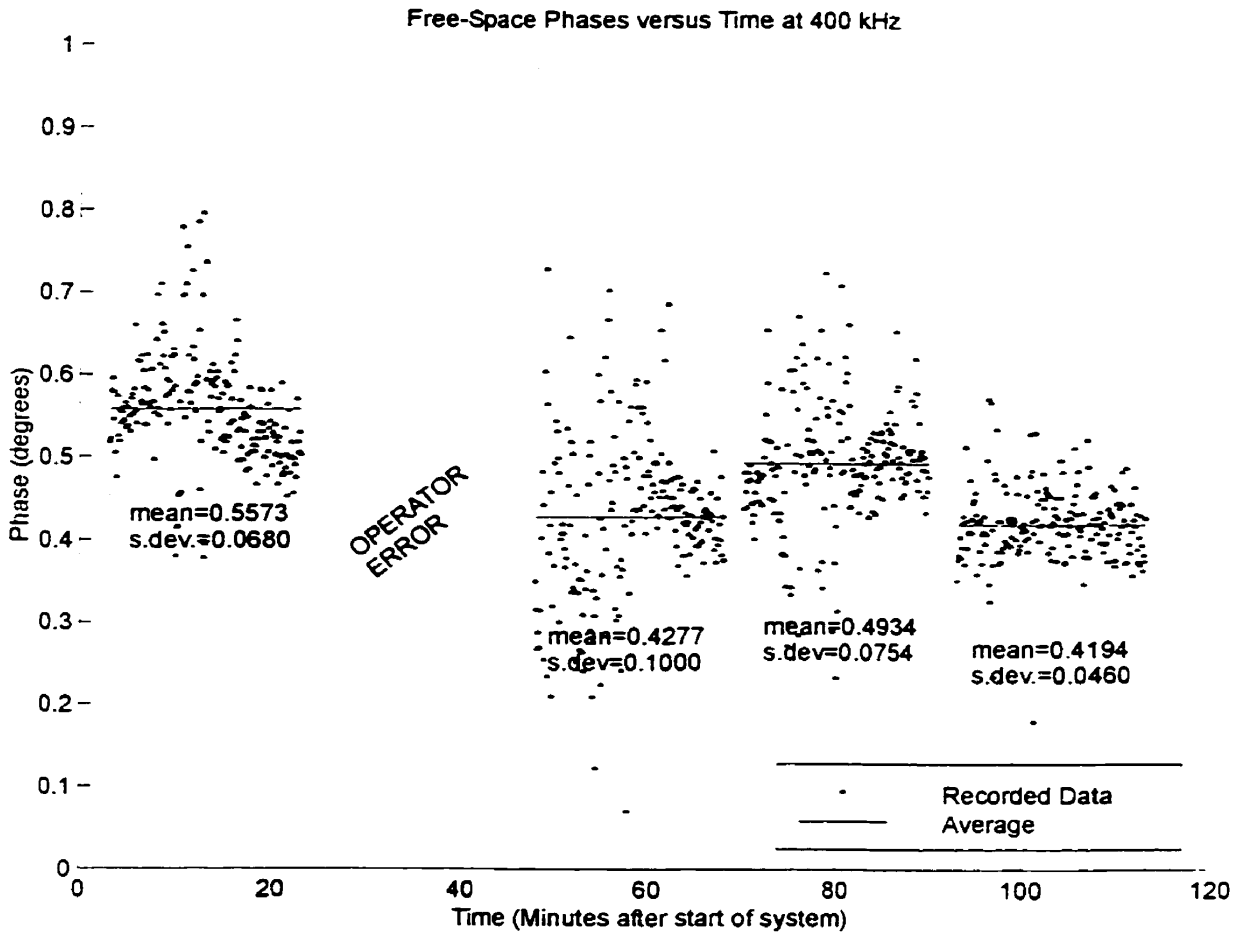

Figure 3-2: Free-space phases versus time at 400 kHz. The solid lines indicate the average value of the phase for each time window. Each time window is labeled with the numerical average.

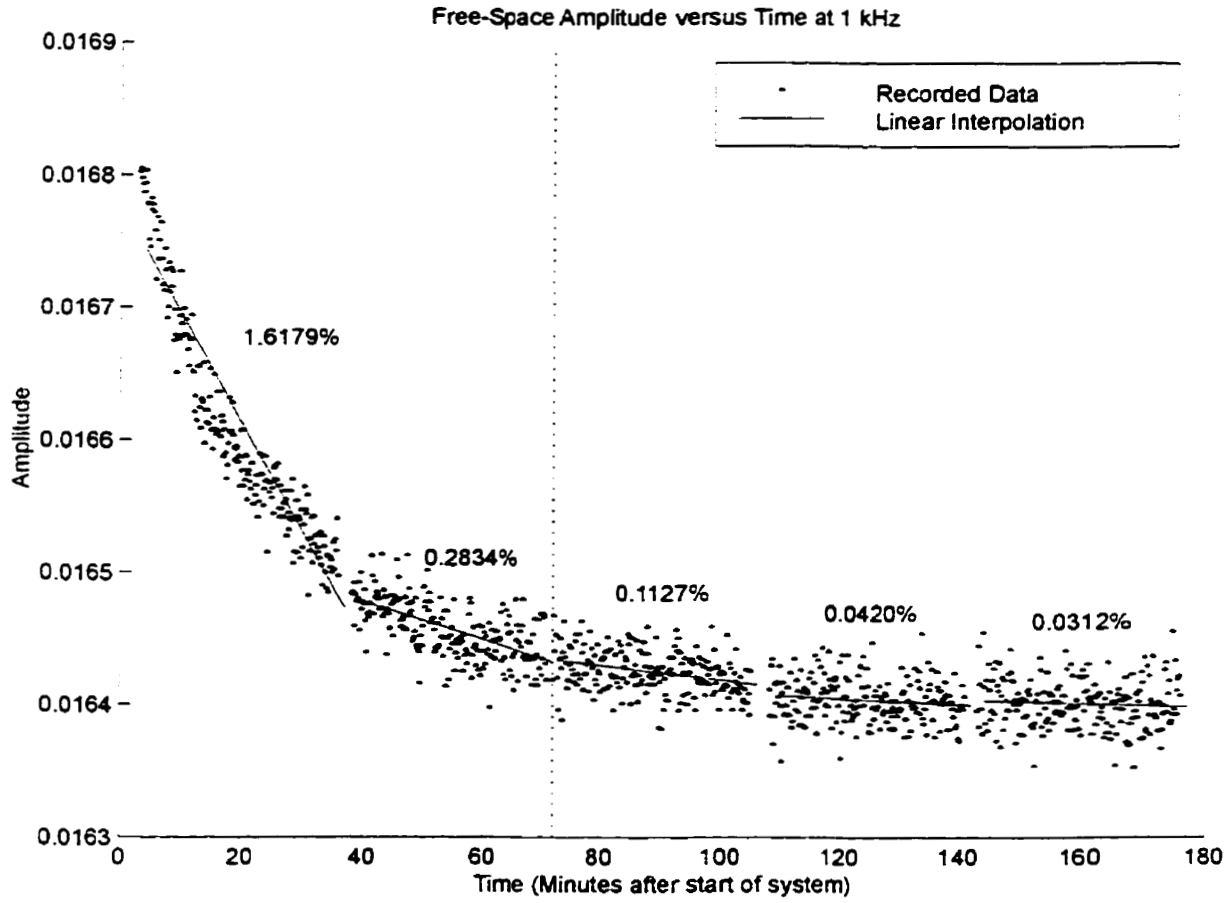

Figure 3-3: Free-space amplitude versus time at 1 kHz. The decrease in the linear interpolated line from the start to the finish is expressed as a percentage of the first point in the window.

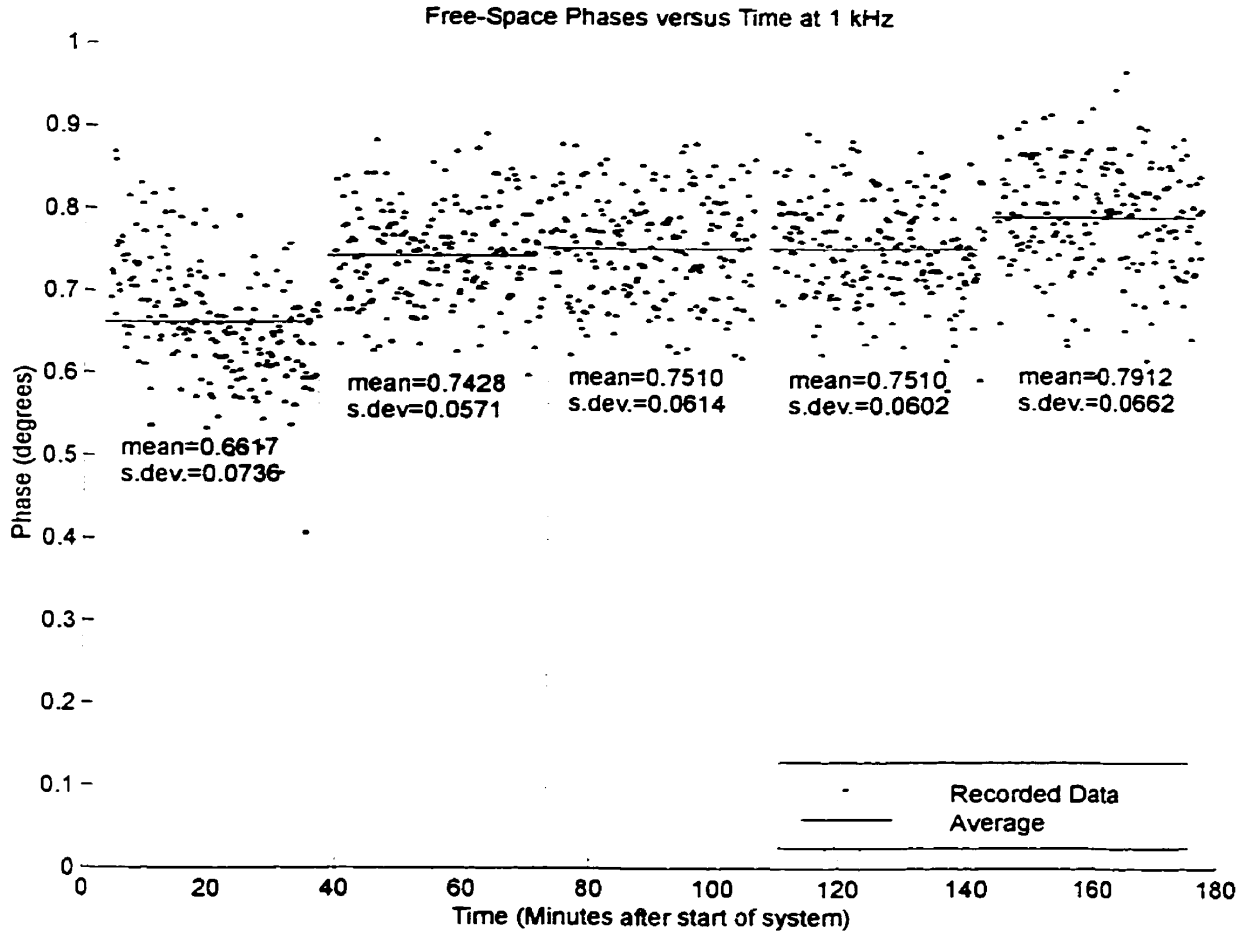

Figure 3-4: Free-space phases versus time at 1 kHz. The solid lines indicate the average value of the phase for each time window. Each time window is labeled with the numerical average.

Table 3-2: Amplitude stability tests at 400 kHz in free-space.

Time Window (minutes)*	Decrease in amplitude (%)**
4-24	0.9962
Data is not available due to operator error	
48-69	0.1248
71-91	0.0523
92-114	0.0333

Table 3-3: Amplitude stability test at 1 kHz in free-space.

Time Window (minutes)*	Decrease in amplitude (%)**
3-36	1.6179
38-71	0.2834
72-105	0.1127
108-141	0.0420
142-176	0.0312

Table 3-4: Phase stability tests at 400 kHz in free-space.

Time Window (minutes)*	Average Phase (Degrees/Standard Deviation)
4-24	0.5573/0.0680
Data is not available due to operator error.	
48-69	0.4277/0.1000
71-91	0.4934/0.0754
92-114	0.4194/0.0460

Table 3-5: Phase stability tests at 1 kHz in free-space

Time Window (minutes)*	Average Phase (Degrees/Standard Deviation)
3-36	0.6617/0.0736
38-71	0.7428/0.0571
72-105	0.7510/0.0614
108-141	0.7524/0.0602
142-176	0.7912/

* the system was turned on at zero minutes

** a straight line was fit through each of the 200 point data sets and the percentage indicates the drop in amplitude from the start of the line to the end of the line with respect to the first point on the line.

3.3 Target Positioning

Accurate positioning of the target, transmitter, and receiver is very important. Free-space models were easier to build than models involving the conductive host because in free-space, it was possible to get close enough to the system to make measurements to within a tenth of a millimeter. To position the free-space target it was clamped to a wooden support and a ruler was taped to the top of the target. The coils were brought close to this ruler and the height of the target support was adjusted. A level was used to ensure the target was horizontal along its length and width, also ensuring the target was vertical.

Errors in target positioning were larger when the target was immersed in the brine solution because the measurements had to be made at a distance of 1.5 m. In the conductive host environment the depth to target errors were minimized by using a measuring stick that rested on the target support platform near the side of the tank (Figure 3-5). The measuring stick was held upright by a loose loop attached to a horizontal beam that allowed it to slide up and down freely. To obtain the zero depth position, the target was lowered until the top of the target was even with the surface of the water, and a mark was made on the measuring stick at the point where it rested against the horizontal beam. Prior to this, the target was leveled by adjusting a set of four screws on the corners of the target platform using the surface of the tank as a reference. The desired depths were measured and marked on the stick so that they could be used to lower the target to the proper depth. This method of target depth placement relied on accurate measurements of the height of the water in the tank.

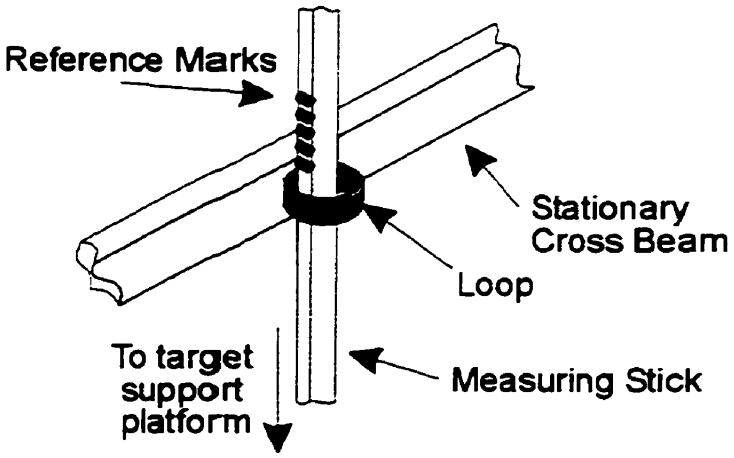

Figure 3-5: The measuring stick apparatus used to set the target depth in the conductive host. The reference marks were spaced 1 cm apart starting at 0 cm. The 0 cm position corresponded to the top of the target being level with the surface of the host. Target depth was set by lining a reference mark up with the top of the stationary crossbeam.

3.4 Preparation of the Brine Solution

The tank of brine had a large surface area, and each day enough water evaporated to lower the tank level by one or two millimeters. A hose was used to fill the tank up to a level that was marked on a small stick hanging from the fixed transmitter. The water level was difficult to measure because there was a meniscus around the measuring device of about one-millimeter. Adjustments of the water level were also complicated by the fact that the water expanded as it warmed to room temperature. An accurate measurement of the water level was important because water level differences of less than one millimeter were shown to affect the recorded data[2]. Most of this effect was

---

[2] A survey done at the end of one day was repeated early the next without the water level being adjusted. The difference between the two resultant field profiles clearly indicated the target's location. This indicated that a small difference in the volume of the conductive host could have measurable effects on the

likely due to the difference the water level made on the height of the coils above it, but some of the effect may have been due to the change in conductivity because of the change in concentration of the brine.

The addition of fresh water and the tendency of the brine to concentrate at the bottom of the tank meant that the solution had to be mixed thoroughly each day. This was accomplished by attaching a trolling motor to the side of the tank. For consistency, the tank was stirred for 10 minutes at a high setting and then let to sit for an hour before measurements were taken.

3.5 Measuring the Conductivity of the Brine Solution

The conductivity of the brine solution was measured with a conductivity cell. The cell consisted of a small rectangular plastic tank with graphite electrodes at either end. These electrodes provided laminar current flow through any material placed in the tank. The tank was partially filled with the solution so that the cross-sectional area of the brine conductor was 4.1 × 8.1 cm. Non-polarizing electrodes were used to measure the potential between two points in the solution. Two different potential electrode separations were used, 19.7 cm and 10.0 cm. Graphite current electrodes at either end of the tank supplied a current. For currents of 51.59 mA, and 51.56 mA respectively, the measured voltages were 0.3067 V and 0.1569 V. If there is laminar flow through a material of constant cross-section, and the potential across a certain length of the materials measured, then the conductivity of the material is given by the following equation

---

response of the target, otherwise the aforementioned surveys should have been identical and their difference would have been uniformly zero.

$$\text{conductivity(Siemens/meter)} = \frac{\text{length(meters)}}{\text{cross}-\text{sectionalarea(meters}^2\text{)}} \times \frac{\text{current(Amperes)}}{\text{potential(Volts)}}$$

Using the above equation the conductivities were calculated to be 9.98 S/m and 9.90 S/m, for an average tank conductivity of 9.93 S/m. These values were in excellent agreement with earlier work (Duckworth and O'Neill, 1989)

3.6 Modeling Procedures

For the purposes of this study, the height of the transmitter and receiver above the host remained constant at 1.8 cm for both devices. The height of the small coils was measured from an annular ring marked around the coil's copper shield to the surface of the host, and the height of the fixed loop transmitter was measured from the windings to the surface (Figure 3-6).

3.6.1 Moving-Source Surveys

Figure 3-7 is a diagram of the model moving-source system. The transmitter and receiver were 1.5-cm diameter multi-turn ferrite-cored coils shielded from capacitative effects by a grounded copper shield. The coils were mounted on a rigid support that allowed the coil separations and orientations to be set manually. The coil separation was set to 20 cm from centre to centre for all surveys. Figure 3-8 is a diagram of a model moving-source survey. The model was placed in a central location along a 1-m long traverse. The resultant field at the receiver was measured at 200 stations with a station spacing of 0.5 cm. The measurement was allocated to the point midway between the transmitter and the receiver.

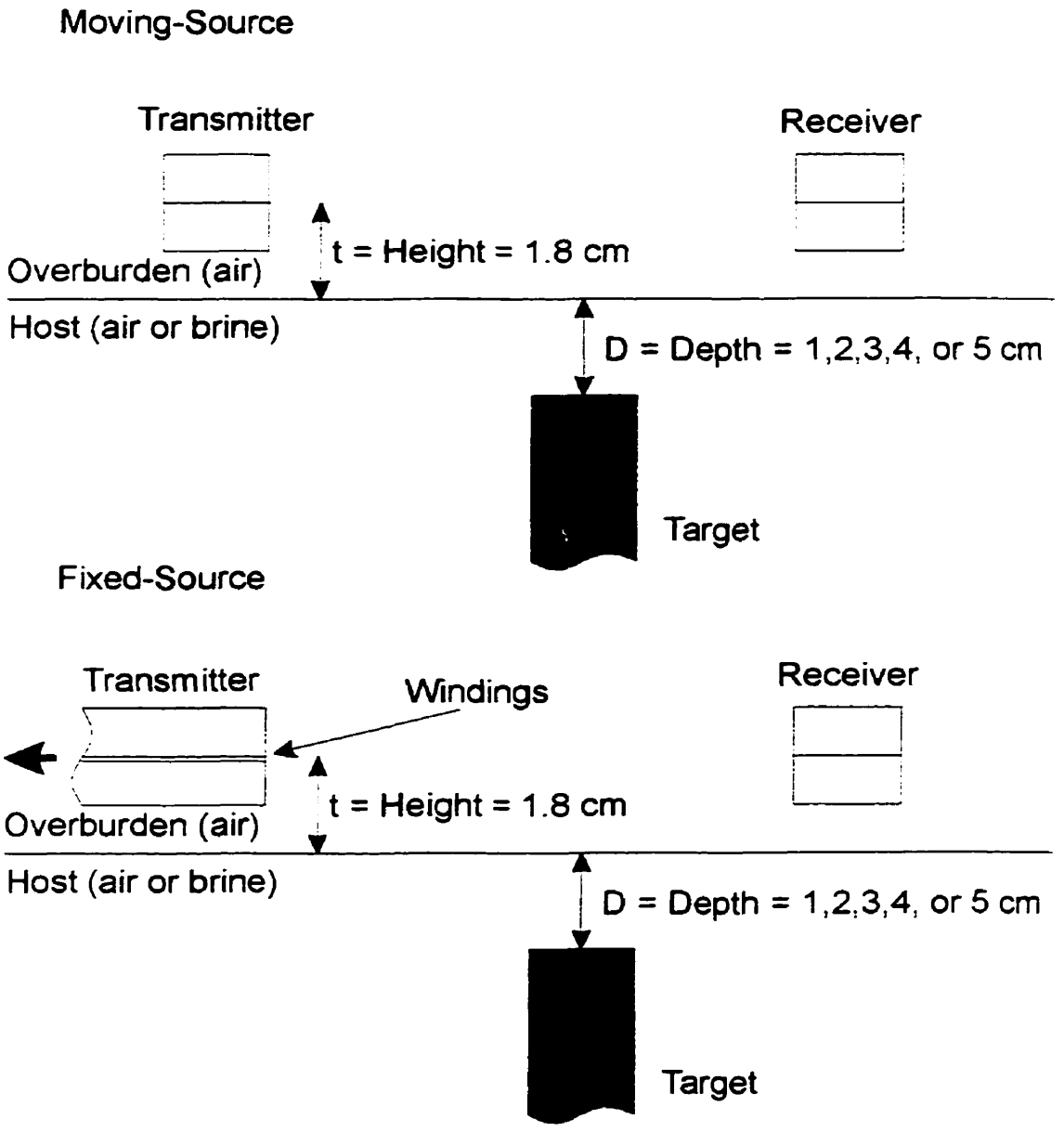

Figure 3-6: Height measurements. The height of the small coils was measured from an annular ring marked around the coil's copper shield to the surface of the host, and the height of the fixed loop transmitter was measured from the wire windings to the surface as shown.

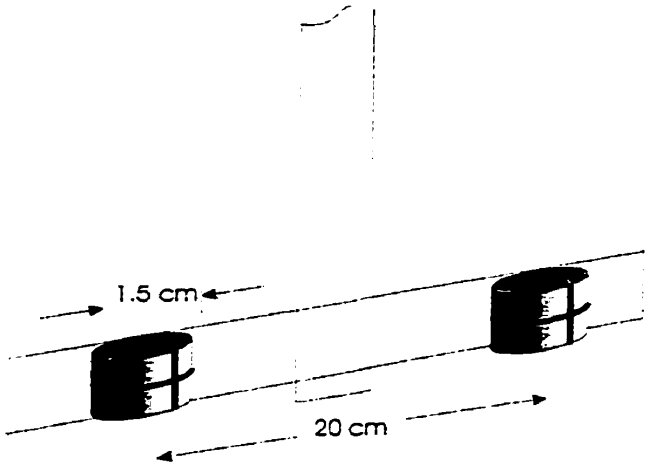

Figure 3-7: The model moving-source system consists of 1.5 cm diameter multi-turn ferrite-cored coils shielded from capacitative effects by a grounded copper shield.

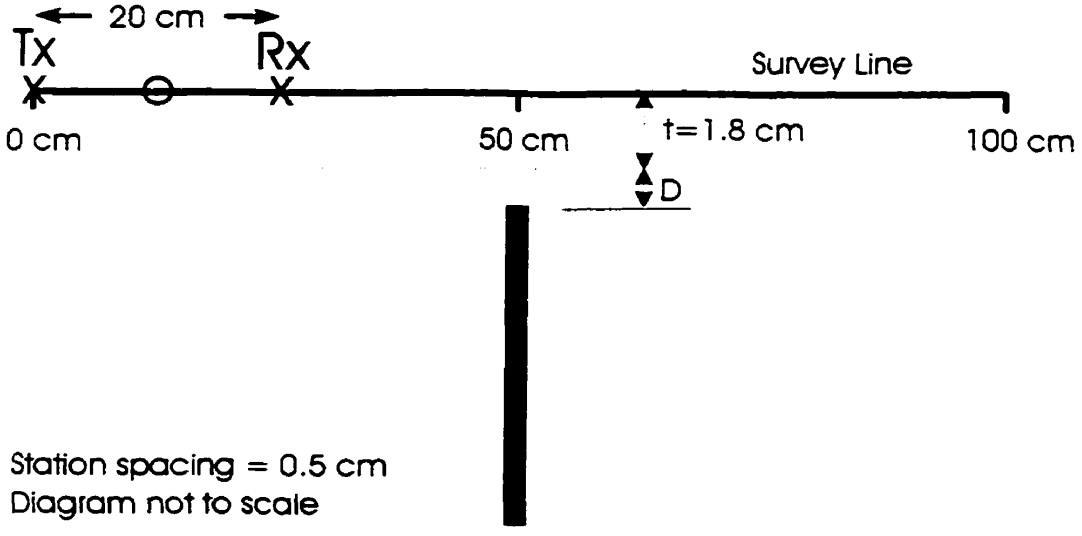

Figure 3-8: A model moving-source survey. The model was placed in a central location along a 1-m long traverse. The resultant field at the receiver was measured at 200 stations with a station spacing of 0.5 cm. The measurement was allocated to the point midway between the transmitter and the receiver (point 'o' on the diagram).

3.6.2 Fixed-Source Surveys

The model fixed-source system is shown in Figure 3-9. For this system, the same receiver was used as for the moving-source system, and the transmitter was a horizontal loop 1-m square. The larger transmitter was necessary because the small moving-source was not powerful enough to excite the target at the distances required. Also shown in Figure 3-9 is a diagram of a model fixed-source survey. The target was always placed in the same location, parallel to, and 60 cm away from, the front edge of the transmitter. The receiver sampled the fields along a line perpendicular to the front edge of the transmitter. The vertical components of the resultant fields (primary plus secondary) were measured at 200 stations, 0.5 cm apart, starting at 19 cm from the transmitter.

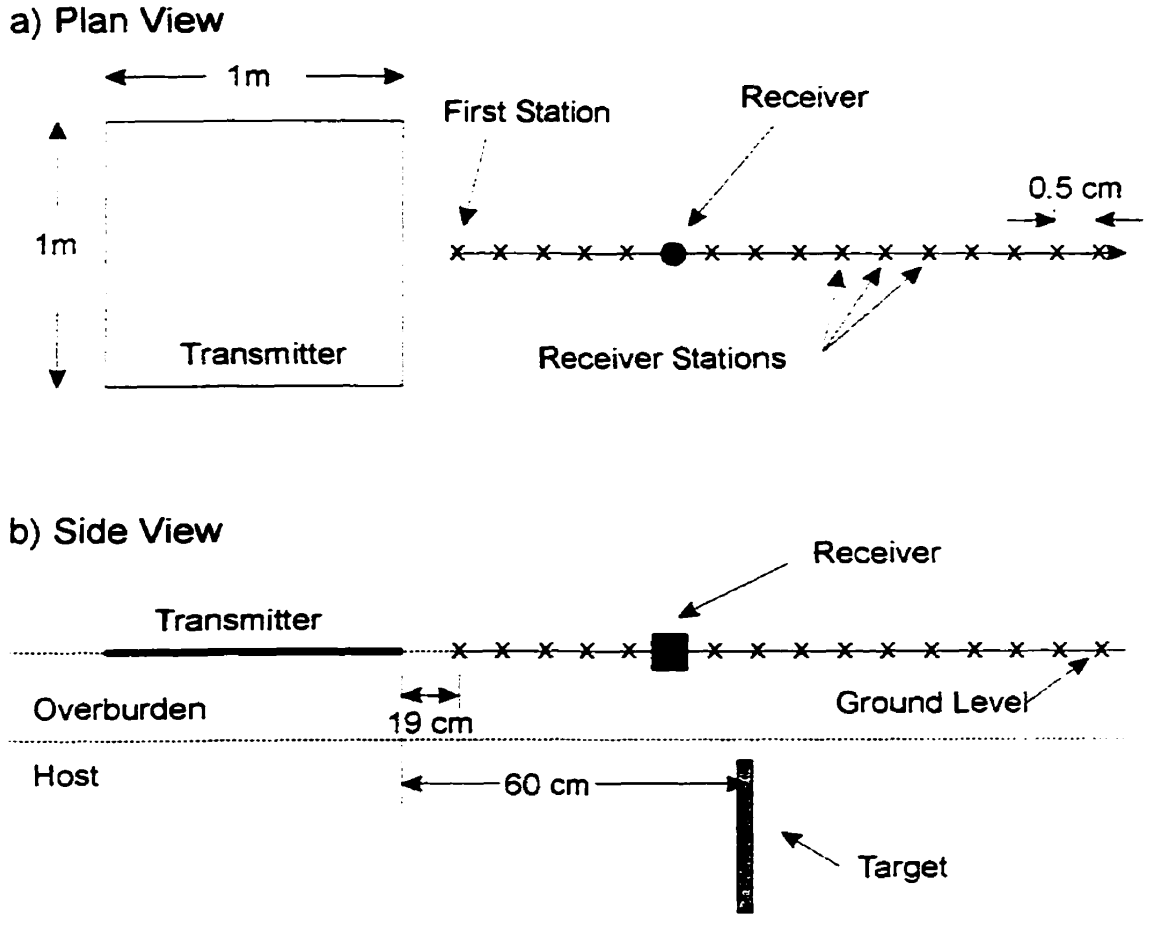

Figure 3-9: The model fixed-source system and survey. The same target and receiver were used here as for the moving-source device. The target was placed 60 cm from the front edge of the transmitter. The survey was 1 m long starting 19 cm from the front edge of the transmitter. The vertical field was sampled at two hundred stations 0.5 cm apart.

Chapter 4

4 Data Processing

This section describes the procedures used in assigning in-phase and quadrature anomaly values to the moving- and fixed-source data.

4.1 Moving-source Data

Figure 4-1 shows typical in-phase and quadrature moving-source profiles, and the associated anomalies, for a tabular conductor in free-space (Figure 4-1a) and in a conductive host environment (Figure 4-1b). Figure 4-1a and 4-1b are for the target at a depth of $D = 1$ cm, and a transmitter frequency of $f = 20$ kHz. For moving-source systems the primary field is constant for each reading and deviations from the constant primary field are due to external sources. In free-space, the profiles tend towards zero percent as the distance from the target increases. When a conductive host is present, the response has a finite non-zero value, which appears as a baseline shift for all profiles taken with the host in place. The baseline shifts due to the conductive host were measured in the absence of the target. In this study, moving-source anomalies were defined as the vertical magnitude (measured in percent) from the baseline to the data point directly over the target as shown by the vertical lines on Figure 4-1.

For the free-space host, the data point directly over the target was the total anomaly since the baseline was zero percent. The anomaly for the target in the conductive host was the sum of the *magnitude* of the host response (with the target removed) and the *magnitude* of the response directly over the target in the host. By convention, the measured in-phase and quadrature components are expressed as a percentage of the free-space primary field. Figure 4-2 shows the in-phase component of physical model data for the target at 1-cm depth in a conductive host environment for the full range of model frequencies. The

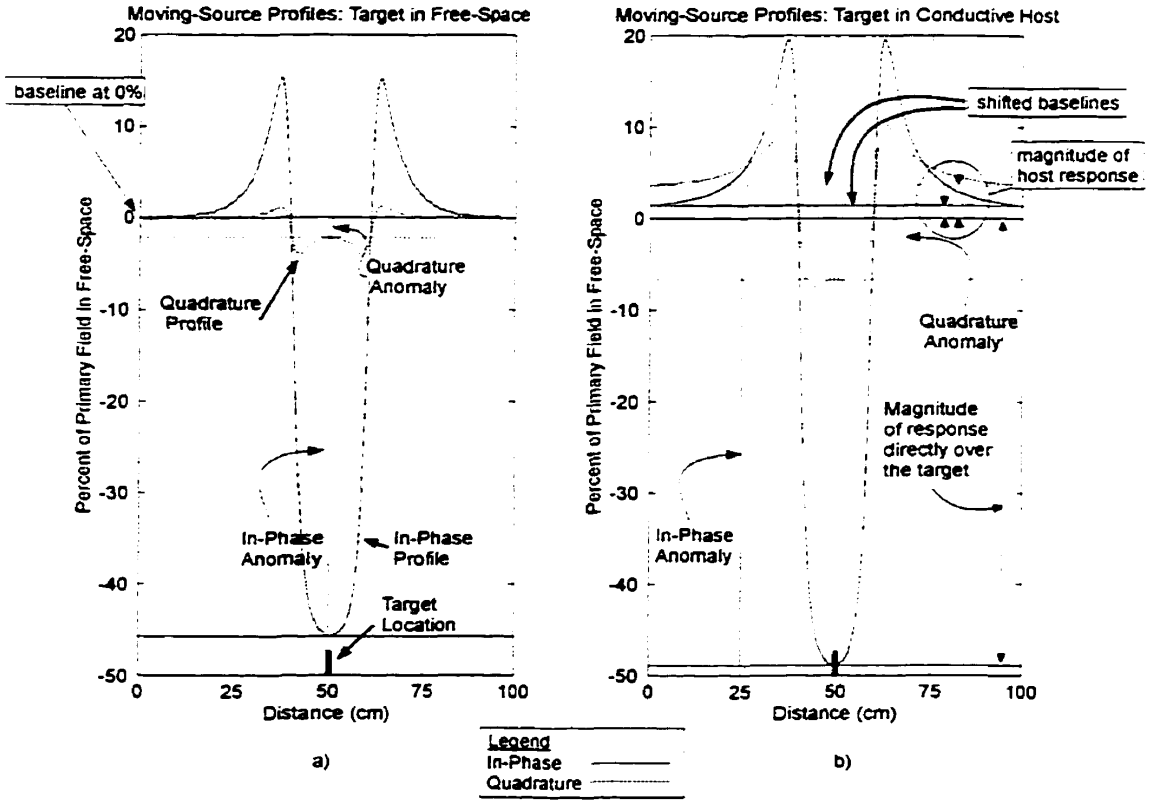

Figure 4-1: Examples of moving-source in-phase and quadrature profiles and anomalies for f=20 kHz, D=1 cm, and a coil separation of 20 cm. a) free-space data, b) conductive host data.

flanks of the 400 kHz data cross over the lower frequency data. This indicates that there was a problem with the in-phase component of the 400 kHz background data. It appeared that the reference for the 400 kHz in-phase data was being reset before the survey began. This effect was repeatable on the modeling system used in this study. Tests on another modeling system that was controlled by a slightly different version of the Quick BASIC program did not show the same effect so a software problem is suspected. No obvious error was located, though there are several hundred lines of code in the program. The background reading is used to remove the vertical baseline shift due to the primary field. A better estimate of the 400 kHz host response was possible by extrapolation from the

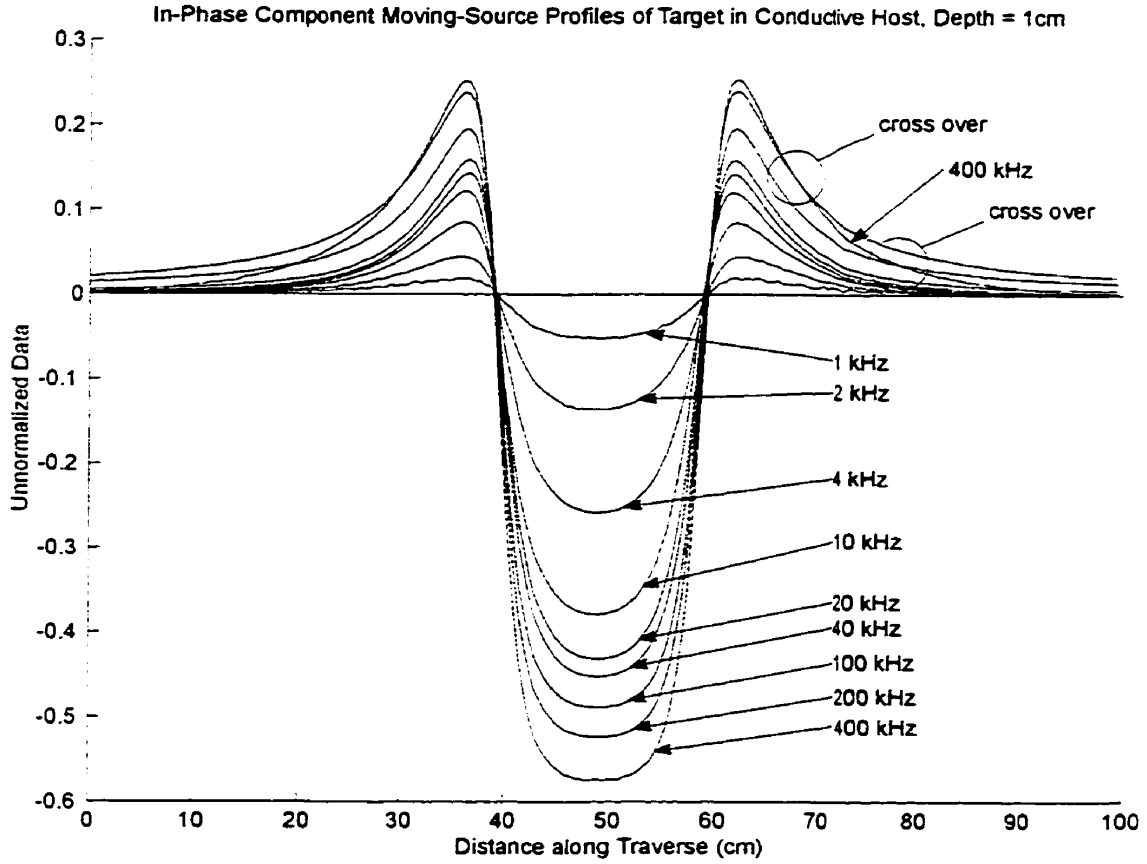

Figure 4-2: In-Phase profiles collected over the target at 1-cm depth in the conductive host. The flanks of the 400 kHz data overlapped the lower frequency data indicating a problem with the free-space reference at that frequency.

lower frequency host responses. Applying the extrapolated 400 kHz background shift to the data results in a vertical shift of the data, but since the baseline-to-peak magnitude does not change with vertical shifts, applying this correction to the data does not affect the magnitude or sign of the measured anomaly. However, it was the erroneous free-space reference that caused the problem, so all 400 kHz moving source data were normalized to the wrong reference, the magnitude of the error caused by this is unknown. The quadrature component profiles (Figure 4-3) did not have an unrealistic baseline shift.

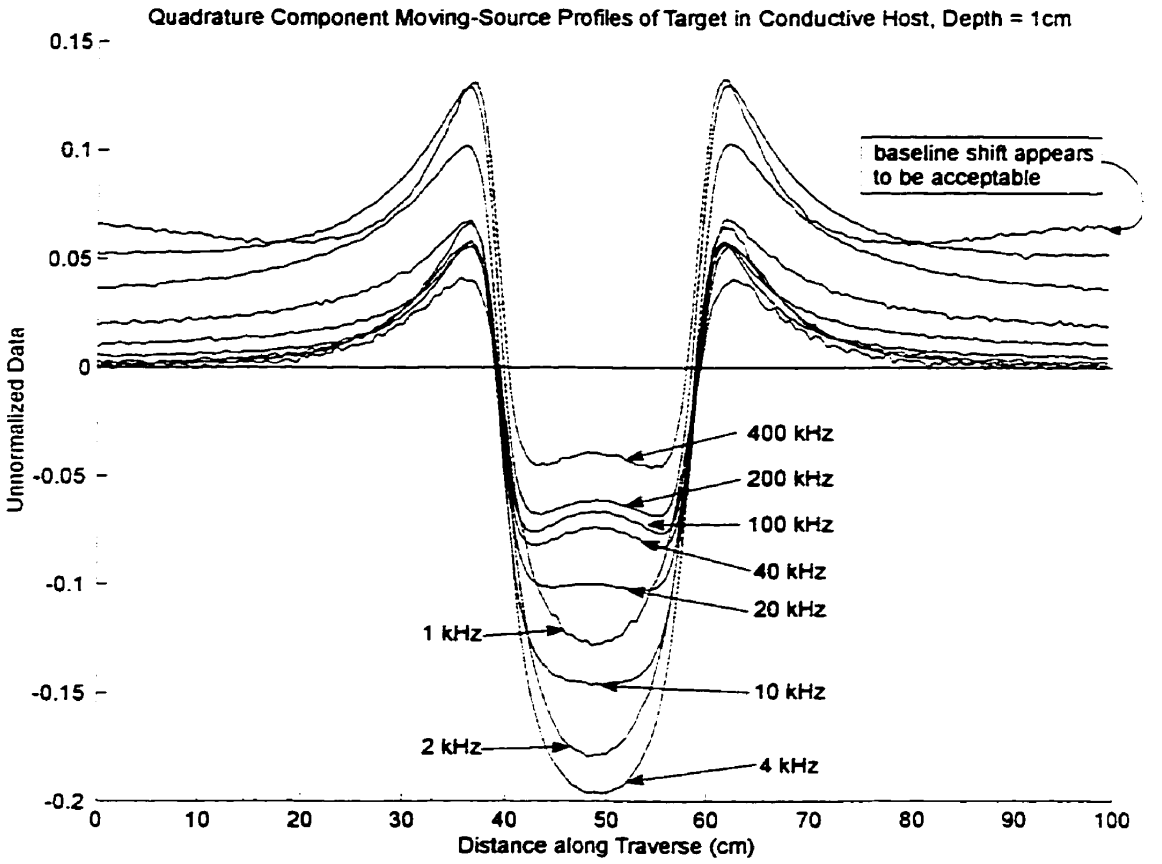

Figure 4-3: Quadrature profiles collected over the target at 1-cm depth in the conductive host. The flanks of the 400 kHz data initially overlap the lower frequency data, but eventually rise above the lower frequency data at far offsets from the target.

4.2 Fixed-source Data

Figures 4-4a and 4-4b provide an example of the fixed-source data acquired by the modeling system for the target at a depth $D = 1$ cm and a transmitter frequency of $f = 20$ kHz. The measured data included the resultant amplitude (Figure 4-4a) and phase

profiles (Figure 4-4b) measured over the host and target, as well as the primary[3] amplitude and phase profiles measured over the host alone. The centre of the target was located 41 cm along the traverse (or 60 cm from the transmitter). The in-phase and quadrature components of the resultant and primary fields at each station were calculated first. Then the in-phase and quadrature components of the primary field were subtracted from the corresponding components of the resultant field. The difference, the secondary field due to the target, was filtered to remove the high frequency (in a spatial sense) noise from the data. The filter caused a slight shift in the lateral location of the target[4].

Figure 4-4c shows the in-phase and quadrature component profiles of the secondary field derived from Figures 4-4a and 4-4b. The in-phase and quadrature anomalies are defined as the vertical distance between the maximum and minimum peaks (See Figure 4–5). An automatic anomaly picking routine determined this vertical distance by subtracting the minimum value from the maximum value. A positive anomaly was defined as one for which the maximum occurred nearer to the transmitter than did the minimum (see, for example, Figure 4-8g). If the minimum was closer to the transmitter than the maximum, the anomaly was considered to be negative (see, for example, Figure 4-5). Prior to the vector subtraction, the primary and resultant field amplitudes were normalized with respect to the first point on the profile. By normalizing in this way it was assumed that the secondary field due to the target was negligible at the first point of the survey. To test whether this was a reasonable assumption, synthetic data were used.

---

[3] The "primary" field due to the host alone is not to be confused with the free-space primary field used for normalization. The host-alone field is required so that the secondary fields from the target may be isolated.

[4] The lateral location of the target is interpreted to be directly below the inflection point on the secondary field profiles.

The synthetic resultant field was calculated by adding the vertical component of the field due to a square loop transmitter (the primary field) to the vertical component of the field due to a line current (an approximation to the secondary field). The line current represented the current that flowed in the upper part of the target along its strike length. The result of processing the synthetic data with the same technique that was used to

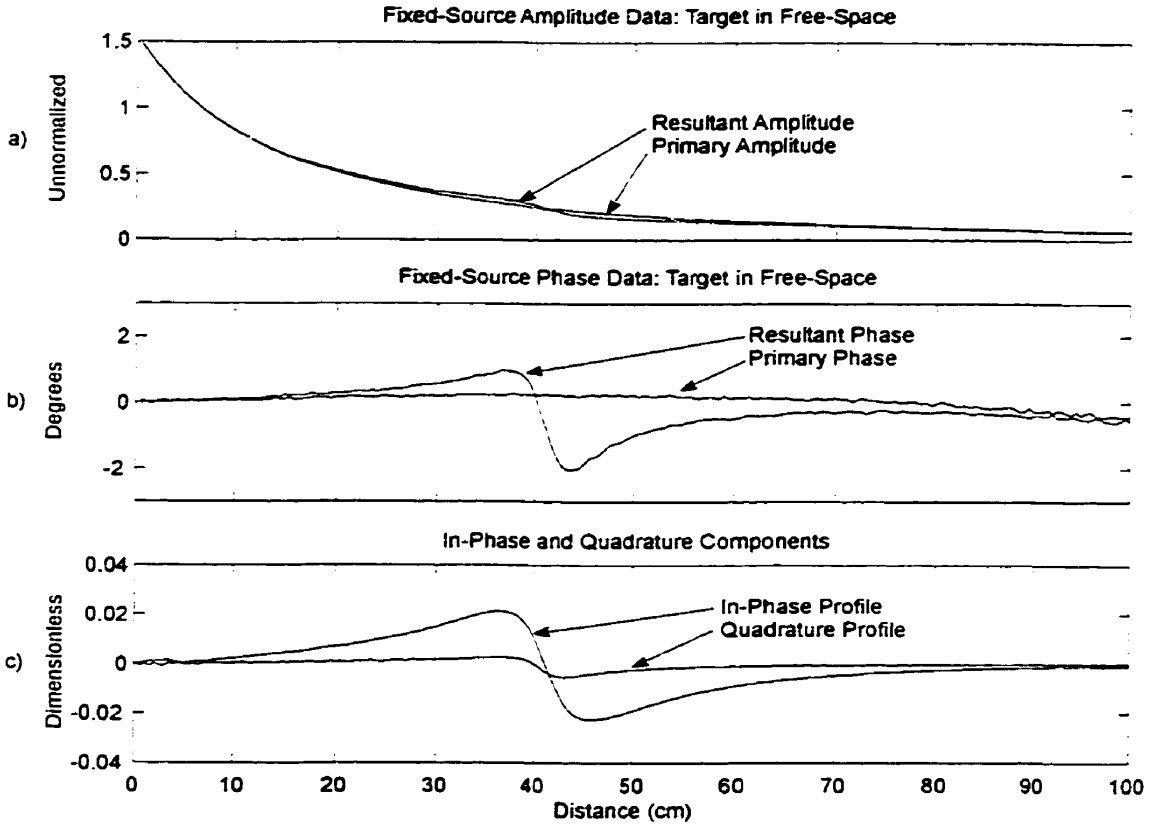

Figure 4-4: Fixed-source data for the target 41 cm from the first station (60 cm from the transmitter), at a depth D=1 cm, with transmitter frequency f=20 kHz: a) resultant and primary amplitudes, b) resultant and primary phase data, c) complex components of the secondary field (the vector difference of the resultant and primary fields). Note: the profiles were smoothed during processing. The smoothing caused a slight lateral shift in

the data, which was ignored because only vertical magnitudes were important in the present study.

process the model data is shown on Figure 4-5. The processed secondary field matched the actual synthetic secondary well. The differences between the actual secondary field and the processed secondary field were most obvious in the in-phase component profile, with the largest differences being near the point that was used for the initial normalization. In the region of interest, however, the agreement was excellent, which indicates that the assumption had very little effect on the data. For this study the fixed-source anomaly was defined as the difference between the maximum and minimum values on the profile. The normalization with respect to the amplitude measured at the first station was necessary in order to remove the effects of the primary field. Finally the anomalies were expressed as a percentage of the normalized free-space primary field at the target location[5].

Figures 4-6 and 4-7 show the processed fixed-source model data for nine frequencies and 5 depth values in free-space. Figure 4-6 shows the in-phase component profiles exhibiting typical line current behavior (for comparison, typical line current behavior is shown in Figure 4-5). The automatic anomaly picking routine worked well in these instances. Figure 4-7 shows the quadrature component profiles. As the frequency increased, the well-defined maximum-minimum response became an asymmetrical response with an ill defined maximum and a sharp minimum (Figure 4-8a to 4-8e). This suggested a transition from the response of a single line current to that of a pair of line

---

[5] The normalizations with respect to the first station amplitude were necessary for the conductive-host data set because the free-space primary field and the conductive host data could not be collected with the same voltage on the transmitter. This is because the conductive host absorbs the fields more effectively than air. The voltage necessary to obtain a clean signal over the conductive host is so high that free-space signals measured with the same transmitter voltage would saturate the pre-amplifier.

currents of opposite polarity. Synthetic data for such a pair is shown on Figure 4-8. Moving from profile a) to profile f) demonstrates the effect of increasing the horizontal distance between two line currents (locations marked with *xs*) of equal but opposite current magnitudes. The apparent rightward motion of the anomaly in Figure 4-8a – 4-8f occurred because only the right-hand current was moved to increase the separation. Profile g) is that of a single line current. If the separation were increased enough, two separate anomalies would become apparent. If the second line current has a magnitude less than the first, the result is an asymmetrical response (Figure 4-9). Comparison of Figure 4-7a through 4-7e to the asymmetrical profile of Figure 4-9 suggests that this paired type of current distribution was causing the change of the form of the anomaly. No attempt was made to fit the measured data with these types of synthetic data.[6]

---

[6] Duckworth (1972, 1988) has shown that this type of curve fitting is quite accurate in determining the location of a tabular conductor.

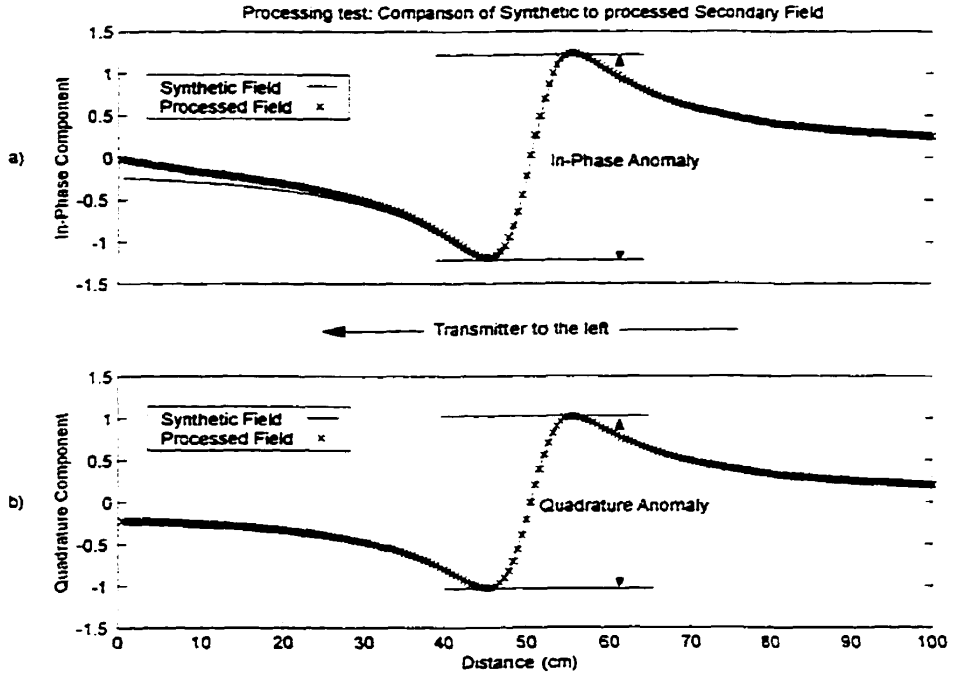

Figure 4-5: Test of the normalization on the processing routine. Normalizing to the first point on the profile causes deviation from the true secondary field in the in-phase component near the first point, but excellent agreement throughout the range of interest. The quadrature component is unaffected.

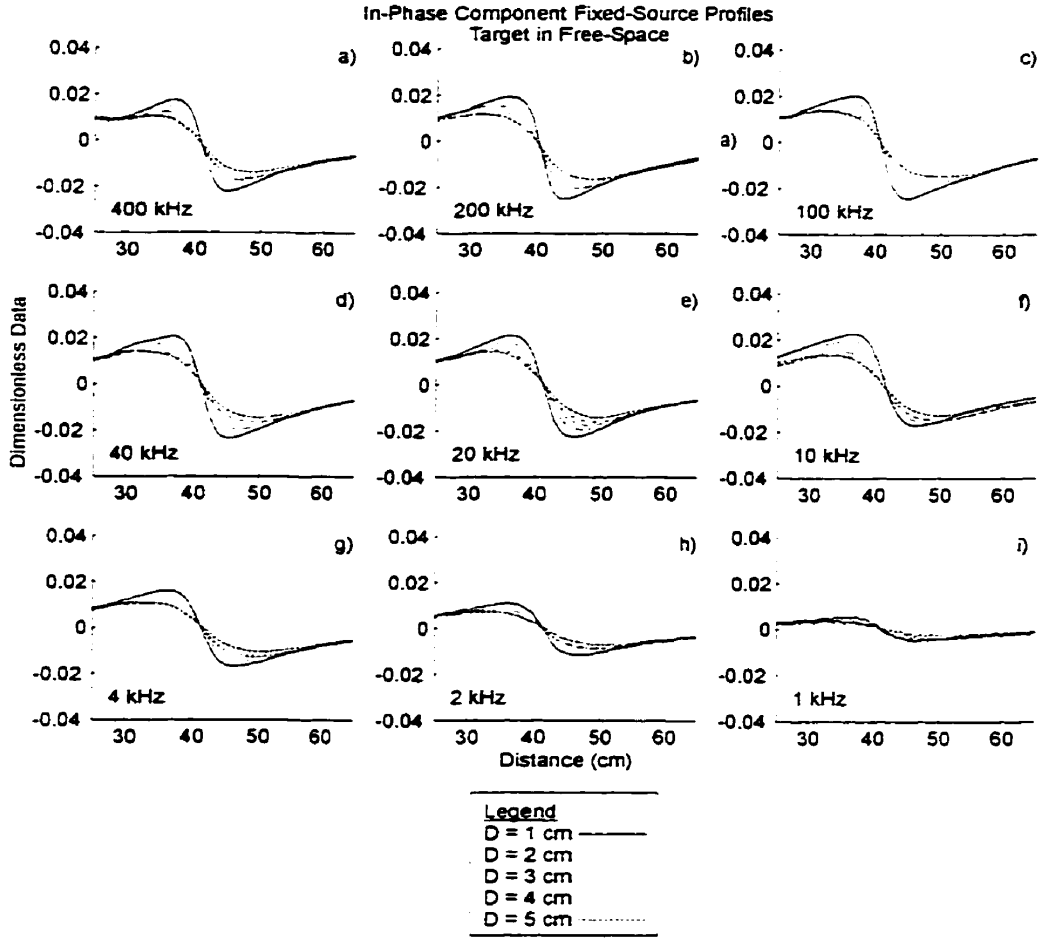

Figure 4-6: Processed in-phase component of the fixed-source data showing typical line current behavior. a) -i) represent data at 400, 200, 100, 40, 20, 10, 4, 2, and 1 kHz respectively.

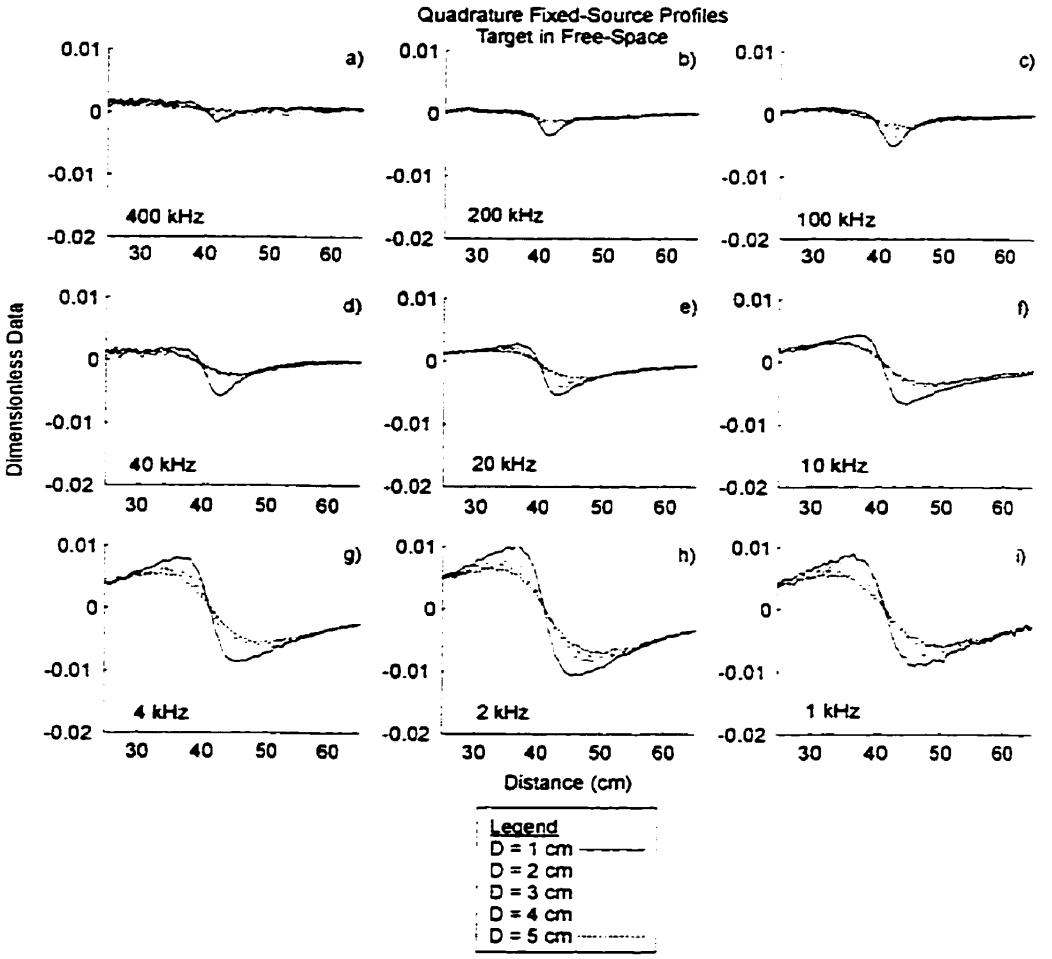

Figure 4-7: Processed quadrature component of the fixed-source data showing line current pair type behavior. a) -i) represent data at 400, 200, 100, 40, 20, 10, 4, 2, and 1 kHz respectively.

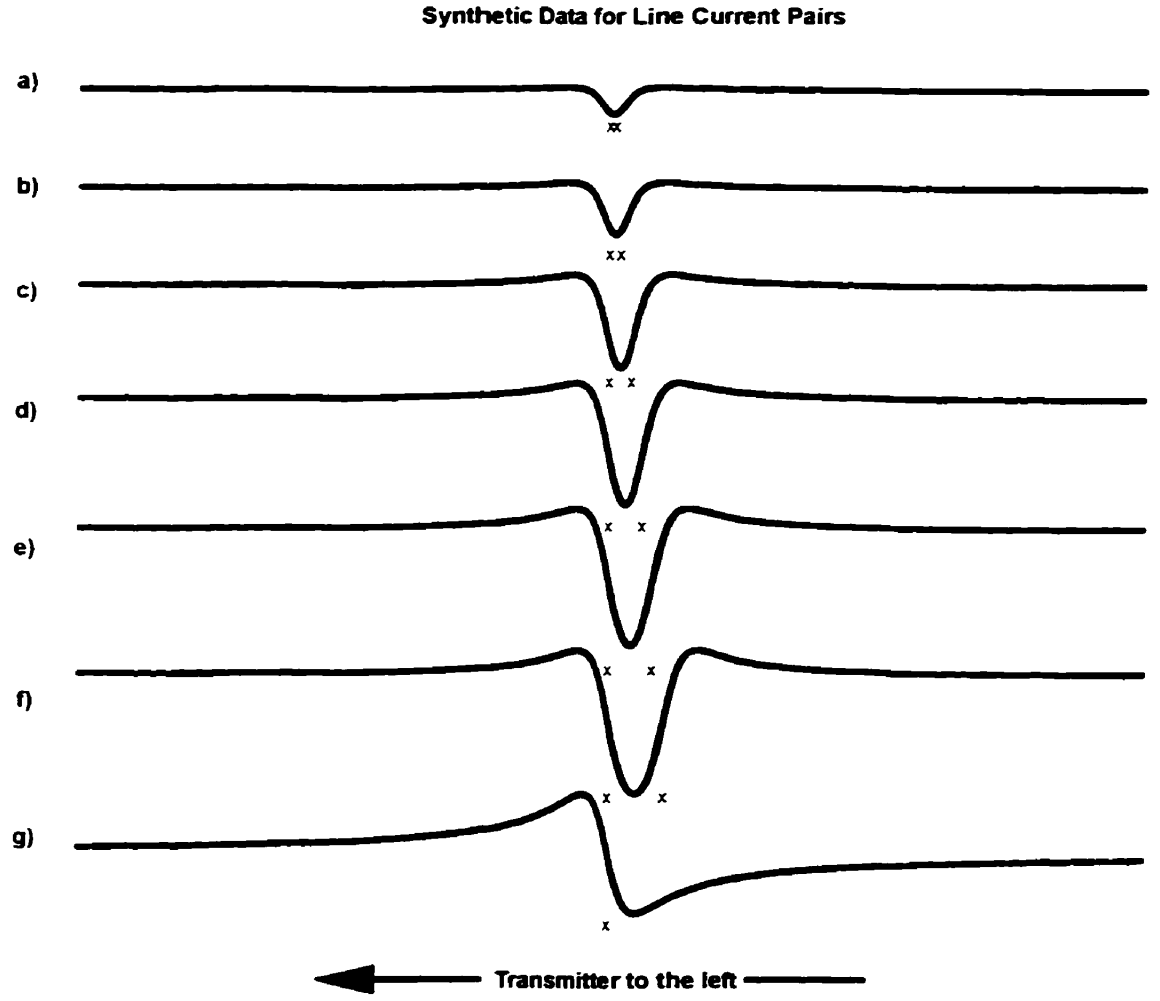

Figure 4-8: Synthetic data for line current pairs of equal magnitude and opposite direction. The right hand side line current was placed further to the right for each plot from a) through f) and the last profile, g), shows just the left hand side line current. The current locations are marked by xs.

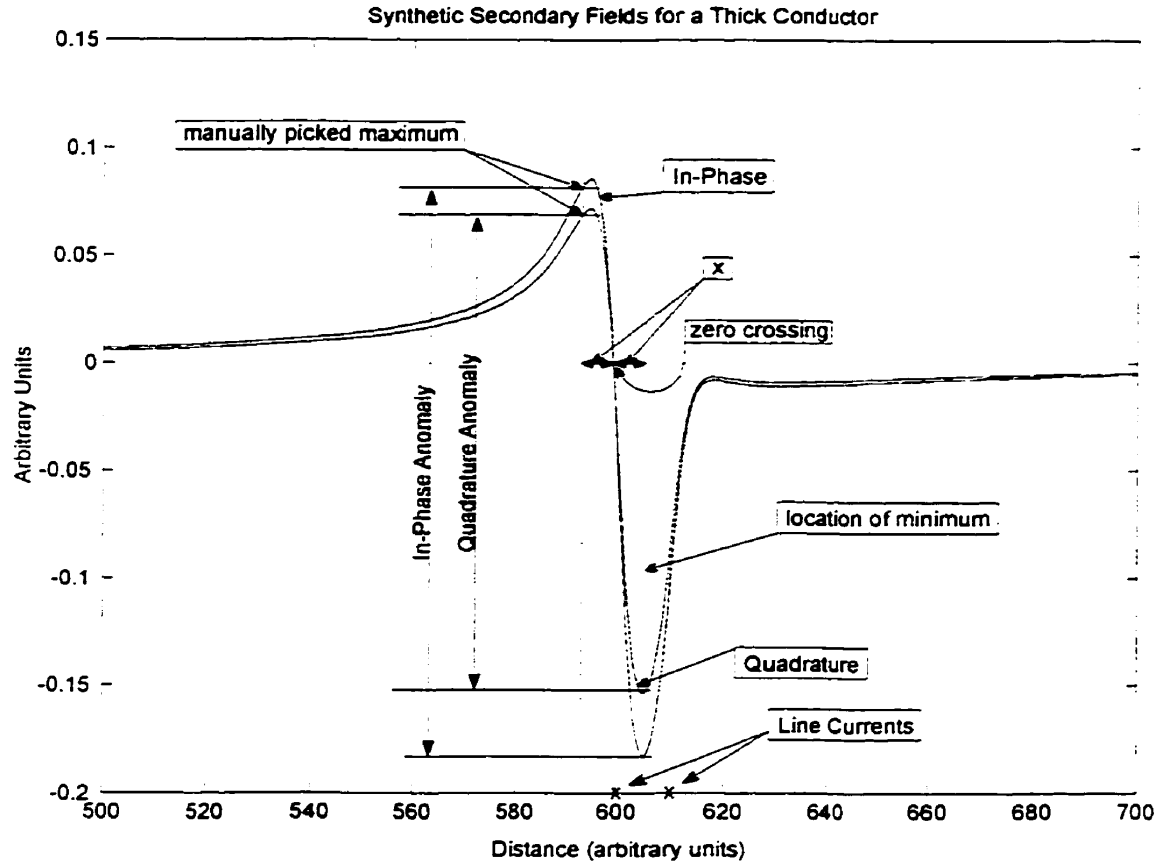

Figure 4-9: Pair of line currents at the same depth. Left-hand side line current is in the opposite direction, and twice as strong as the right hand side line current causing an asymmetrical response. Line current locations are indicated by xs.

The automatic anomaly picking routine works by taking the difference between the local maximum and minimum and assigns the anomaly a sign (positive or negative) based on the relative horizontal location of the two peaks. When the response changed form from a double to single peaked function, the anomalies had to be picked manually. To do this, the lateral distance between the minimum and the zero crossing was determined (distance *x* in Figure 4-9). The maximum value was assumed to be located an equal lateral distance to the other side of the zero crossing (Figure 4-9). As shown on Figure 4-9, this manual method does not guarantee that the location of the maximum will be correct. It

was only used to provide an estimation of the location of the maximum. The maximum value was difficult to determine even with this manual method because of the low signal to noise ratio of the data (Figure 4-7a – 4-7d). Fitting synthetic data to the observed data could be used to provide a more accurate determination of the maximum, but the low signal to noise ratio would mean that there would be a range of solutions which would fit the data. Each solution would have a different maximum value, and the errors would not be reduced enough to warrant this time consuming process.

Chapter 5

5 Results

As discussed in Chapter 4, a target's anomaly is expressed in terms of an in-phase and a quadrature response. The in-phase and quadrature response pair is plotted as a point on an Argand complex space diagram where the in-phase axis is horizontal and the quadrature axis is vertical (Figure 5-1). The vector that represents the anomaly is drawn from the origin to the plotted point. The amplitude of the anomaly is the length of the vector, and the phase of the anomaly is the angle between the in-phase axis and the vector.

For a specific target depth and transmitter frequency, the anomaly due to the target located in a conductive host usually has a different amplitude and phase than the free-space anomaly for the same target depth and transmitter frequency because the host changes the strength, phase, and geometry of the secondary field radiated by the target. To discuss and compare the effects of a conducting host on each of the electromagnetic devices studied in this thesis, the amplitude enhancement ratio (AER) will have to be defined. The amplitude enhancement ratio (AER) is the ratio of the total amplitude of the conductive host anomaly (OC on Figure 5-1) to the total amplitude of the free-space anomaly (OF on Figure 5-1). This gives the factor by which the free-space amplitude must be multiplied to get the conductive host amplitude. An AER greater than one means that enhancements occurred due to current gathered from the conductive host. Attenuations are indicated by AERs less than one. In section 5-2 it was necessary to investigate the AERs of the in-phase and quadrature components of the response separately. For this purpose, the AER of the in-phase component is defined as rC/rF, and the AER of the quadrature phase component is defined as iC/iF. Unless otherwise specified, 'AER' will refer to the total amplitude ratio OC/OF.

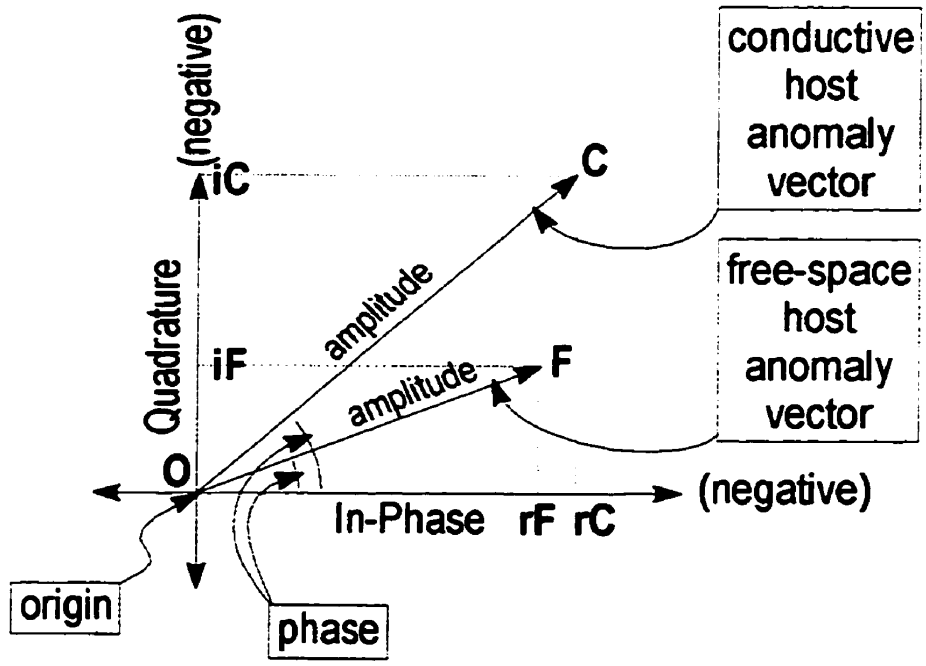

$$\text{Amplitude Enhancement Ratio: AER} = \frac{OC}{OF}$$

$$\text{In-Phase AER} = \frac{O(rC)}{O(rF)}$$

$$\text{Quadrature Phase AER} = \frac{O(iC)}{O(iF)}$$

Figure 5-1: The in-phase and quadrature anomalies are plotted on the horizontal and vertical axis of an Argand diagram. By convention, the axes are both negative. This figure shows examples of two such anomalies, one for the target in free-space and one for the same target in the conductive host. The amplitude of the anomaly is the distance from the origin to the plotted point (in-phase, quadrature), and the phase is the angle between the horizontal and the vector.

It is important to note that even though moving- and fixed-source anomalies are expressed as a percentage of a free-space primary field, there is no basis for direct comparison of an anomaly measured by one device to an anomaly measured by the other

device. This is because the free-space primary field used to normalize the moving-source data is the field that the receiver measures in the absence of the target and host at any location, while for the fixed-source data, the field that is used for the normalization is arbitrarily chosen. For this study, the free-space primary field that was used to normalize the fixed-source data was the field that was measured on the surface at the target location.

Four data sets were collected for this thesis, two for each device (moving- and fixed-source), one for each host (free-space and conductive). These data sets are presented on Argand diagrams (Figures 5-2, 5-4, 5-7, and 5-8). These diagrams indicate the effect of increasing both the target depth and response parameter (the response parameter as defined below was varied by changing the transmitter frequency) of the system. Lines of constant target depth are labeled with the dimensionless parameter g_D where g is the dimensionless ratio of depth to a significant length, L, and the subscript D indicates the depth of the top of the target below the surface of the host in centimeters. L is defined as the coil separation for the moving-source device (by convention), and the strike length of target for the fixed-source device (after Lajoie and West, 1976).

Lines of constant response parameter are labeled α_f, where $\alpha=\sigma t\mu\omega L$, ($\sigma$, t, and μ are the conductivity, thickness, and magnetic permeability of the target, ω is the angular frequency of the transmitter signal), and the subscript f is the frequency of the transmitter signal in kilohertz. The subscripts D and f are only included to aid the comparison of the moving-source to the fixed-source data since $\alpha_{f(moving\text{-}source)}$ does not equal $\alpha_{f(fixed\text{-}source)}$ and $g_{D(moving\text{-}source)}$ does not equal $g_{D(fixed\text{-}source)}$ even though the frequency f, and the depth D, may be the same for both devices. Unless otherwise indicated, all the response parameters were calculated using the manufacturer's value for the conductivity of the graphite target.

5.1 Moving-Source: Target in Free-Space

Figure 5-2 shows the free-space moving-source data that were collected in the present study. For low response parameters the responses were mainly in the quadrature phase. As the response parameter increased, the response of the target became mainly in-phase (this is indicated by the clustering of responses near the in-phase axis on Figure 5-2). This behavior is consistent with that of the simple induction model discussed in Section 2-3. The decrease in amplitude that caused the data to appear to curl under at the two highest response parameters (α_{200}, and α_{400}) was not consistent with thin conductor theory. It has not been determined whether this was caused by the target no longer behaving as a thin conductor, or by an error (or errors) in the Quick BASIC program that controls the modeling system (see Chapter 4.1). The skin depth of the graphite at 100, 200, and 400 kHz is 6.34, 4.48, and 3.17 mm respectively and the graphite is 1.45 cm thick so it is reasonable to assume that the target will behave as a thick conductor at these high frequencies.

To determine whether the modeling system was giving reasonable results, a comparison was made to earlier work by Nair et al. (1968). Figure 5-3 shows moving-source data from the present study, as well as data from Nair et al. (1968). The relative position of the arcs of constant depth to coil separation for each of the data sets is in agreement from α_2 to α_{400}. The agreement is evidenced by the fact that the depth to separation ratio increases as the distance from the origin decreases for the combined data-set. For low response parameters (*Nair 1*, α_1, and *Nair 2*), there is little agreement as the results from the present study have larger amplitudes than the Nair et al. data. The radial lines of the data from the present study are labeled, as on Figure 5-2, by α_f, and the radial lines from Nair et al. are labeled *Nair n*, where the *n* indicates the order (from left to right) in which the radial lines occurred. The actual values of the response parameters are presented in column 2 of Table 5-1 in the order that they occurred. It is clear from column 2 that the response parameters of the two data sets are not consistent. Bold numbers in Table 5-1,

column 2, indicate the response parameters from the present study that are out of order when compared to the Nair et al. data. This indicates the difficulties of obtaining accurate values of the conductivity factor of the response parameter. The α_f values in

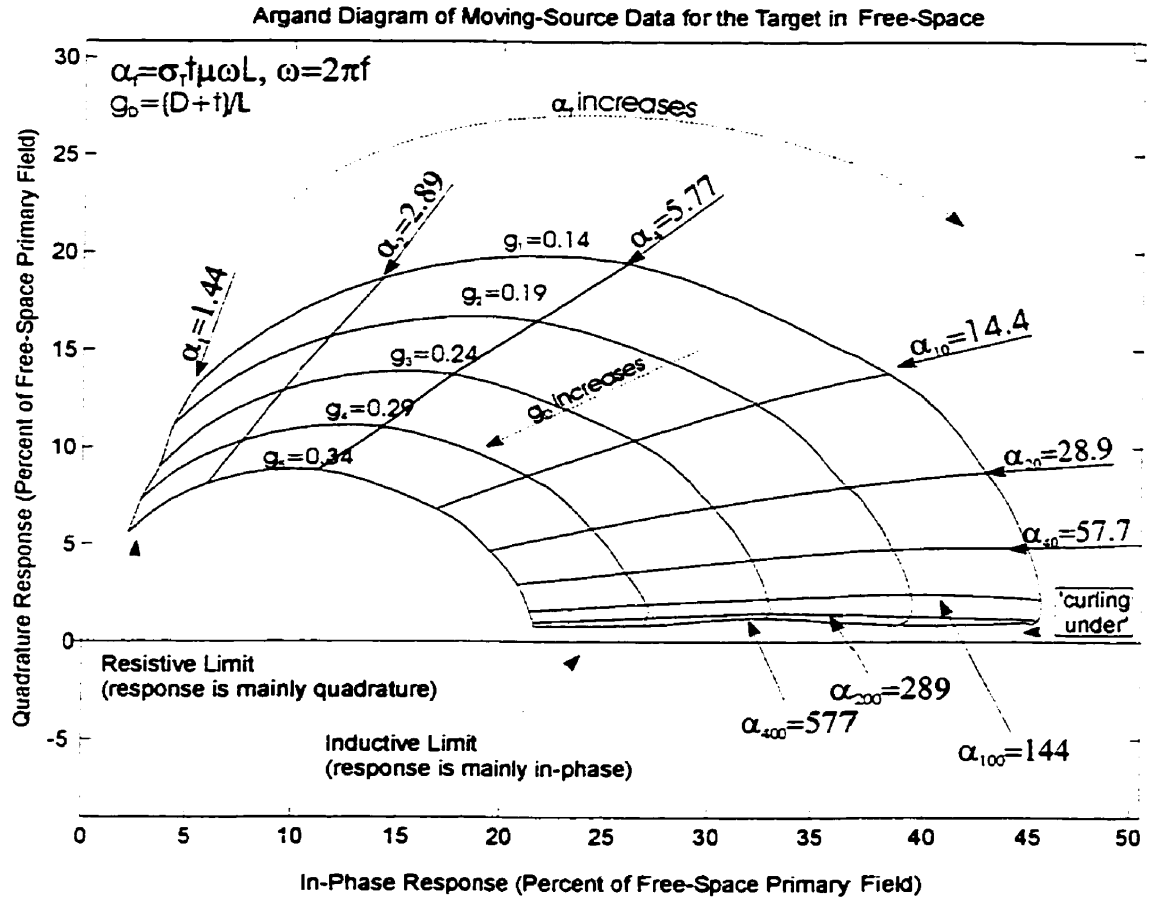

Figure 5-2: Argand diagram for the target in free-space surveyed by the moving-source device. The response parameter α_f increases along the arcs in a clockwise sense. The depth to separation ratio increases towards the origin along the radial lines. As the response parameter increases, the responses had a smaller quadrature component and a larger in-phase component. The curling under for α_{200}, and α_{400} is not consistent with thin conductor theory.

column 2 of Table 5-1 were calculated based on the manufacturer's value for the conductivity of the graphite target (6.3×10^4 S/m, σ_a). Estimates of the conductivity of the target were made for the α_1 to α_{40} data using the Nair et al. results. The average target conductivity (based on data from the six lowest frequencies) was found to be 1.54×10^5

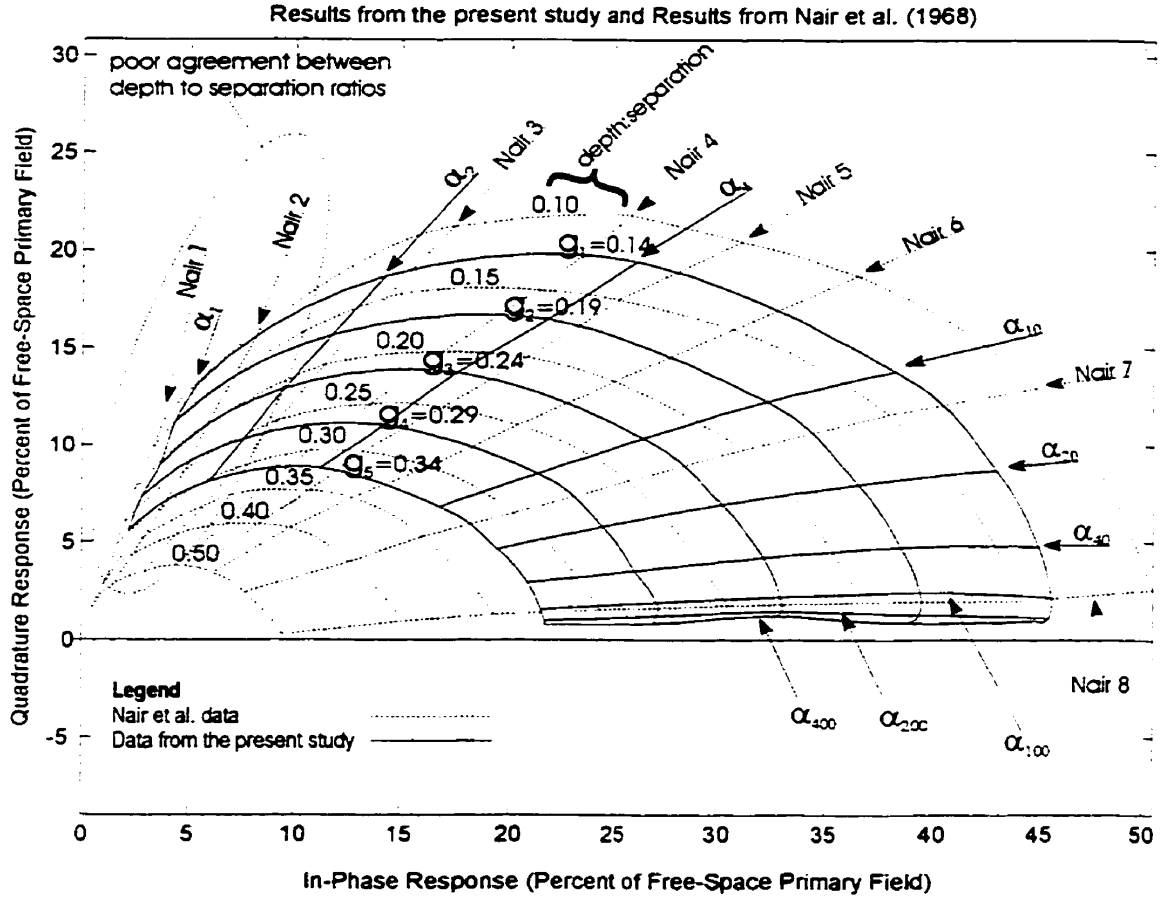

Figure 5-3: Data from the present study and data from Nair et al. (1973). For α_2 to α_{400} the arcs of constant depth to coil separation ratios are in relatively good agreement, increasing towards the origin for the combined data-set. The actual values of the response parameters are given in Table 5-1. Nair et al.'s results suggest the manufacturer's value for the graphite conductivity of the present study was too low.

S/m (σ_b), resulting in the response parameters shown in Column 3 of Table 5-1. The bold values for 1, 2, 4, and 10 kHz show response parameters which are out of order with respect to the Nair et al. Data. This indicates that this average conductivity was not a good estimate. The α_{20} and α_{40} conductivities that were included in the average were

Table 5-1: Response Parameters from Figure 5-2 (as they appear from left to right) calculated using σ_a, the manufacturer's value for the conductivity of the graphite, σ_b, the average value for the six lowest frequencies used in the present study estimated from Nair's data, and σ_c, the average value for the four lowest frequencies used in the present study estimated from Nair's data.

Response Parameter Label	$\sigma_a t\mu\omega L$ $\sigma_a=6.3\times10^4$ S/m	$\sigma_b t\mu\omega L$ $\sigma_b=1.54\times10^5$ S/m	$\sigma_c t\mu\omega L$ $\sigma_c=1.02\times10^5$ S/m
Nair 1	*1.6*	*1.6*	*1.6*
α_1	**1.44**	**3.53**	2.34
Nair 2	*2.6*	*2.6*	*2.6*
α_2	2.89	**7.05**	4.67
Nair 3	*5.3*	*5.3*	*5.3*
Nair 4	*7.9*	*7.9*	*7.9*
α_4	**5.77**	**14.10**	9.34
Nair 5	*10.5*	*10.5*	*10.5*
Nair 6	*15.8*	*15.8*	*15.8*
α_{10}	**14.4**	**35.3**	23.4
Nair 7	*31.6*	*31.6*	*31.6*
α_{20}	**28.9**	70.5	46.7
α_{40}	57.7	141.0	93.4
Nair 8	*316*	*316*	*316*
α_{100}	**144**	353	**234**
α_{200}	**289**	705	467
α_{400}	577	1410	934

Italics indicate Nair et al. results.
Bold indicates results from the present study that are out of order with respect to Nair et al.

difficult to estimate due to the lack of data between *Nair 7* to *Nair 8*. If the conductivities estimated by using *Nair 7* and *Nair 8* were not included, the average conductivity became 1.02×10^5 S/m (σ_c) and the response parameters for this conductivity are shown in column 4 of Table 5-1. It appeared that the lower average conductivity (1.02×10^5 S/m) was more reasonable than the manufacturer's value of 6.3×10^4 S/m. Without a direct measurement of the graphite's conductivity, it is not possible to say which response parameters, *Nair 1* to *Nair 8*, or α_1 through α_{400}, were more accurate.

5.2 Moving-Source: Target in a Conducting Host

Figure 5-4 shows both the free-space and the conductive host data on the same Argand diagram. Because the target, the transmitter frequencies, and the target depths were the same, the α_f and g_D values did not change with the introduction of the conductive host. It is important to remember that responses presented in Figure 5-4 represent the response of the target alone. The background response of the host has been removed. Comparison of the two sets of data shows that the host had little effect on the data from α_1 to α_4. The physics of the situation would suggest that any host with a finite conductivity should affect the response of the target, though, for low frequency and low host conductivity, the magnitude of the effect would be very small. The lack of any measurable effect on the low response parameter data may be explained if the effect was too small for the system to measure, or if experimental errors masked the host effects by causing errors of the same magnitude but opposite sense to that of the host responses. Though the same coils, target, target depths, and coil separations were used to obtain the conductive host data and the free-space data, some errors arose because the target and coils had to be moved between the free-space modeling apparatus and the conductive host apparatus. The difficulties in making accurate position and depth measurements for the target in the conductive host environment have been discussed previously in Section 3-3, and will not be repeated here. However it was unavoidable that the depth of the target and the height

of the coils were slightly different for the target in each host. These differences are thought to be the cause of a repeated pattern seen on Figure 5-5 (maximum AER at 2 cm or 3 cm, minimum AER at 4 cm). These errors would have been minimized if the conductive host could have been introduced into the free-space system after the free-

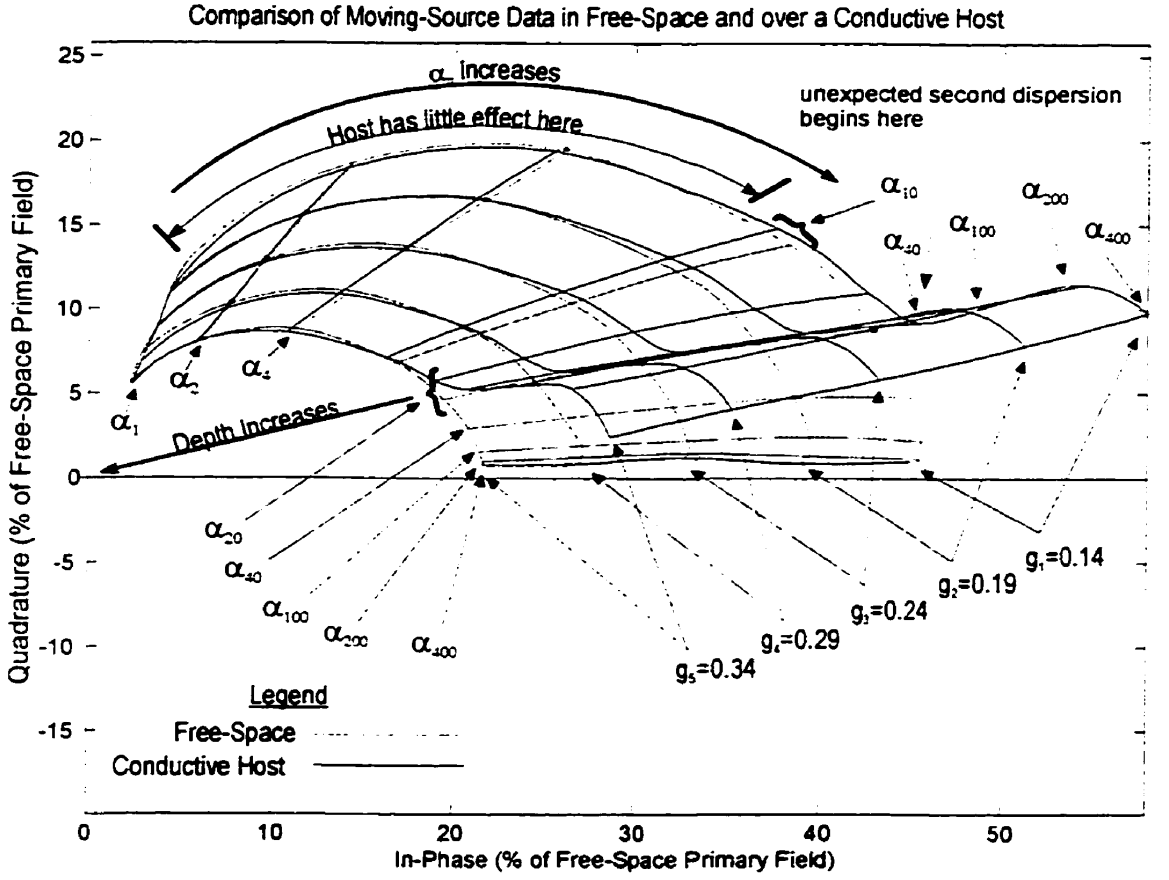

Figure 5-4: Moving-source Argand diagrams for the target in a free-space and in a conductive host. All the anomalies shown are due to the target. Primary and background fields due to the host have been removed. The differences shown are due to changes in the induction and conduction currents in the target due to the different hosts. The second dispersion that begins at α_{40} was unexpected.

space data had been collected. This wasn't practical because several thousand liters of brine were used to model the conductive host, so the target, transmitter, and receiver had to be moved between the two systems. Though no investigation into the effect of small changes in depth was performed, an estimate of the effect may be obtained by using a linear interpolation between the points on the radial lines of Figure 5-4. Error bars of ± 1% could easily be generated if the difference in the depth was actually ±1 mm from what it was supposed to be. It is possible that the depth discrepancies combined with coil height discrepancies could have caused a height difference of about 1-mm.

Another possible source of error related to the repositioning of the model, and could have been caused by the orientation of the transmitter and receiver coils. A leveling device was used to orient the transmitter and receiver horizontally, but errors were inherent in this method since determining when the coil was level relied on centering the air bubble in the window of the leveling device. If the transmitter-target orientation had been slightly different for the free-space system than it was for the conductive host system, the induced fields would also have been different. Also, if the curvature of the resultant electromagnetic field lines at the receiver is strong, a tilted receiver will measure fields that are larger or smaller than the true vertical component that was desired. In summary, height discrepancies, coil positioning errors, background value errors, and the large skin depth of the host may have combined to cause the lack of host-related response at and below 4 kHz.

From α_{10} to α_{20}, the anomaly vectors for the target in the conductive host were rotated counterclockwise with respect to the corresponding anomaly[7] vectors for the target in free-space. At these response parameters (α_{10} and α_{20}) there was little change in

---

[7] For the same target at the same depth and with the same transmitter frequency, corresponding anomalies were generated by the change of the host material.

anomaly amplitude. From α_{40} to α_{100} the counterclockwise phase rotations became larger and the anomalies due to the target in the conductive host had larger amplitudes than the corresponding anomalies for the target in free-space.

The response parameter for a frequency of 40 kHz (α_{40}) marks the transition between the first dispersion[8] (α_1 to α_{40}) and the second dispersion (α_{40} to α_{400}). Duckworth and Krebes (1997) measured a double dispersion with earlier physical modeling but the author is unaware of any other work that has shown a double dispersion. Duckworth and Krebes postulate that a double dispersion may occur if the target and host conductivities are such that the target response approaches its inductive limit as frequency increases before the host response has been able to move away from its resistive limit. That the host alone was responsible for the second dispersion was supported by the fact that the onset of the second dispersion occurred at the same frequency for different target conductors.[9]

Physical scale modeling results from Gaur and Verma (1973) showed the effects of varying the depth of the target and the conductivity of the host. Direct and quantitative comparisons can not be made between Gaur and Verma's work and the results of the present study because of the differences in the target response parameters, host response parameters, and transmitter-receiver heights. In addition, Gaur and Verma's measurements and definitions of the anomaly were very different than those used in the present study. In Gaur and Verma's study, the primary field over the host was removed before the target was surveyed, and the anomaly was expressed as a percentage of the

---

[8] A target's dispersion is the locus of the tip of the anomaly vector as the response parameter is varied.

[9] The second dispersion is only obvious because the target is present, and in this sense, it is not solely dependent on the host material.

field above the host. Even with these differences, there is good general agreement between the two sets of data. Gaur and Verma described the expected decrease in the target anomaly magnitude with depth in both a free-space and conducting host. They found that the anomaly magnitude decreased faster in the free-space environment than in the conductive host environment. Data from the present study support this observation. The bar graph of Figure 5-5 shows the relationship between the AERs and target depth and transmitter frequency (the horizontal line is at a ratio of one and indicates the free-space response). When enhancement occurs (for response parameters from α_{10} to α_{400}), the AER tends to increase slightly with depth. Since the height of each bar in Figure 5-5 represents the ratio of the conductive host anomaly magnitude to the free-space host anomaly magnitude, a slight increase of this ratio with depth would imply that the free-space anomaly magnitudes were decreasing faster with depth than the corresponding conductive host anomalies. For response parameters α_1 through α_{40}, the host did not significantly affect the amplitude of the response. Table 5-2 provides the measured AERs for the moving-source system that are shown in Figure 5-5.

The increase in AER with depth may be explained physically by considering the geometry of the induced and gathered (conducted) currents in the target. Induced currents have the form of vortices while gathered currents tend to be more unidirectional. The field due to unidirectional currents tends to decay less rapidly than the field due to vortices because a vortex consists of circulating currents whose fields partially cancel one another because the currents generating the fields are not unidirectional. The AER is a ratio of the conductive host response to the free-space response. The conductive host response is due to the contribution of induced currents and conduction currents, while the free-space response can only be due to induced currents. Thus, the free-space response can be expected to decay faster with depth than the conductive host response so the AER would be expected to increase with depth.

Figure 5-6 is a reproduction of the in-phase and quadrature AERs for the horizontal coplanar coil configuration from Gaur and Verma's paper. Gaur and Verma's definition of AER is the same as given at the beginning of this section except that they calculated the AER for the in-phase and quadrature responses separately. Although in- phase and

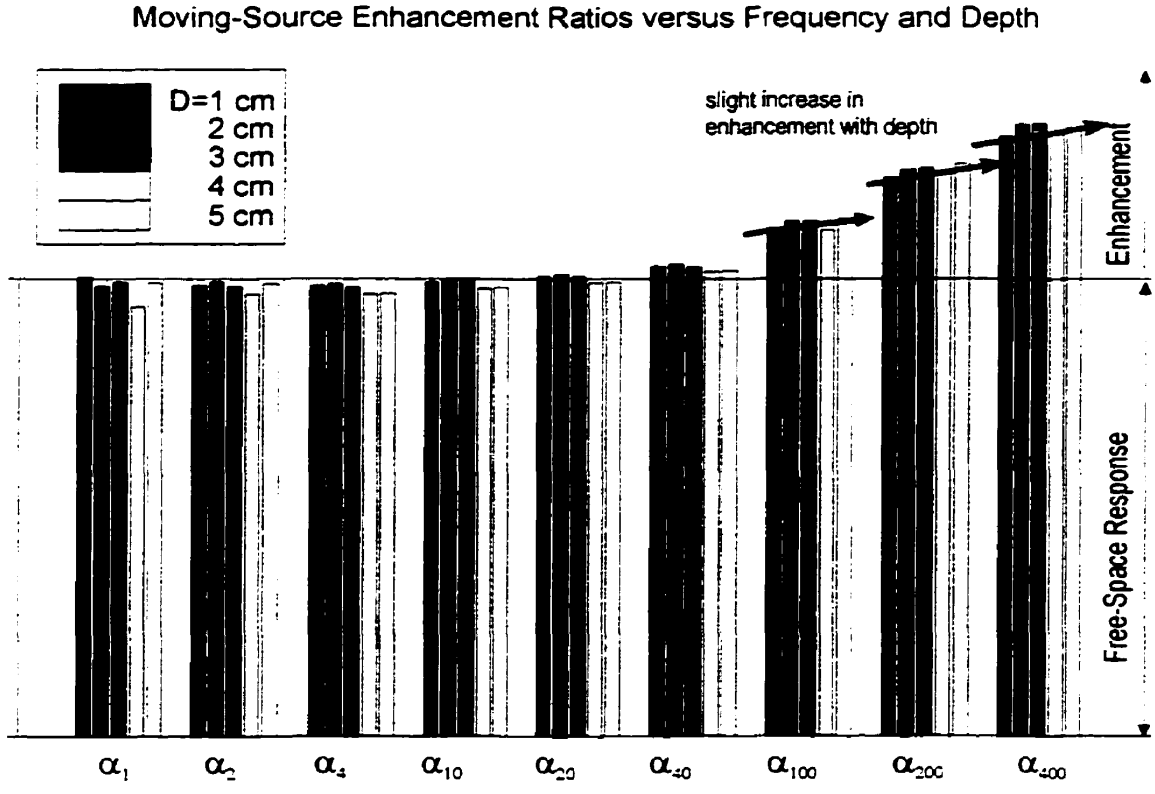

Figure 5-5: Amplitude enhancement ratios for the moving-source device. The horizontal line indicates the free-space response at AER = 1. Enhancements and attenuations are not significant for response parameters of α_1 through α_{40}. There is a slight increase in AER with depth for α_{100}, through α_{400} indicating that the free-space anomaly magnitudes decreased faster with depth than the conductive host magnitudes.

quadrature AERs from the present study are also shown on Figure 5-6, quantitative comparisons may not be made between the two sets of data because Gaur and Verma used a different normalization, and considered different host and target response parameters, and different geometries. The electromagnetic and survey parameters of Gaur and Verma's study are provided along with the same data for the present study in

Table 5-2: Measured AERs for the Moving-Source Device.

	D = 1 cm	D = 2 cm	D = 3 cm	D = 4 cm	D = 5 cm
f = 1 kHz	1.0029	0.9836	0.9933	0.9389	0.9911
f = 2 kHz	0.9857	0.9929	0.9821	0.9662	0.9880
f = 4 kHz	0.9851	0.9887	0.9813	0.9658	0.9673
f = 10 kHz	0.9934	0.9990	0.9951	0.9781	0.9802
f = 20 kHz	1.0043	1.0090	1.0044	0.9915	0.9924
f = 40 kHz	1.0259	1.0311	1.0245	1.0154	1.0182
f = 100 kHz	1.1088	1.1248	1.1243	1.1060	1.1308
f = 200 kHz	1.2203	1.2370	1.2400	1.2293	1.2495
f = 400 kHz	1.3101	1.3368	1.3386	1.3146	1.3297

the table on Figure 5-6. All the data on Figure 5-6 were collected at 100 kHz. Gaur and Verma describe the variation of the quadrature AER with depth as oscillating. The overall appearance of the data indicates an increase in quadrature AER with depth, though there are ranges of depths for which AER decreased with depth. The quadrature AERs of the present study showed either very little depth dependence for low response parameters, or a decrease in quadrature AER with depth for high response parameters. Coincidentally, the range of target depths used in the present study (indicated by the box on Figure 5-6) lie within the range of depths that show either a plateau, or a decrease in quadrature AER with depth. The character of the in-phase AER versus depth plots of the present data is similar to that of Gaur and Verma, as both tend to increase with depth when significant enhancement is present (i.e. if the in-phase AER is greater than one). Gaur and Verma did not report a second dispersion in their data. The fact that the total

AER increases with depth while the quadrature AER decreases with depth is a consequence of the vector nature of the anomaly.

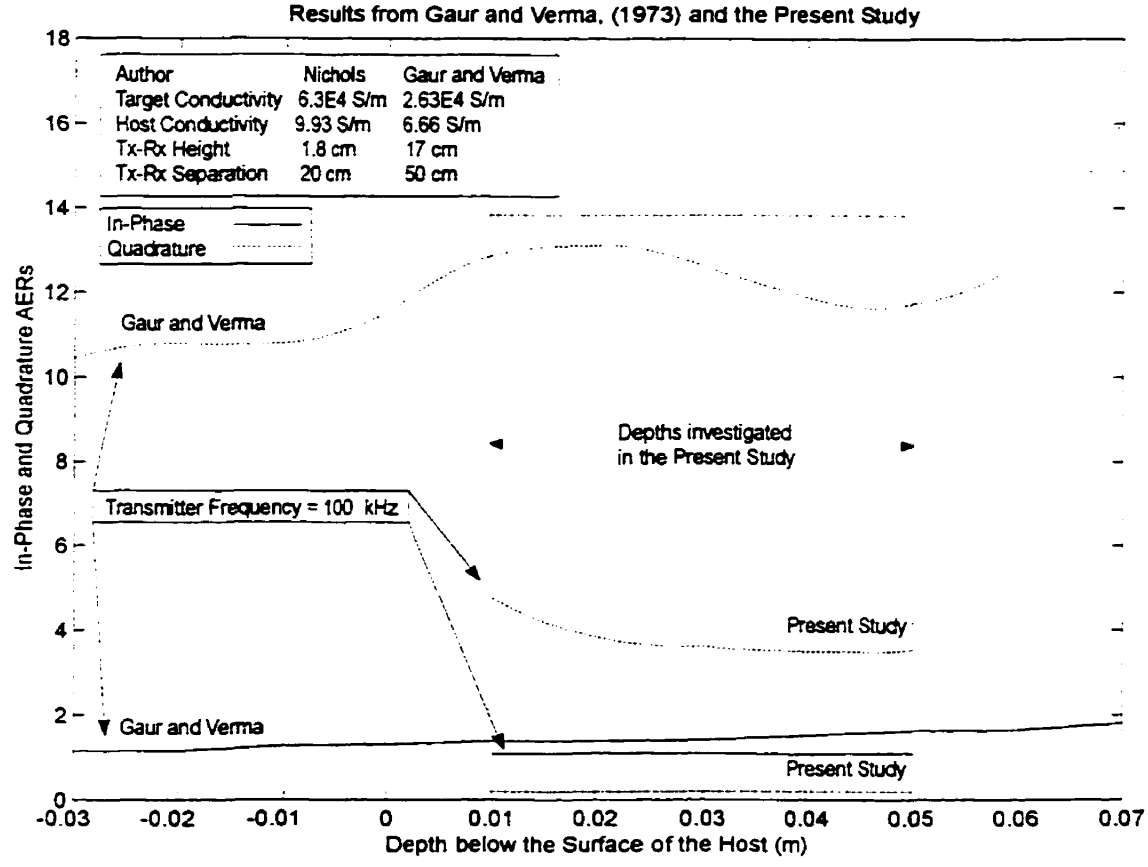

Figure 5-6: In-phase and quadrature amplitude enhancement ratios reproduced from Gaur and Verma (1973), and results from the present study for the same frequency. Experimental differences don't allow for quantitative comparison (see the table on the figure), but there is good qualitative agreement with regards to the change in the in-phase and quadrature component AERs with depth.

Hanneson and West (1984) used numerical modeling to calculate the response of a thin plate in a conducting half space. Their theoretical results did not predict a second dispersion, possibly because their program could not handle high conductivity contrasts

between the host and target. Hanneson and West's numerical solutions were found to be unstable for $\alpha_p/\alpha_h>64$, where α_p and α_h were the response parameters of the target and host respectively. The α_p/α_h ratio of the target and host used for the present study was much higher than 64, at 460.

5.3 Fixed-Source: Target in Free-Space

Fixed-source device responses are more complicated than moving-source responses because the primary field at the receiver varies along the traverse, and it must be removed from the data in order to obtain the secondary field. In full scale field surveys, the primary field cannot be measured, so it must be calculated to remove it from the measured resultant field. The method used to remove the primary field will affect the size and shape of the secondary field profile. Physical scale modeling does allow direct measurement of the primary field so that a simple vector subtraction of the primary field from the resultant field can be used to extract the secondary field in this case (see Section 4-2). Secondary field profiles obtained with the model system and processed in this way had predictable shapes (similar to those of line currents) and had good signal to noise ratios.

Aside from the variable primary field, several other factors can influence the response of the fixed-source system to a target in free-space. Bosschart (1964) grouped the factors into three categories: 1) factors that affected the geometry of the system with the frequency and electromagnetic parameters held constant; 2) factors that affected the response parameter of the target through variations in frequency, and electromagnetic parameters; and 3) factors related to the dimensions of the target, the transmitter, and to the location of the traverse with respect to the target. Category 1 factors change the shape of the anomaly, while category 2 and 3 factors alter the relative amplitudes of the complex components of the anomalies. Category 2 factors alter the amplitude relations in a way that is determined by the electromagnetic parameters alone, while category 3

factors cause amplitude variations that could mislead an interpretation because they are not related to the electromagnetic parameters of the target. Due to the large number of variables, and limited modeling materials, there was no attempt made to reproduce published results in the present study.

Lajoie and West (1976) used a numerical model to investigate the effect of a conductive host on Turam[10]-type fixed-source devices. They began by investigating the response of a plate in the field of an alternating dipole source in free-space. In their model, they varied the response parameter of the plate and found that the induced currents were initially mainly in the quadrature phase, the currents then progressed to mainly in-phase as the response parameter increased. This effect was also observed in the present study as shown by Figure 5-7 even though the transmitter is now a large square loop. The irregular behavior from α_{20} to α_{400}, and the lower amplitude of the 400 kHz data were not expected based on the indications provided by the simple induction model of Section 2.3. This unexpected behavior is likely due to the transition from thin to thick conductor behavior as discussed in Section 4.2. The values of the response parameters α_1 through α_{400} are provided in Table 5-3.

The lack of consistent thin conductor behavior means that Figure 5-7 will not be useful for general interpretations even if the transmitter and target system in question is expected to have a geometry similar to that used in the present study. The early onset of thick conductor behavior means that the free-space anomalies of Figure 5-7 are mainly

---

[10] The Turam device consists of a large transmitter, either a large rectangular loop or a grounded wire, and a pair of receivers which measure the differences in amplitude and phase of the resultant signal along a survey. The survey is usually at right angles to the near edge of the transmitter. The Turam-type device discussed here differs from the proper Turam device in that only a single receiver is used to record the fields along the survey.

controlled by the dimensions and electromagnetic parameters of the graphite target. Because of this, the anomaly index diagram presented in Figure 5-7 for the fixed-source device in free-space should not be used for interpretation of data, unless the full scale

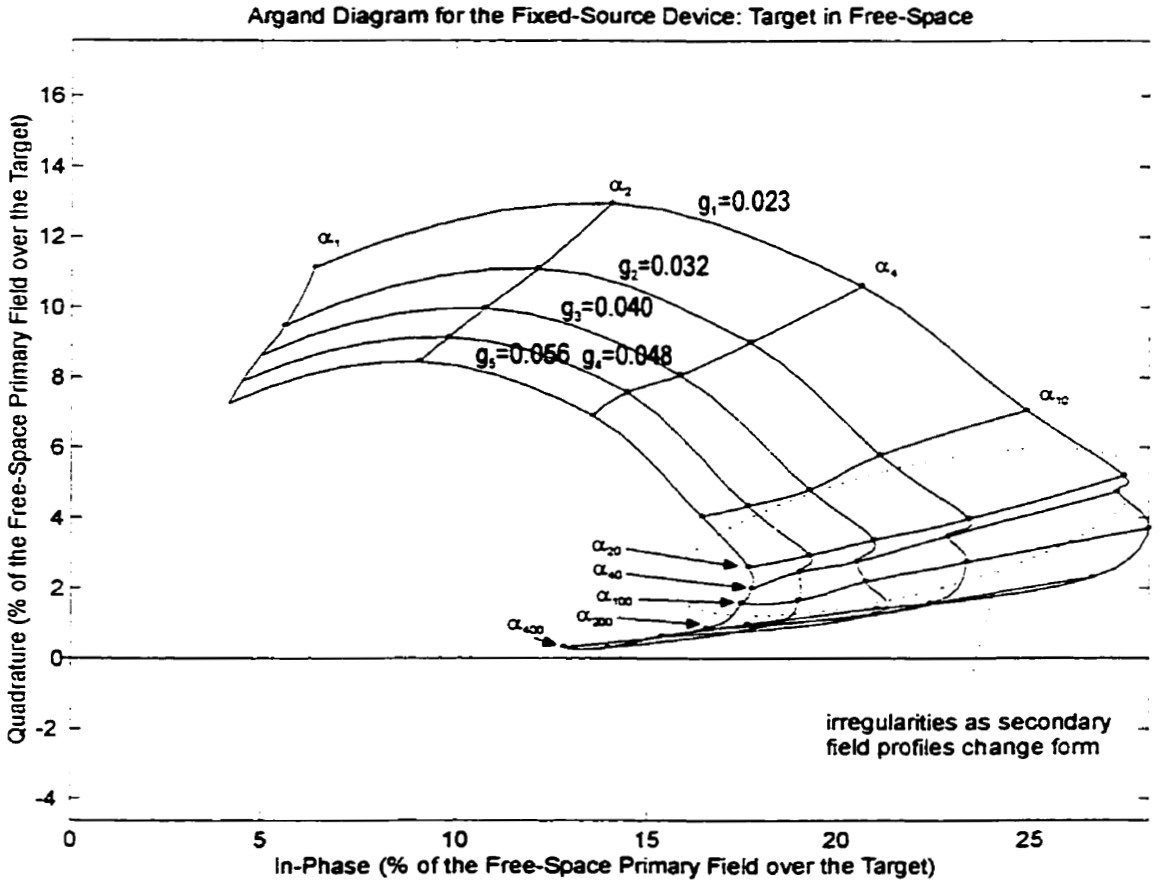

Figure 5-7: Argand diagram for the target in free-space surveyed by the fixed-source device. These responses are consistent with those of the simple induction model in that as the response parameter increased the response had a smaller quadrature component and a larger in-phase component. The irregularities that occur from α_{20} to α_{400} appear to indicate that the target has begun to respond as a thick conductor as described in Section 4-2.

target-transmitter system have the same geometry and relative dimensions as those that were used in this model study.

Table 5-3: Response parameters for the fixed-source target.

Frequency (kHz)	Response Parameter, α_f
1	7.105
2	14.21
4	28.42
10	71.05
20	142.1
40	284.2
100	7105
200	1421
400	2842

5.4 Fixed-Source: Target in a Conducting Host

Figure 5-8 shows both the free-space and conducting host anomalies of the present study on the same Argand diagram. As with the moving-source data shown in Figure 5-4, the fixed-source data showed a double dispersion. The second dispersion of the fixed-source data began at a lower frequency (4 kHz (α_4) rather than 40 kHz (α_{40})) and the enhancements were much larger than for the moving-source device (compare Figure 5-8 with Figure 5-4).

Lajoie and West (1976) used a numerical model to investigate the effect of a conducting host on a target's fixed-source response. In their investigations they kept the target response parameter constant and varied the host's response parameter through its conductivity. In the present study, the transmitter frequency was used to vary the response parameters of the system while both the target and host conductivities were

fixed, with the result that both the target and the host response parameters were affected. This difference limits comparisons with the work of Lajoie and West to the variation of the response versus depth. Their data reduction procedure, however, was identical to that used in the present study. Lajoie and West employed only a single increase in target depth in their numerical model. This showed that amplitude enhancements and phase

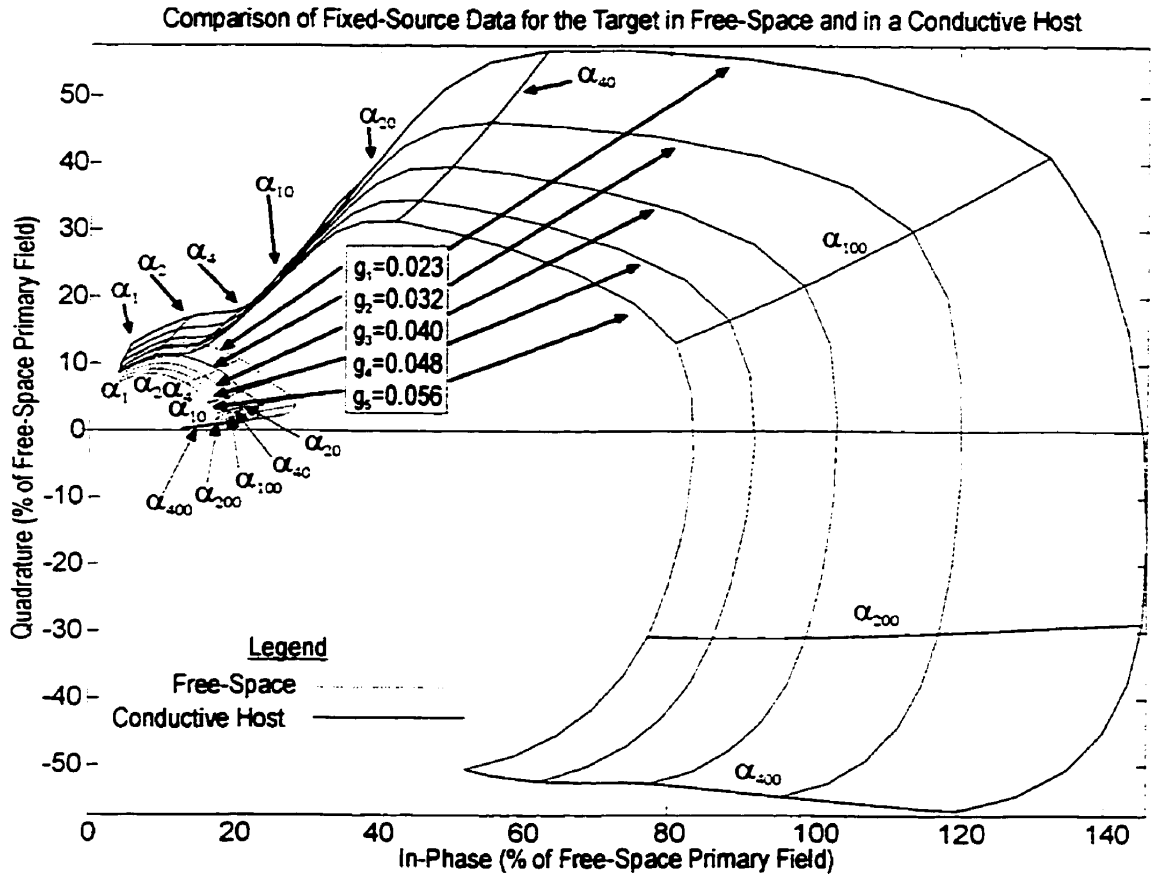

Figure 5-8: Fixed-source Argand diagrams for the target in both a free-space and conductive host. All the anomalies shown are due to the target alone. The primary and background fields due to the host have been removed. The differences shown are due to changes in the induction and conduction currents in the target due to the different hosts. The second dispersion that begins at α_4 was unexpected.

rotations increased with depth. Their conclusions to explain these results were that: 1) as depth is increased, the half space currents are greater; 2) the conduction currents are unidirectional, whereas the induction currents are vortices, so the amplitude of the conduction current decreases as the inverse of the distance from the currents rather than the inverse cube of the distance as for the vortex currents, and 3) as the distance to the surface was increased, there was more regionally induced current to gather because there was a greater volume of the host above the target from which to channel current. A direct comparison of the enhancements from Lajoie and West's paper is not possible because the target conductances and host conductivities used did not correspond to those of the present study.

The amplitude enhancements versus depth observed in this study are shown on Figure 5-9. Contrary to Lajoie and West's predictions (for which data were only presented for two models of different depth), the enhancements in Figure 5-9 tend to decrease with depth. This implies that the conductive host responses decreased faster with increased depth than the free-space responses. Table 5-4 contains the measured AERs for the fixed-source device.

The decrease in AER with depth may be explained physically by considering the geometry of the induced and gathered currents in a manner similar to that used to explain the increase in AER with depth for the moving-source device. The currents induced directly into the conductor by the fixed-source are still assumed to have the form of vortices, and the gathered currents are still assumed to be unidirectional. To argue that the fixed-source AERs should decrease with depth, the conductive host response (numerator) must decrease with depth faster than the free-space response (denominator). This can be accomplished if there is sufficient attenuation of the primary and secondary fields due to the conductive host. This implies that attenuations due to the host are not as important to moving-source device responses as they are to fixed-source devices. This seems reasonable since the fixed-source primary field must travel further through the host

than the moving-source primary field. This implies that the distance of the target from the transmitter would also affect the AER.

Lajoie and West's results were for two models where the target was buried to two different depths. The depth to strike-length ratio was 0.1 for the shallow target, and 0.3 for the deeper target. For the sake of comparison, the depth to strike-length ratios used in

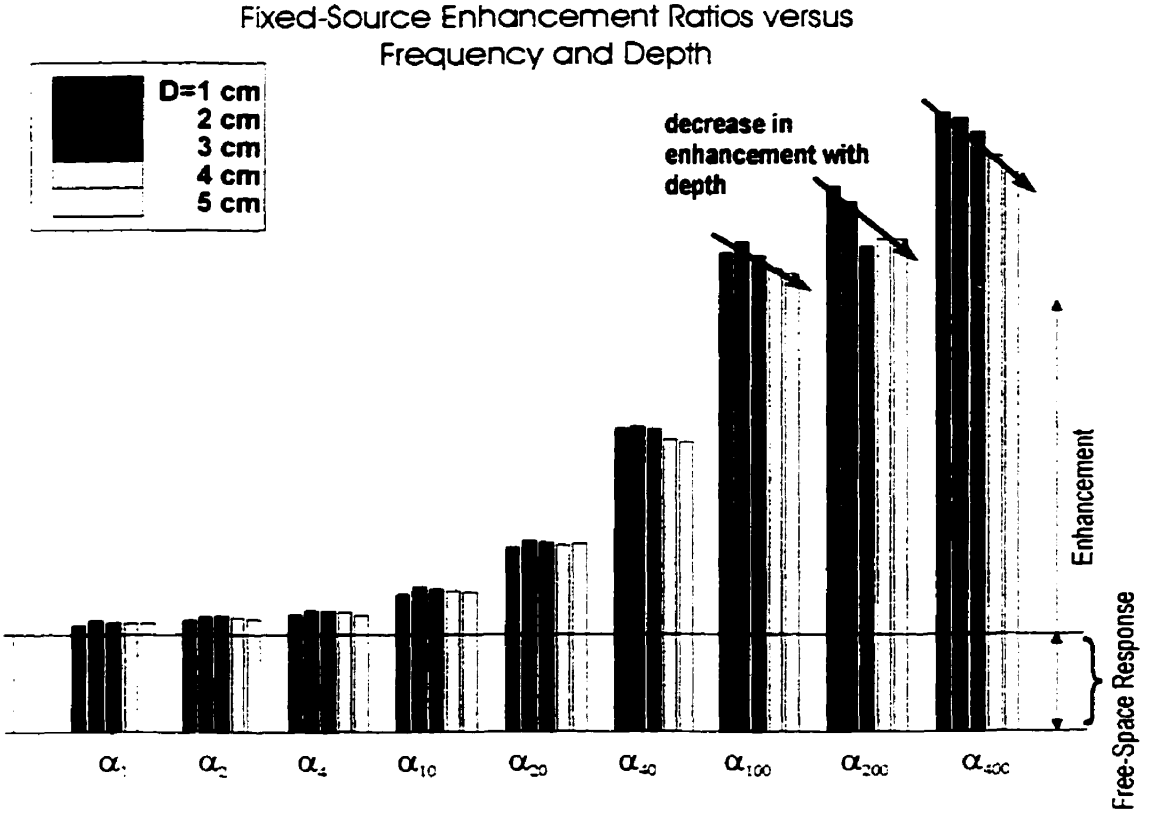

Figure 5-9: Amplitude enhancement ratios for the fixed source device. The horizontal line indicates the free-space response at AER = 1. Enhancements were apparent for all response parameters. The decrease in AER with depth that was noticeable for high response parameter data indicates that the conductive host response decreases faster with depth than the free-space response.

the present study were much smaller, in the range 0.023-0.056. Lajoie and West's transmitter was a rectangle with dimensions $1L \times 2L$, L being the strike length of the target. The transmitter was oriented so that the long edge was parallel to the strike of the target. The host conductivity was never greater than 5E-3 S/m, which means the resistivity was never less than 200 Ωm. If the model of the present study was scaled by a factor of 1:1000, and a full scale frequency of 500 Hz is assumed (after Lajoie and West)

Table 5-4: Measured AERs for the Fixed-Source Device

	D = 1 cm	D = 2 cm	D = 3 cm	D = 4 cm	D = 5 cm
f = 1 kHz	1.0926	1.1446	1.1199	1.1191	1.1184
f = 2 kHz	1.1434	1.1794	1.1890	1.1721	1.1574
f = 4 kHz	1.2045	1.2393	1.2412	1.2228	1.1963
f = 10 kHz	1.4104	1.4739	1.4619	1.4407	1.4302
f = 20 kHz	1.8772	1.9435	1.9286	1.9047	1.9182
f = 40 kHz	3.0777	3.1057	3.0769	2.9734	2.9414
f = 100 kHz	4.8709	4.9845	4.8353	4.7025	4.6534
f = 200 kHz	5.5445	5.3832	4.9309	5.0104	5.0039
f = 400 kHz	6.2868	6.2316	6.0935	5.8488	5.6793

the full-scale host conductivity would be between 2×10^{-2} S/m and 8 S/m for 1 kHz and 400 kHz respectively. Their target conductance was varied from 7 to 1000 S (compared to 913 S for the present study). The lower conductivity of the host material used in the study by Lajoie and West may have reduced attenuations to a level where they did not cause a decrease in AER with depth as was measured in the present study with the target buried in a much more conductive host.

Chapter 6

6 Comparison of the Effect of a Conductive Host on Moving- and Fixed Source Devices

The high conductivity contrast between the target and host caused the double dispersion seen on both the moving- and fixed-source anomaly index diagrams. Earlier studies by Duckworth and Krebes (1997) indicated that the magnitude and the frequency of onset of the second dispersion was independent of the target. Because the second dispersion occurred at different frequencies for the moving- and fixed-source devices, it is believed that the size and shape of the transmitter may determine the character of the host response. This is not surprising because the free-space target responses for each device were also quite different. When the target was in free-space, the moving-source device data behaved as those from a thin conductor until the frequency reached at least 100 kHz (indicated by the form of the Argand diagram). It could not be determined whether or not modeling system problems caused the deviation from thin conductor behavior (the 'curling under' of the responses on Figure 5-1) above 100 kHz. Thick conductor behavior would be expected since the skin depth for graphite was much smaller than the thickness at these frequencies, but errors in the reference measurement could also affect the size of the anomaly. The form of the fixed-source anomalies began to change from thin to thick conductor at a frequency as low as 20 kHz. Studies with different shaped transmitters of equal cross sectional area, or similarly shaped targets of different size may clarify whether the size or the shape of the transmitter is more important.

Published results indicate that both devices should have AERs that increase with depth (Gaur and Verma, 1973; Lajoie and West, 1976). The results of the present study are in agreement with this for the moving-source device, but not for the fixed-source device. By considering the numerator and denominator of the AER it was found that the decrease in AER with depth for the fixed-source device could be explained if attenuations due to

the conductive host were more important for the fixed-source device than for the moving-source device. This seemed reasonable because the fixed-source primary field has to travel farther through the host than the moving-source primary field does. Lajoie and West's results were obtained by numerical modeling of a target in a host that had a conductivity of 5×10^{-3} S/m. The conductivity of the brine solution in the present study was 9.93 S/m. When this is converted to the full scale value using a linear scale factor or 1:1000 and a full scale frequency of 500 Hz (as Lajoie and West), the range of full scale host conductivities that this corresponds to is 2×10^{-2} S/m to 8 S/m for model frequencies 1 and 400 kHz respectively. It is believed that the higher conductivity host caused greater attenuation of the measured fields, which in turn, caused the fixed-source AERs to decrease, rather than increase, with depth. This implies that the behavior of the AERs may also depend on the distance of the target from the source for the fixed-source device.

The large enhancement of the fixed-source data was due to the fact that the fixed-source transmitter was so much larger than the moving-source transmitter. The larger transmitter was capable of inducing currents in a larger volume of the host. Since the enhancement of the target response is related to the amount of conduction current that passes through the target, a larger volume of current carrying host surrounding the target will cause the enhancement to be stronger. It would be interesting to develop a numerical method that could handle conductivity contrasts similar to those of the present study to see if second dispersions develop.

Chapter 7

7 Conductive Sphere in a Dipole Field

An attempt was made to model the response of a conductive sphere in free-space to a vertical-coaxial coil (horizontal dipole) moving-source configuration. The goal was to reproduce the results of Lodha and West (1976). Lodha and West used the theory that was developed by Wait (1953) as it was presented in Grant and West (1965) to calculate the profile that would have been observed on a traverse that passed directly over the centre of the sphere. Best and Shammas (1979) had reproduced Lodha and West's results and extended them to include the response for traverses that did not pass directly over the centre of the sphere. The goal of the present work was to write a program that could model the free-space sphere and then extend that program to model the sphere under a conductive overburden. This chapter describes the unsuccessful attempt of the author to reproduce the published results of Lodha and West, and Best and Shammas.

7.1 Theory

In spherical coordinates, an arbitrary dipole moment vector may be expressed as the sum of three orthogonal component vectors, one radial and two transverse. The following expressions (Grant and West, 1965) describe the secondary fields emitted by the sphere due to the presence of any of the component dipoles.

Secondary Field Components Due to a *Radial Dipole*

$$H_r^{(S)} = -\frac{m_r}{4\pi} e^{i\omega t} \sum_{n=1}^{\infty} (X_n + iY_n) \frac{a^{2n+1}}{(rr_o)^{n+2}} n(n+1) P_n(\cos\vartheta) \qquad \textit{Equation 7-1}$$

$$H_{\vartheta}^{(S)} = -\frac{m_r}{4\pi} e^{i\omega t} \sum_{n=1}^{\infty} (X_n + iY_n) \frac{a^{2n+1}}{(rr_o)^{n+2}} n P_n^1(\cos\vartheta)$$

$$H_{\varphi}^{(S)} = 0$$

Secondary Field Components Due to a *Transverse Dipole in the same axial plane as the receiver* ($\varphi - \varphi_o = 0$).

$$H_r^{(S)} = \frac{m_{\vartheta}}{4\pi} e^{i\omega t} \sum_{n=1}^{\infty} (X_n + iY_n) \frac{a^{2n+1}}{(rr_o)^{n+2}} n P_n^1(\cos\vartheta) \qquad \textit{Equation 7-2}$$

$$H_{\vartheta}^{(S)} = -\frac{m_{\vartheta}}{4\pi} e^{i\omega t} \sum_{n=1}^{\infty} (X_n + iY_n) \frac{a^{2n+1}}{(rr_o)^{n+2}} \left[n^2 P_n(\cos\vartheta) - \frac{n}{n+1} \cot\vartheta P_n^1(\cos\vartheta) \right]$$

$$H_{\varphi}^{(S)} = 0$$

Secondary Field Components Due to a *Transverse Dipole Perpendicular to the axial plane of the receiver* ($\varphi - \varphi_o = \pi/2$).

$$H_r^{(S)} = H_{\vartheta}^{(S)} = 0 \qquad \textit{Equation 7-3}$$

$$H_{\varphi}^{(S)} = -\frac{m_{\varphi}}{4\pi} e^{i\omega t} \sum_{n=1}^{\infty} (X_n + iY_n) \frac{a^{2n+1}}{(rr_o)^{n+2}} \left[\frac{n}{n+1} \csc\vartheta P_n^1(\cos\vartheta) \right]$$

The function (X_n+iY_n) is called the response function and is given by

$$\{X_n + iY_n\} = \left\{ \frac{\left[\frac{\mu_o}{2} - (n+1)\mu\right] I_{n-1/2}(ka) + \mu_o ka I'_{n-1/2}(ka)}{\left(\frac{\mu_o}{2} + n\mu\right) I_{n-1/2}(ka) + \mu_o ka I'_{n-1/2}(ka)} \right\} \qquad \textit{Equation 7-4}$$

The symbols are defined in Table 7-1.

The field for an arbitrarily oriented dipole may be calculated by decomposing the arbitrary dipole into its three spherical components, calculating the secondary fields due to each of the component dipoles, and summing the corresponding fields. The field that would be measured by a vertical coaxial receiver is then determined by the sum of the parts of the component fields that pass perpendicularly through the receiver coil.

7.2 Modeling a Vertical Coaxial EM System

A vertical coil transmitter produces a horizontal dipole moment that can be decomposed vectorally into three components in the spherical coordinate system, one radial component, and two transverse components. In the case of geophysical surveys that pass over the centre of the sphere, the horizontal dipole moment vector has only a radial component and a transverse component in the plane of the survey line and centre of the sphere.

The secondary fields generated by the radial and transverse components of the transmitting dipole moment, measured at r, are given by Equations 7-1 and 7-2 respectively, where m_r, and m_ϑ are the radial and transverse components of the total dipole moment m. For the purposes of the program, the m has been set to one, because it will be eliminated during normalization.

For the receiving coil, a vector sum of the secondary fields generated by the two component dipoles m_r, and m_ϑ, is the total secondary field at the receiver location. Because a planar coil will only respond to fields that pass through the plane of the coil at

Table 7-1: List of symbols used in this chapter.

Symbol	Definition
a	Radius of spherical conductor centred on the origin
B_n	Variables for unknown functions
D	Depth to centre of sphere
d	Distance from the point directly over the centre of the sphere to the point midway between the transmitter and the receiver measured on the surface of the earth
E_n	Variables for unknown functions
f	Transmitter field frequency
$I_{n+1/2}(x)$	Modified Bessel function of the first kind evaluated at x
$I'_{n+1/2}(x)$	First derivative of the modified Bessel function of the first kind evaluated at x
k^2	$i\sigma\mu\omega$
m_r	Radial component of magnetic dipole
m_ϑ	Theta component of magnetic dipole
p	Strength of the magnetic pole
$P_n(\cos\vartheta)$	Legendre polynomial of order n
$P_n^1(\cos\vartheta)$	Legendre polynomial of first degree and order n
r	Distance from origin to receiver
r_o	Radial distance from the origin to the transmitter
δ	Angle between the vector r and the horizontal
φ	Angle measured from the x-axis in the x-y plane
μ	Magnetic permeability of the sphere
μ_o	Magnetic permeability of free-space
ϑ	Angle measured from the z-axis
ω	Frequency of the oscillating field

an oblique angle, each component of the secondary field must be reduced to the sum of two orthogonal vectors, one in the plane of the receiving coil, and one perpendicular to it. The vector sum of the perpendicular fields will be the signal measured by the receiver. The modeling code was written as MATLAB script files.

7.2.1 The Vertical Coaxial Modeling Code

The vertical coaxial coil modeling routine (VERTICALCOAXIAL) plots, and returns the numerical values for the profiles that would be obtained from a vertical coaxial coil survey that passes over the centre of a conducting sphere. The program requires seven input parameters: the coil separation (S>0, meters), the radius of the sphere (a>0, meters), the sphere conductivity (σ>0, Siemens/meter), the depth to the sphere (D>a, meters), a vector of sampling points (d, meters), an operating frequency (f, Hertz), and the order of the highest magnetic multipole to be considered (this is usually set to 20, though it was found that 10 would often prove adequate). The vector of sampling points is entered with reference to the point directly over the centre of the sphere, with negative distances to the left and positive distances to the right. The survey is conducted along a line passing directly above the centre of the sphere, though it is not necessary for the points to be regularly spaced, or that the survey must extend to the point directly over the sphere. The resulting profiles are normalized to the primary field measured at the receiver.

Unless otherwise indicated, the author wrote all MATLAB functions.

7.2.2 Structure of the Modeling Code

VERTICALCOAXIAL takes the aforementioned input parameters are returns the vectors r, r_o, ϑ, α, δ, m_r, and m_ϑ. Each element of the vectors corresponds to a different sampling point; for example, if d=[-3 0 3], then the corresponding transmitter distances would be given by r=[$r(d=-3)$ $r(d=0)$ $r(d=3)$].

Once the survey geometry is calculated, the program calls the function FIELDS that calculates the secondary fields due to each of the components of the dipole. The ith term of the series for each of the sampling points is calculated simultaneously and stored in the ith row of a matrix. Once there are as many terms as requested (i.e. n terms, where the highest order multipole is n), the sum of each column is calculated. Since the columns

represent a constant d value, this amounts to calculating the summations in Equations 7-1 and 7-2. Finally, the summations are multiplied by the appropriate coefficients to get the component fields.

Each term in the summation requires the value of the response function for a given multipole order. These complex numbers are calculated by a function called RFGENERATOR, which stands for Response Function Generator. RFGENERATOR takes the survey frequency, multipole order, sphere radius, conductivity, and magnetic permeability as input, and returns the appropriate response function value. The response function is calculated from Equation 7-4, which requires modified Bessel functions of the first kind and their first derivatives. MATLAB has a Bessel function generator, as well as a few differentiation routines, but these did not work well for the magnitudes of the parameters required. The RFBESSEL function was written to calculate both of the required Bessel Functions. The Bessel function is calculated from the standard series solution

$$I_n(x) = \sum_{k=0}^{\infty} \frac{\left(x/2\right)^{n+2k}}{k!\Gamma(k+1+n)}$$

The first derivative of the Bessel function above was calculated from the above expression to be

$$I_n'(x) = \sum_{k=0}^{\infty} \frac{(n+2k)\left(x/2\right)^{n+2k-1}}{2k!\Gamma(k+1+n)}$$

This solution is acceptable for response parameters less than 1000.

Also necessary for the field calculations are the Legendre polynomials, $P_n(\cos\vartheta)$, and $P_n^1(\cos\vartheta)$. MATLAB has a built in LEGENDRE function that originally had a bug in it that would not allow it to work for Legendre polynomials of degree 4 (for this program

Legendre functions of every degree from 1 to 20 were necessary). This error was corrected in a later version of MATLAB.

Once FIELDS returns the field values to VERTICALCOAXIAL, horizontal components of the total radial and total transverse fields are calculated, and the fields are normalized with respect to the primary field measured at the receiving coil,

$$H^P = -\frac{m}{2\pi s^3}$$

where m=1.

VERTICALCOAXIAL then calls a plotting routine, VCPROFILE that plots the normalized response profile.

7.2.3 Testing the Modeling Software

The profiles generated by the VERTICALCOAXIAL program were symmetric, and demonstrated scale invariance as expected. Comparisons to published results proved unsatisfactory.

The solid lines on Figure 7-1a to 7-1f are the results from VERTICALCOAXIAL. The stars indicate the corresponding points from the published results from Lodha and West's Figures 4a, 4b, 4c, 5a, 5b and 5c (corresponding to Figures 7-1a to 7-1f). The VERTICALCOAXIAL output only agreed with Figure 7-1a. It was noted that the agreement would be better in Figures 7-1d to 7-1f if the VERTICALCOAXIAL results were decreased by a factor of π. Since these fields had been normalized by dividing by the primary field, $\frac{1}{2\pi s^3}$, it was thought that normalization by a factor of $\frac{1}{2s^3}$ would provide a better fit for Figures 7-1d to 7-1f, though this would ruin the agreement seen in

Figure 7-1a. The effect of the $\frac{1}{2S^3}$ normalization is shown in Figure 7-2. The agreement for Figures 7-2d to 7-2f is good, though it seems that the profiles are slightly

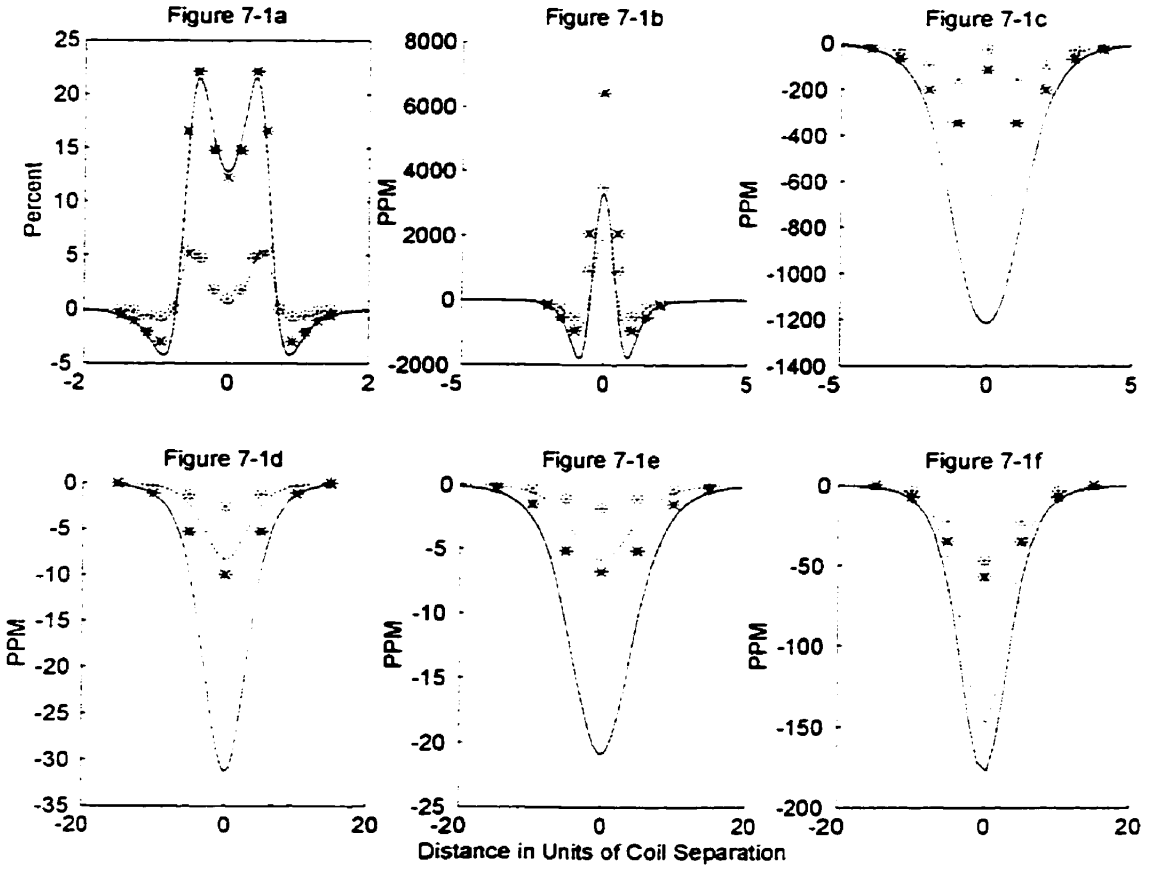

Figure 7-1: VerticalCoaxial data are shown with lines, published results from Lodha and West (1976) are shown as stars. Solid lines and stars are in-phase responses and dashed lines and stars are quadrature phase responses. The normalization factor used was $\frac{1}{2\pi S^3}$. *Figure 7-1a shows good agreement, while Figures 7-1d to 7-1f appear to be too large by a factor of* π. *See Table 7-2 for the geometry and response parameters of each figure.*

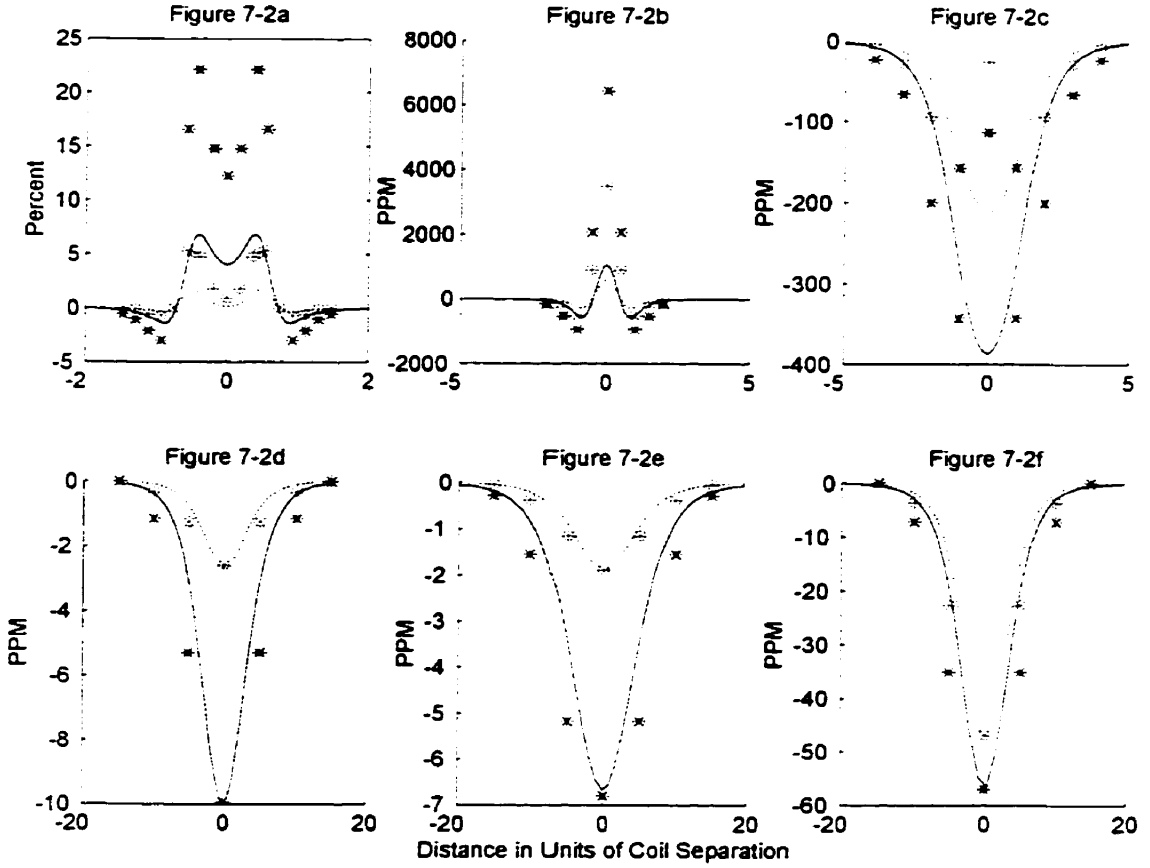

Figure 7-2: VerticalCoaxial data are shown with lines, published results from Lodha and West (1976) are shown as stars. Solid lines and stars are in-phase responses and dashed lines and stars are quadrature phase responses. The normalization factor used was $\frac{1}{2S^3}$. *Figures 7-2d to 7-2f are in good agreement with the published results, though the VerticalCoaxial anomaly appears to be too thin. As expected, Figure 7-1a is no longer in agreement with the published results. See Table 7-2 for the geometry and response parameters of each figure.*

thinner than the published results. Agreement between VERTICALCOAXIAL results and the published data was never very good for Figure 7-1b or 7-1c, or 7-2b or 7-2c.

Table 7-2: Geometry relations and response parameters for the sub-figures in Figures 7-1, 7-2, and 7-3.

Sub-Figure of Figures 7-1, to 7-3	Depth to Separation D/S	Depth to Radius D/a	Response Parameter	Radius to Separation a/S
a	0.5	1.2	100	0.4
b	0.9	3.0	30	0.3
c	2.1	3.0	30	0.7
d	7	4	100	1.75
e	10	3.3	100	3
f	8	2.0	25	4

At this point it appeared that no single version of the program could reproduce all six figures, even though the publications indicated that the same program generated them all. Further attempts to debug the program lead to an investigation of the Legendre function. Two definitions of the Legendre function were found. The first, from the Schaums Mathematical Handbook (Speigel, 1993)

$$P_n^m(x) = (1-x^2)^{m/2} \frac{d^m}{dx^m} P_n(x)$$

the second, from MATLAB's Legendre function code

$$P_n^m(x) = (-1)^m (1-x^2)^{m/2} \frac{d^m}{dx^m} P_n(x)$$

The difference was a factor of -1 for the first order Legendre polynomial. When the first order Legendre function was 'corrected' by multiplication by -1, the result was a much better match for the last three figures (Figures 7-3d, 7-3e, and 7-3f), but there were large discrepancies for the first three figures (Figures 7-3a, 7-3b, and 7-3c).

The author was unable to determine the cause of the discrepancies between the published results and the output from the VERTICALCOAXIAL programs. The MATLAB programs have been included in Appendix C.

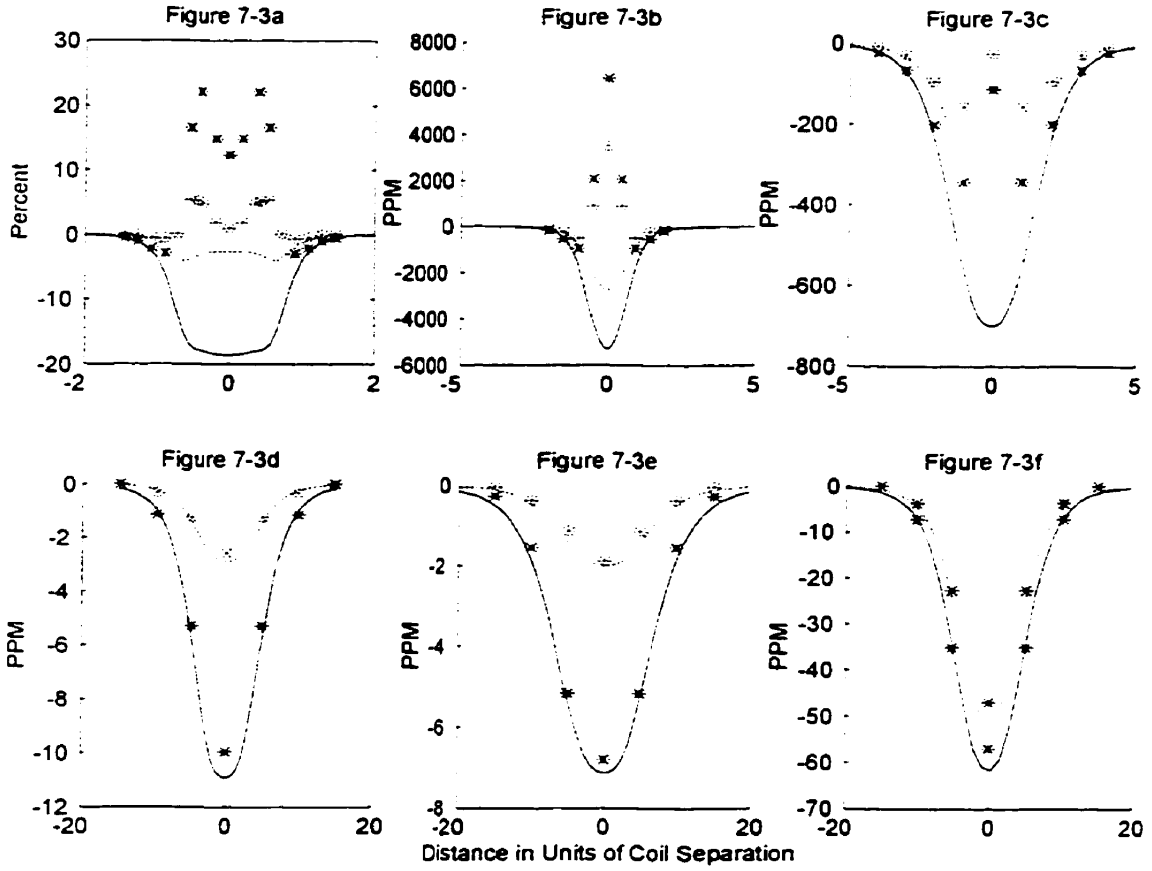

Figure 7-3: VerticalCoaxial data are shown with lines, published results from Lodha and West (1976) are shown as stars. Solid lines and stars are in-phase responses and dashed lines and stars are quadrature phase responses. The normalization factor used was $\frac{1}{2\pi S^3}$, *and the MATLAB Legendre function has been 'corrected' by multiplication of the first order Legendre polynomials by -1. The Legendre function correction has improved the agreement between the published results and the VerticalCoaxial output for Figures 7-3d to 7-3f, but lessened the agreement of Figures 7-3a to 7-3c. See Table 7-2 for the geometry and response parameters of each figure.*

References

Bays, A. R., 1982, Development of an electromagnetic modeling apparatus: M.Sc. thesis, University of Calgary.

Best, M. E., and Shammas, B. R., 1979, A general solution for a spherical conductor in a magnetic dipole field: Geophysics, **44**, 781-800.

Bosschart, R. A., 1964, Analytical interpretation of fixed-source electromagnetic prospecting data: Ph.D. thesis, University of Delft, Holland.

Cummins, C., 1986, Scale modelling of the parallel-line mode of operation of the Turam prospecting system and a comparison with the conventional mode: M.Sc. thesis, University of Calgary.

Duckworth, K., 1972, Turam interpretation by curve matching using a line current approximation: Geophysical Prospecting, **20**, 514-528.

Duckworth, K., 1988, A modified current-filament model for use in the interpretation of frequency-domain electromagnetic data: Canadian Journal of Exploration Geophysics, **24**, 66-71.

Duckworth, K., and Krebes, E. S., 1997, The response of steeply dipping tabular conductors located in conductive host rocks when detected by horizontal coplanar coil and vertical coincident coil electromagnetic exploration systems: Canadian Journal of Exploration Geophysics, **33**, 55-65.

Duckworth, K., and O'Neill, D., 1989, Turam responses in a scale model conductive environment for single and paired conductors: Canadian Journal of Exploration Geophysics, **25**, 115-137.

Duckworth, K., and O'Neill, D., 1992, Comparison of scale-model results with field surveys conducted over the night hawk test range using fixed-loop and moving-source electromagnetic systems: Canadian Journal of Exploration Geophysics, **28**, 1-5.

Frischknecht, F. C., 1988, Electromagnetic physical scale modeling: *in* M. N. Nabighian, Ed., Electromagnetic methods in applied geophysics: SEG, **1**, 365-372.

Gaur, V. K., and Verma, O. P., 1973, Enhancement of electromagnetic anomalies by a conducting overburden II: Geophysical Prospecting, **21**, 159-184.

Gaur, V. K., Verma, O. P. and Gupta, C. P., 1972, Enhancement of electromagnetic anomalies by a conducting overburden: Geophysical Prospecting, **20**, 580-604.

Grant, F. S., and West, G. F., 1965, Interpretation theory in applied geophysics: McGraw-Hill Book Co.

Guptasarma, D., and Maru, V. M., 1971, A study of some effects of a conducting host rock with a new modeling apparatus: Geophysics, **36**, 166-183.

Hanneson, J. E., and West, G. F., 1984, The horizontal loop electromagnetic response of a thin plate in a conductive earth: part II - computational results and examples: Geophysics, **49**, 421-432.

Hedström, E. H., and Parasnis, D. S., 1958, Some model experiments relating to electromagnetic prospecting with special reference to airborne work: Geophysical Prospecting, **6**, 322-341.

Keller, G. V., 1988, Rock and Mineral Properties: *in* M. N. Nabighian, Ed., Electromagnetic methods in applied geophysics: SEG, **1**, 13-18.

Lajoie, J. J., and West, G. F., 1976, The electromagnetic response of a conductive inhomogeneity in a layered earth: Geophysics, **41**, 1133-1156.

Lodha, G. S., and West, G. F., 1976, Practical airborne EM (AEM) interpretation using a sphere model: Geophysics, **41**, 1157-1169.

Lorrain, P., Corson, D. R., and Lorrain, F., 1988, Electromagnetic fields and waves, Third edition: W. H. Freeman and Company.

Lowrie, W., and West, G. F., 1965, The effect of a conducting overburden on electromagnetic prospecting measurements: Geophysics, **30**, 624-632.

Macnae, J. C., and Walker, P., 1981, The Thomas township test target: an example of EM interpretation using simple models: Res. in Appl. Geophys., No. 22, Geophys. Lab., Dept. of Physics, Univ. of Toronto.

Nair, M. R., Biswas, S. K., and Mazumdar, K., 1968, Experimental studies on the electromagnetic response of tilted conducting half-planes to a horizontal-loop prospecting system: Geoexploration, **6**, 207-244.

O'Neill, D. A., 1989, Turam responses in a conductive environment: M.Sc. thesis, University of Calgary.

Pitcher, D. H., 1985, Night Hawk geophysical test range results, District of Cochrane, *in* Wood, J., White, O. L., Barlow, R. B., and Colvine, A. C., Eds., Summary of field work: Ont. Geol. Surv., Misc. Paper 126, 170-177.

Sinclair, G., 1948, Theory of models of electromagnetic systems: Proc. I. R. E., **36**, 1364-1370.

Speigel, M. R., 1993, Schaums Outline Series: Mathematical Handbook of Formulas and Tables: McGraw Hill Inc., Toronto.

Spies, B. R., 1976, The derivation of absolute units in electromagnetic scale modeling: Geophysics, **41**, 1042-1047.

Verma, O.P., and Gaur, V.K., 1975, Transformation of electromagnetic anomalies brought about by a conducting host rock: Geophysics, **40**, 473-489.

Wait, J. R., 1953, A conducting permeable sphere in the presence of a coil carrying an oscillating current: Canadian Journal of Physics, **31**, 670-678.

Ward, S. H., 1967, The electromagnetic method, *in* Hansen, D. A., Ed., Mining Geophysics, SEG, **2**, 224-372.

Appendix A

Using Equations 2-5 to 2-7, the definition of the curl of a vector in rectangular coordinates, and the chain rule it will be shown that $\nabla_2 \times \mathbf{V} = p\nabla_1 \times \mathbf{V}$.

The curl of a vector in the rectangular coordinates of the second system, denoted by a subscript 2 is

$$\nabla_2 \times \mathbf{V} = \left(\frac{\partial \mathbf{V}_{z2}}{\partial y_2} - \frac{\partial \mathbf{V}_{y2}}{\partial z_2} \right) \bar{x}_2 + \left(\frac{\partial \mathbf{V}_{x2}}{\partial z_2} - \frac{\partial \mathbf{V}_{z2}}{\partial x_2} \right) \bar{y}_2 + \left(\frac{\partial \mathbf{V}_{y2}}{\partial x_2} - \frac{\partial \mathbf{V}_{x2}}{\partial y_2} \right) \bar{z}_2 .$$

Equations 2-5 to 2-7 provide the following differential relationships

$$p = \frac{\partial x_1}{\partial x_2} = \frac{\partial y_1}{\partial y_2} = \frac{\partial z_1}{\partial z_2} .$$

The chain rule applied to the first term on the right hand side of the curl equation becomes

$$\left(\frac{\partial V_{z2}}{\partial y_1} \frac{\partial y_1}{\partial y_2} - \frac{\partial V_{y2}}{\partial z_1} \frac{\partial z_1}{\partial z_2} \right) \bar{x}_2 = \left(\frac{\partial V_{z2}}{\partial y_1} p - \frac{\partial V_{y2}}{\partial z_1} p \right) \bar{x}_1 ,$$

and it is noted that the unit vectors, by definition, are interchangeable.

Applying the chain rule to the remaining terms of the curl equation, and factoring out the scale factor p shows that

$\nabla_2 \times \mathbf{V} = p\nabla_1 \times \mathbf{V}$, as required.

The next identity to be derived is $\frac{\partial V}{\partial t_2} = q\frac{\partial V}{\partial t_1}$. This requires differentiating Equation 2-8 and applying the chain rule to $\frac{\partial V}{\partial t_2}$.

Equation 2-8 provides the relationship $q = \frac{\partial t_1}{\partial t_2}$, so by the chain rule,

$\frac{\partial V}{\partial t_2} = \frac{\partial V}{\partial t_1}\frac{\partial t_1}{\partial t_2} = q\frac{\partial V}{\partial t_1}$ as required.

Appendix B

When an object is scaled, its relative dimensions (e.g. width to height ratio) remain the same. Since the skin depth is also a length, then it follows that the ratio of a linear dimension to the skin depth must also be constant upon scaling. Mathematically this is expressed as

$$\frac{L_{1,k}}{\delta_{1,k}} = \frac{L_{2,k}}{\delta_{2,k}}$$

where the subscript 1 or 2 denote the two systems, and the subscript k refers to the kth object in either system.

Recall that the skin depth of a material with conductivity σ, magnetic permeability μ, in the presence of an electromagnetic field oscillating with an angular frequency ω (and ω is low enough that displacement currents are negligible) is given by

$$\delta = \sqrt{\frac{2}{\sigma\mu\omega}}$$

so that the first equation becomes

$$L_{1,k}\sqrt{\frac{\sigma_{1,k}\mu_{1,k}\omega_{1,k}}{2}} = L_{2,k}\sqrt{\frac{\sigma_{2,k}\mu_{2,k}\omega_{2,k}}{2}}$$

which simplifies to

$$L_{1,k}^{\ 2}\sigma_{1,k}\mu_{1,k}\omega_{1,k} = L_{2,k}^{\ 2}\sigma_{2,k}\mu_{2,k}\omega_{2,k}$$

The last equation is identical to Equation 2-28, the scaling relationship.

Appendix C

Vertical Coaxial

```
% VerticalCoaxial.m          Written by Tricia Nichols 28/03/97.
%
% [HR,HI]=VerticalCoaxial(S,d,D,a,cond,mu,f,nmax);
%
% This program returns the total real and total imaginary secondary
% magnetic fields measured by a vertical loop receiver.
%
% This program requires the operator to define a linear survey that passes
% over the centre of the sphere.  The input parameters are:
%
% S = coil separation in meters (can be very small, but not zero).
% d = points to be sampled along a line that passes over the centre of the
%    sphere.  d=0 corresponds to the point directly above the sphere.
%    The spacing of the points need not be regular.
% D = the vertical depth to the centre of the sphere in meters.
% a = the radius of the sphere in meters.
% cond = the conductivity of the sphere in (ohms*m)^-1.
% mu = the magnetic permeability of the sphere in H/m.
% f = the frequency of the survey in Hz.
% nmax = the highest excited multipole to be considered.
%*** The following is to be added in the future, as of April/97 only[11]
%    dipole moments in the horizontal orientation are considered.***
% MDD = magnetic dipole direction cosine, three component vector of the form
%       MDD=[Cos(theta-x), Cos(Theta-y), Cos(Theta-z)], (z +ve upwards)
%     Examples: Vertical Dipole => MDD=[0 0 1]
%               Horizontal Dipole Parallel to survey => MDD=[0 1 0]
%               Horizontal Dipole Perpendicular to survey => MDD=[1 0 0]

function [HR,HI] = VerticalCoaxial(S,d,D,a,cond,mu,f,nmax)
% Geometry and survey information
r=sqrt(D^2+(d+S/2).^2);              %position of receiver (m)
rnot=sqrt(D^2+(d-S/2).^2);   %position of inducing dipole (m)
```

---

[11] This was never done.

```
angro=acos(D./rnot);
angr=acos(D./r);
theta=abs(angro-angr);          % angle between r and rnot
alpha=pi-asin(D./rnot);         % angle between rnot and the horizontal

for k = 1 : length(d)
   if abs(d(k)) <= S/2
        theta(k)=angro(k)+angr(k);%angle between r and rnot (radians)
   end
   if d(k) <= S/2
        alpha(k) = asin(D/rnot(k));
   end
end

Mr=cos(alpha);                  % radial component of the transmitting dipole
Mt=sin(alpha);                  % transverse component of the transmitting dipole
%Mr=sin(alpha);Mt=cos(alpha);note='Trish Aug 6 /98'

Mp=1;                   % second transverse component of transmitting dipole

x=cos(theta);                   % parameter for the LEGENDRE function
delta=alpha+theta;

% Calculate the components of the secondary fields generated by the component
% dipoles.

[Rr,Rt,Rp,T1r,T1t,T1p,T2r,T2t,T2p] =
Fields(Mr,Mt,Mp,nmax,x,theta,a,cond,mu,f,r,rnot);

% Calculate the total field measured by a vertical receiver
HRtot=(real(Rr+T1r)).*cos(delta)+(real(Rt+T1t)).*sin(delta);
HItot=(imag(Rr+T1r)).*cos(delta)+(imag(Rt+T1t)).*sin(delta);

% Normalize to primary field at a distance S from the receiver
Hprime=-1/(2*pi*S^3);[12]
HR=100*HRtot./Hprime;
HI=100*HItot./Hprime;
```

---

[12] Figure 7-2 was produced by removing the factor π from *Hprime*.

```
% plot the results
VCProfile

%THERE IS A PROBLEM WITH T1t BECAUSE IT'S NAN-this occured because theta
went
%to zero when S=0, and cotan in the Field code went to infinity- so S can
%be very small, but NOT zero!  March 28/97
```

Fields

```
%function [Rr,Rt,Rp,T1r,T1t,T1p,T2r,T2t,T2p] =
Fields(mr,mt1,mt2,nmax,x,theta,a,cond,mu,f,r,rnot)
%
% This function calculates the radial and theta components of the secondary
% fields produced by radial and theta magnetic dipoles.
%
% Rr, Rt, Rp = the radial, theta, and psi fields due to a radial dipole
% T1r, T1t, T1p = the radial, theta and psi fields due to a theta dipole
%
% Written by Tricia Nichols   28 March 1997
%

function [Rr,Rt,Rp,T1r,T1t,T1p,T2r,T2t,T2p] =
Fields(mr,mt1,mt2,nmax,x,theta,a,cond,mu,f,r,rnot)

RCoeff=-mr/(4*pi);
TtCoeff=mt1/(4*pi);
TpCoeff=-mt2/(4*pi);
for n = 1:nmax
        clear pn;
        pn=legendre(n,x);
%pn(1,:)[13]
%clear tmp;
%tmp=pn(2,:)
%pn(2,:)=-tmp
        rfn=RFGenerator(n,a,cond,mu,f);
        HRrtemp(n,:)=rfn*a^(2*n+1)*n*(n+1)*pn(1,:)./(r.*rnot).^(n+2);
```

[13] This and the next three lines were used to produce Figure 7-3.

```
        HRttemp(n,:)=rfn*a^(2*n+1)*n*(+1)*pn(2,:)./(r.*rnot).^(n+2);
        HT1rtemp(n,:)=rfn*a^(2*n+1)*n*(+1)*pn(2,:)./(r.*rnot).^(n+2);
        HT1ttemp(n,:)=(rfn*a^(2*n+1)./(r.*rnot).^(n+2)).*...
                        (n^2.*pn(1,:)-(n/(n+1)).*cot(theta).*(+1).*pn(2,:));
        HT2ptemp(n,:)=(rfn*a^(2*n+1)./(r.*rnot).^(n+2)).*...
                        (n.*csc(theta).*pn(2,:)/(n+1));
end

% r,theta, and psi components of the secondary fields

Rr=sum(HRrtemp).*RCoeff;
Rt=sum(HRttemp).*RCoeff;
Rp=0;

T1r=sum(HT1rtemp).*TtCoeff;
T1t=sum(HT1ttemp).*(-1).*TtCoeff;
T1p=0;

T2r=0;
T2t=0;
T2p=sum(HT2ptemp).*TpCoeff;
```

Legendre (MATLAB's Code)

```
function plm = legendre(l,amu,tflag)
%LEGENDRE Associated Legendre function.
%  P = LEGENDRE(N,X) computes the associated Legendre functions
%  of degree N and order m = 0, 1, ..., N, evaluated for each element
%  of X.  N must be a scalar integer less than 256 and X must contain
%  real values between -1 <= X <= 1.
%
%  If X is a vector, P is an (N+1)-by-L matrix, where L = length(X).
%  The P(m+1,i) entry corresponds to the associated Legendre function
%  of degree N and order m evaluated at X(i).
%
%  In general, the returned array has one more dimension than X.
%  Each element P(m+1,i,j,k,...) contains the associated Legendre
%  function of degree N and order m evaluated at X(i,j,k,...).
%
%  The associated Legendre functions are defined as:
%
```

```
%     P(n,m;x) = (-1)^m * (1-x^2)^(m/2) * (d/dx)^m { P(n,x) },
%
%  where P(n,x) is the Legendre polynomial of degree n. Note that
%  the first row of P is the Legendre polynomial evaluated at X
%  (the M == 0 case).
%
%  SP = LEGENDRE(N,X,'sch') computes the Schmidt semi-normalized
%  associated Legendre functions SP(n,m;x). These functions are
%  related to the (un-normalized) associated Legendre functions
%  P(n,m;x) by:
%
%        SP(n,m;x) = sqrt( 2*(n-m)!/(n+m)! ) * P(n,m;x)
%
%  Examples:
%   1. legendre(2, 0.0:0.1:0.2) returns the matrix:
%
%          |   x = 0        x = 0.1       x = 0.2
%      ------|-----------------------------------------
%      m = 0 |  -0.5000       -0.4850       -0.4400
%      m = 1 |         0       0.2985        0.5879
%      m = 2 |   3.0000        2.9700        2.8800
%
%   2. X = rand(2,4,5); N = 2;
%      P = legendre(N,X);
%
%   so that size(P) is 3x2x4x5 and
%   P(:,1,2,3) is the same as legendre(N,X(1,2,3)).

%  Acknowledgement:
%
%  This program is based on a Fortran program by Robert L. Parker,
%  Scripps Institution of Oceanography, Institute for Geophysics and
%  Planetary Physics, UCSD. February 1993.
%
%  MATLAB version: D. L. Chen, 5/24/93, 1/20/95.
%  Copyright (c) 1984-98 by The MathWorks, Inc.
%  $Revision: 5.13 $  $Date: 1997/11/21 23:45:43 $
%
%  Reference:
%   [1] M. Abramowitz and I.A. Stegun, "Handbook of Mathematical
%       Functions", Dover Publications, 1965, Ch. 8.
%   [2] J. A. Jacobs, "Geomagnetism", Academic Press, 1987, Ch.4.
```

```
%
%  Note on Algorithm:
%
%  LEGENDRE uses a three-term backward recursion relationship in M.
%  This recursion is on a version of the Schmidt semi-normalized
%  Associated Legendre functions SPc(n,m;x), which are complex
%  spherical harmonics. These functions are related to the standard
%  Abramowitz & Stegun functions P(n,m;x) by
%
%     P(n,m;x) = ((-1)^m)*sqrt((n+m)!/(n-m)! ) * SPc(n,m;x)
%
%  They are related to the Schmidt form given previously by:
%
%     SP(n,m;x) =  SPc(n,0;x);
%           = ((-1)^m)*sqrt(2) * SPc(n,m;x), m > 0

if nargin < 3
   tflag = 'unnorm';
end;

% Check degree constraints
lmx = 256;   % initialize lmx
if (prod(size(l)) > 1) | (l >= lmx),
   error(sprintf('N must be a positive scalar < %d.',lmx));
elseif l <= 0
   plm = ones(size(amu));
   return
end

% Convert amu to a row vector
siz = size(amu);
amu = amu(:)';

% Initialize parameters
nmx=2*lmx;
% The following three are parameters from Parker's Fortran code
tol = 0.10000000168623835 3e-15;
alogt = -0.368413619995117188e+02;
tstart = 0.999999993922529029e-08;

rootn=sqrt(0:nmx);
s=sqrt(1.0 - amu.^2);
```

```
plm = zeros(l+1,length(amu));
tlm = zeros(l+3,length(amu));

% Calculate TWOCOT, separating out the amu = -1,+1 cases first
twocot = amu;      % initialize dimensions of TWOCOT

kk = find(amu == -1);
if ~isempty(kk)
   twocot(kk) = Inf;
end;

kk = find(amu == 1);
if ~isempty(kk)
   twocot(kk) = -Inf;
end;

kk = find(s~=0);
if ~isempty(kk)
   twocot(kk)  = -2.0*amu(kk)./s(kk);
end;

% Small sine: prevent underflow By starting at m=m1-1<l

% First, replace s_copy = 0 with s_copy = NaN to avoid log(0) error messages.
% This is okay since we want nonzero s anyway.
scopy = s;
kk = find(s == 0);
scopy(kk) = NaN;
ind = find(l*log(scopy) < alogt);

if ~isempty(ind)
% Approx solution of x*ln(x)=y
   v = 9.2-alogt./(l*s(ind));
   w = 1./log(v);
   m1=1+l*s(ind).*v.*w.*(1.0058+ w.*(3.819 - w*12.173));
   m1=min(l+1, floor(m1));

% column-by-column recursion
  for k = 1: length(m1)
      mm1 = m1(k);
      col = ind(k);
      tlm(mm1:l+1,col)= zeros(size(mm1:l+1))';
```

```
      % Start recursion with proper sign
      tlm(mm1,col)  = sign(rem(mm1,2)-0.5)*tstart;
      if amu(col) < 0, tlm(mm1,col)=sign(rem(l+1,2)-0.5)*tstart; end;

      % Recur from m1 to m=0, carrying normalizing
      sumsq=tol;
      for m= mm1-2:-1:0,
         tlm(m+1,col)=((m+1)*twocot(col)*tlm(m+2,col)- ...
         rootn(l+m+3)*rootn(l-m)* tlm(m+3,col))/ ...
         (rootn(l+m+2)*rootn(l-m+1));
         sumsq=tlm(m+1,col)^2 + sumsq;
      end;
      scale=1.0/sqrt(2*sumsq - tlm(1,col)^2);
      tlm(1:mm1+1,col)=scale*tlm(1:mm1+1,col);
   end    % FOR loop

end % small sine IF loop

% Zero out the columns that have been calculated above, saving S
tmps = s(ind);
s(ind) = zeros(size(ind));
nind = find(s);

% Regular recursion from m=l to 0
if ~isempty(nind)

   % Produce normalization constant
   c=1.0;
   twol=2.0*l;
   for x= 2.0: 2: twol
      c=c - c/x;
   end;

   tlm(l+1,nind)= sqrt(c)*(-s(nind)).^l;
   tlm(l,nind)  = tlm(l+1,nind).*twocot(nind).*l./sqrt(twol);

   % Recur downwards to m=0
   for m= l-2: -1: 0,
      tlm(m+1,nind)=((m+1)*twocot(nind).*tlm(m+2,nind) ...
         - rootn(l+m+3)*rootn(l-m).* ...
         tlm(m+3,nind))/(rootn(l+m+2)*rootn(l-m+1));
```

```
   end;

end % IF loop

% Calculate the Schmidt semi-normalized functions
s(ind) = tmps;  % restore s
plm(1:l,:)=tlm(1:l,:);
plm(l+1,:)=tlm(l+1,:);

% Polar argument   (mu=+-1)
s0 = find(s == 0);
if ~isempty(s0)
   plm(1,s0)=amu(s0).^l;
end

if strcmp(tflag,'sch')
   % Calculate the standard Schmidt semi-normalized functions from these
   % functions. For m = 1,...,l, multiply by (-1)^m*sqrt(2)
   row1 = plm(1,:);
   plm = sqrt(2)*plm;
   plm(1,:) = row1;    % restore first row
   const1 = 1;
   for r = 2: l+1;
      const1 = -const1;
      plm(r,:) = const1*plm(r,:);
   end;

else
   % Calculate the standard A&S functions (i.e., unnormlized case) from
   % these functions by multiplying each row by: ((-1)^m)*sqrt((l+m)!/(l-m)!)
   const1 = 1;
   for r = 2: l+1
      m = r-1;

      % Find const for row r
      const = exp(0.5 * (sum(log(2:l+m)) - sum(log(2:l-m)) ) );

      plm(r,:) = const*plm(r,:);
   end;

end;
```

```
% Pack into output array
if length(siz) == 2 & min(siz) == 1
   plm = reshape(plm,l+1,max(siz)); % Row or column vector case
else
   plm = reshape(plm,[l+1 siz]);
end
```

RFGenerator

```
%function [rf] = RFGenerator(n,a,cond,mu,f)
%
% This function computes the response function for the nth order multipole in a
% sphere of radius 'a' m, conductivity 'cond' (ohm*m)^-1, magnetic permeability
% 'mu' H/m, and survey frequency 'f' Hz.
%
% The Bessel functions and their derivatives are calculated with RFBessel which
% uses a series solution approach.  This method provides accurate response
% function values up to a response parameter of 1000.
%
% Written By Tricia Nichols
% 12 March 1997
%

function [rf] = RFGenerator(n,a,cond,mu,f)

munot=4*pi*10^(-7);          %magnetic permeability of free-space
omega=2*pi*f;                %vector of angular frequencies
ka=sqrt(i*cond*mu*omega)*a;
rp=abs(ka.^2);               %response parameter vector

[bess, bessprim]=RFBessel(n+.5,ka);

rf=((munot/2-
(n+1)*mu)*bess+munot*ka.*bessprim)./((munot/2+n*mu)*bess+munot*ka.*bessprim);
```

RFBessel

```
% function [bess,bessprim] = RFBessel(n,x)
```

```
%
% RFBessel calculates the n'th order bessel function of a vector
% of numbers x, and stores the results in a vector, bess. The
% first derivative is also calculated and stored in a vector, besprim.
%
%Note:          - n must be a positive integer.
%       - the series solution is calculated with 30 of terms.
%
% Written By Tricia Nichols
% February 1997
%
function [bess,bessprim] = RFBessel(n,x)

for k=0:30-1
        temp1(k+1,:)=((x/2).^(n+2*k))/(gamma(k+1)*gamma(k+1+n));
        temp2(k+1,:)=((n+2*k)*(x/2).^(n+2*k-1))/(2*gamma(k+1)*gamma(k+1+n));
end

for k=1:length(x)
        bess(k)=sum(temp1(:,k));
        bessprim(k)=sum(temp2(:,k));
end
```

VCProfile

```
% VCProfile.m
%
%This program plots the vertical coplanar profiles from the calculated
%fields of VerticalCoaxial.m
%Note the fields have been plotted such that they are POSITIVE values!
%Only the component of the field that is perpendicular to the vertical coil
%receiver will contribute to the field measured there.

figure
plot(d./S,-HR);
hold
plot(d./S, -HI,':');
legend('Real','Imaginary')
title 'Normalized Vertical Coaxial Profile of a Conductive Sphere'
grid; ylabel 'Percent'
xlabel 'Distance in Coil Separations'
```